NOAA/NSSL's WSR-88D Radar for Research and Enhancement of Operations:

Polarimetric Upgrades to Improve Rainfall Measurements

National Severe Storms Laboratory Report

prepared by: R. J. Doviak and D. S. Zrnić
with contributions from: J. Carter, A. Ryzhkov, S. Torres, and A. Zahrai

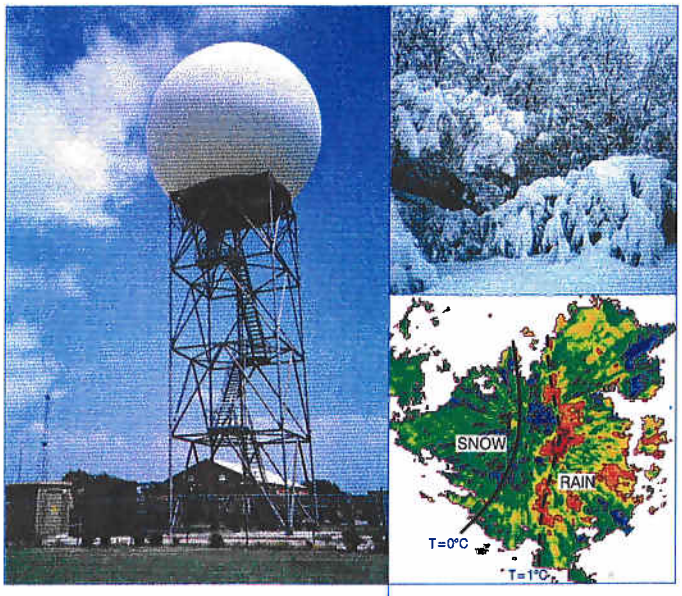

April 1998

National Oceanic and Atmospheric Administration
National Severe Storms Laboratory
Norman, Oklahoma 73069

NOAA/NSSL'S WSR-88D RADAR for
RESEARCH and ENHANCEMENT OF OPERATIONS:

POLARIMETRIC UPGRADES TO IMPROVE RAINFALL MEASUREMENTS

A National Severe Storms Laboratory Report

Prepared by : R. J. Doviak and D. S. Zrnic
with contributions from: J. Carter, A. Ryzhkov, S. Torres, and A. Zahrai

April 1998

NOAA NATIONAL SEVERE STORMS LABORATORY
1313 HALLEY CIRCLE
NORMAN, OKLAHOMA 73069

PREFACE

The National Severe Storms Laboratory (NSSL) is the leading NOAA agency for advancing weather radar research, engineering, and applications. Prominent among the high impact projects and experiments conducted at the NSSL was the Joint Doppler Operational Project (JDOP) which gave impetus to the design and establishment of the NEXRAD (now the WSR-88D). To a large part, the WSR-88D is based on the experience with the research Doppler radars developed by NSSL staff. The media for informing the National Oceanic and Atmospheric Administration (NOAA) and the National Weather Service (NWS) management and staff about hardware advances in radar techniques are NSSL reports specifically tailored to the weather agencies' needs. Following extensive research in the mid eighties, two reports dealing with dual polarization capabilities for the NEXRAD were generated for the NWS. (These report titles are listed on the last page of this report.) Since then, more research has been done, and new experiences have emerged. In this spirit, the present report is a successor to those previous reports. It is meant to document the details that lead us to favor a novel scheme for obtaining polarimetric variables in order to improve the quantitative estimation of precipitation. Furthermore, it describes hardware changes in the microwave and antenna assemblies, as well as measurements of the antenna patterns before and after the modifications to the research WSR-88D (designated KOUN1). The report is written for engineers and managers, and the information it contains is detailed enough to gauge the basis upon which recommendations are made for upgrades to the network of WSR-88Ds. This report describes the effects that changes in antenna hardware for polarimetric upgrades have on the radiation patterns, and provides information necessary for making decisions on the selection of a polarization basis. Possible configurations of hardware are also suggested. Ultimately, it is the cost effectiveness (not addressed in this report) that should prevail in the decision process.

EXECUTIVE SUMMARY

This report focuses on the steps undertaken by the National Severe Storms Laboratory (NSSL) to improve rainfall measurements by adding a polarimetric capability to the research WSR-88D (designated as KOUN1). One of the most important elements in obtaining a good polarimetric radar is a good antenna with low sidelobes and matched radiation patterns (i.e., the distribution of radiated power density vs. angular displacement from the beam axis) for horizontally and vertically polarized waves. The polarimetric characteristics and radiation patterns of the KOUN1 radar are presented in Section II. An engineering evaluation was made to determine if the existing antenna assembly with minimum modification could be used for the dual polarization mode. This is indeed the case; therefore, obvious savings in hardware and manpower would ensue by adopting the proposed design.

Because no pattern measurements were ever made of any WSR-88D antennas on site, it was imperative to make measurements on the KOUN1 antenna before the feed was changed from one which transmits only horizontally polarized waves to one (a dual port feed) which transmits both horizontally and vertically polarized waves. The patterns, before change of feed, demonstrate that there are no significant changes in the quality of the antenna installed in 1988.

A dual port antenna feed was purchased from Andrew Canada, Inc. (manufacturers of the WSR-88D antennas) and installed on the radar. Pattern measurements were made for the horizontal and vertical polarizations. It is comforting to note that the radiation patterns with the dual port feed are very close to those patterns measured with the single port feed. For polarimetric measurements, it is desirable to have a good match of main lobes at horizontal (H) and vertical (V) polarizations. Both copolar patterns have low sidelobe levels and are well matched in the mainlobe. Beamwidths are 0.93° for the horizontal copolar and 0.90° for the vertical copolar patterns. The match of patterns in the lower half of the vertical plane is excellent; it even extends to several of the sidelobes. For the most part, the patterns agree within ±1 dB, and the match is best where the gain is largest (i.e., near the beam axis). For the points far removed from the axis, the differences are larger as expected, but because the antenna gain is much smaller in these regions, the differences are much less significant than for those close to the axis.

Cross polarization patterns were also recorded, and it was observed that the WSR-88D specification of < -30 dB is met. The cross-polar pattern at vertical polarization matches in shape the cross-polar pattern at horizontal polarization, but the amplitudes are about 4 dB higher (still within the measurement uncertainty). Consequently, the addition of the dual port feed and the retention of the three struts had not degraded the patterns. Therefore, this configuration is recommended for future polarimetric upgrades of the WSR-88D.

Of critical importance to the favorable utility of a polarimetric radar is the selection of an appropriate polarization basis and its practical implementation. Considerations for the choice of polarimetric basis and a few system design options are described in Section III. The circular and

linear polarimetric bases are compared. It is demonstrated that the circular basis can, in principle, provide estimates of specific differential phase (K_{DP}) without switching the transmitted polarization. In weak showers, these estimates are corrupted because the cross-polar signal is almost three orders of magnitude below the copolar signal. But with circular polarization, the cross-polar signal does not depend on the orientation of hydrometeors; furthermore, in combination with the copolar signal, it leads to the measurement of the mean canting angle. Nonetheless, this apparent advantage of the circular polarization basis vanishes in the presence of significant precipitation along the radar beam. A linear polarization basis is well suited for quantitative measurement of rainfall and classification of hydrometeor types without extensive correction of propagation effects. Therefore, our choice rests with the linear H, V basis.

A novel polarimetric scheme employing simultaneous transmission of horizontally and vertically polarized waves is being implemented on the KOUN1 radar. Principally, the motivation for simultaneous transmission is to do away with an expensive high power microwave switch which has been the key component in research polarimetric radars during the 1980s and 1990s. This design includes installation of two receivers that share several common components, but a single receiver can also measure all the polarimetric variables. With two receivers, the dwell time for computing polarimetric variables is reduced, the ground clutter filter is not affected, and maintenance is simpler. On the down side, the depolarization ratio cannot be measured simultaneously with other polarimetric variables, but if desired, it can be measured together with the standard spectral moments in separate volume scans. Having two receivers offers some redundancy that might be advantageous. For comparative testing, NSSL plans to incorporate two receivers in its radar and still provide full WSR-88D compatibility. That is, all current data acquisition modes and scanning strategies can remain as they are, and the impact of polarimetric implementation on the existing algorithms and products should be minimal.

Theoretical evaluation of the effects that feed alignment, drop canting, and backscatter depolarization have on the measurements of polarimetric parameters is made in Section IV for simultaneous transmission and reception of H and V signals. The simultaneous transmission and reception mode is not detrimental to measurements of the specific differential phase and coefficient of correlation between H, V weather echoes. The effects, however, on differential reflectivity of drop canting along propagation paths can be significant. But these effects are harmful only when differential attenuation dominates, which is a problem whether H, V signals are transmitted simultaneously or alternately. Differential reflectivity and the correlation coefficient could be affected by depolarization due to backscattering from hail mixed with rain. On the other hand, backscatter depolarization would accentuate the hail signature of low Z_{DR} and low ρ_{hv} (i.e., reduce even more the low values of Z_{DR} and ρ_{hv} in hail regions). Thus, the effect might be beneficial.

In summary, the report has demonstrated the following. After the change of feed and one strut on the antenna assembly, the radiation pattern satisfies original WSR-88D specifications. The patterns for horizontal and vertical polarizations are well matched, and the cross-polar pattern is sufficiently suppressed. A linear horizontal and vertical polarization basis is preferred

to a circular basis. The proposed simultaneous transmission and reception of H, V waves is completely compatible with the existing signal processing algorithms on the operational WSR-88Ds. Theoretical analyses of the factors that might affect the precision in measurement of intrinsic polarimetric variables suggests that the simultaneous transmission of H, V waves is a sound method and should be tested.

ACKNOWLEDGEMENTS

We are grateful to the management and staff of the National Severe Storms Laboratory (NSSL), who provided continued support and encourgement to the Doppler radar project during the formative stages in the development of the National Oceanic and Atmospheric Administration (NOAA)/NSSL's research WSR-88D (i.e., the KOUN1). We thank the National Weather Service (NWS) for providing radar parts that made it possible for the NWS Operational Support Facility (OSF) and NSSL to assemble an updated WSR-88D (i.e., the KCRI) on the campus of the University of Oklahoma's (OU) Research Park. This allowed for the transfer of the prototype WSR-88D (i.e., the KOUN1) to NSSL and provided the OSF with a WSR-88D identical to the operational WSR-88Ds they are responsible to maintain and upgrade. OU's Cooperative Institute for Mesoscale Meteorological Studies (CIMMS) management and staff are thanked for providing personnel to this project. Part of the work described herein was supported by Dr. James Rasmussen, Director of the NOAA's Environmental Research Laboratory, with contributions from his Director's Discretionary Fund.

The staff of the NWS Operational Support Facility (OSF) in Norman, Oklahoma, gave us much needed technical guidance concerning the operation of the KOUN1 and provided critical documentation and materials necessary to implement a polarimetric upgrade which this report addresses. Richard Wahkinney and Mike Schmidt of the NSSL provided crucial technical assistance in the design, fabrication, and installation of the components necessary for the polarimetric upgrades. Dale Sirmans of the Titan Corp. was a source of technical expertise concerning WSR-88D details. Dr. John Fagan of the Electrical Engineering Department of OU supplied the GPS system to determine the locations of test equipment used for antenna pattern measurements on the KOUN1. The Physics Department of OU provided a much needed precision rotator to measure the alignment of the polarization ellipse. Dr. Bringi and Mr. Brunkow of Colorado State University provided the data for Figs. IV.12 and IV.13 from the first experimental comparisons of polarimetric data based on simultaneous and alternate transmissions of H,V polarized waves. Joan O'Bannon drafted several figures and composed the cover.

NOAA/NSSL'S WSR-88D RADAR for
RESEARCH and ENHANCEMENT OF OPERATIONS:

POLARIMETRIC UPGRADES TO IMPROVE RAINFALL MEASUREMENTS

TABLE OF CONTENTS

NOAA/NSSL'S WSR-88D RADAR for
RESEARCH and ENHANCEMENT OF OPERATIONS:

POLARIMETRIC UPGRADES TO IMPROVE RAINFALL MEASUREMENTS

I. INTRODUCTION

The WSR-88D (NEXRAD) radar system is a national network of weather surveillance Doppler radars serving the National Weather Service (NWS), the Air Weather Service (AWS), and the Federal Aviation Administration (FAA). Operational experience with these meteorological radars has encouraged users' demand for additional capabilities and improvements. Thus, many parallel efforts are underway to resolve deficiencies and implement new features and enhancements. One deficiency is the constraint on developing improved algorithms for product generation (e.g., rainfall accumulation, range-velocity ambiguity mitigation, etc.) caused by specialized computer hardware designed during the late 1970s and early 1980s. Likewise, the Radar Data Acquisition (RDA) unit of the WSR-88D is based on a custom signal processor and other subsystem components whose proprietary nature makes systematic replacement and incremental upgrades extremely difficult. Thus, the NSSL has been tasked to develop a Radar Product Generator (RPG) and an RDA unit using an open system design which incorporates off-the-shelf components meeting rigid standards.

One of the enhancements to the WSR-88D, to be made possible by upgrading the RDA to an open system design, is the addition of a polarimetric capability to improve rainfall estimation and to make possible the identification of precipitation types (e.g., distinguishing rain from hail, snow, etc.). Relations between radar reflectivity factor Z and rainfall rate R have been used for several decades to estimate rainfall accumulation, forecast flash flood conditions, etc. Although high reflectivity factor values correlate with high rainfall rates, there is no unique relation between the two. To improve the accuracy of the rainfall estimated with radar, considerable effort has been expended by meteorologists over the past decades to develop techniques to tune the R,Z relations to specific types of rain (e.g., stratiform, convective, etc.). Also, the WSR-88D radar, which presently measures Z for horizontally polarized waves, has not changed the basic way in which rainfall is measured. Improvements in rainfall estimation brought about by the WSR-88D are due to improvements in radar calibration, narrow beamwidth and lower sidelobes, real-time access to rain gauges to tune the R,Z relations,etc. Fundamentally, there has not been any significant change in the way rainfall is estimated by the WSR-88D.

This state of affairs has been dramatically altered by research initiated in the late 1960s at the National Research Council, Ottawa, Canada, (Barge 1970; 1974), and at the Ohio State University in the early 1970s (Seliga and Bringi 1976) which showed that the added information

provided by a polarimetric radar has the potential to detect hail and improve the accuracy of estimating rainfall. The focus of the later research was to use polarimetric information (i.e., differential reflectivity factor Z_{DR} measured using both horizontally and vertically polarized waves, in addition to *Z)* to estimate the parameters of an assumed two parameter drop size distribution. Rainfall rate based upon *Z* measured with a single linearly polarized wave constrains the assumed drop size distribution to a single parameter; in general, the drop size distribution can only be accurately described by a distribution function having many parameters. Remote measurements with polarimetric radars are based on the assumption that the eccentricity of drops increases predictably with their size (Beard et al. 1989). The Z_{DR}, *Z* approach to improve rainfall estimate assumes that rain rates measured with singly polarized waves (e.g., like that transmitted by the WSR-88D) have errors principally caused by highly variable drop size distributions; these cannot be measured with a single, linearly polarized wave. On the other hand, Zawadski (1984) pointed out that variability of drop-size distributions is only one of many factors that affect the accuracy with which radar measures rain, and it is not necessarily the most important factor.

Sachidanada and Zrnic (1986) showed that the relation between specific differential phase (i.e., the differential propagation phase shift per unit length between vertically and horizontally polarized waves) and rainrate is relatively insensitive to drop size distribution and, thus, can also form the basis of rain measurement using a single parameter relation (i.e., an R,K_{DP} relation). Equally important, Zrnic and Ryzhkov (1996) have shown that the specific differential phase method of measuring moderate to heavy rain rates overcomes many of the factors that limit rain measurement accuracy (e.g., calibration errors, wet radome, ground clutter backscattered routinely or through anomalous propagation conditions, underestimation of extreme rainfalls, attenuation, ground clutter canceller bias, etc.). Thus, the addition of a polarimetric capability to the WSR-88D will provide, for the first time, a revolutionary approach to the radar measurement of rainfall. This improvement could significantly increase the accuracy of rainfall measurements, lead to issuance of more timely and accurate flash flood warnings, and provide other improved hydrological products of importance to agricultural and commercial enterprises.

Recent experiments with dual-polarized Doppler weather radars have demonstrated great potential in solving a variety of problems in operational meteorology. The following is a list of what dual polarization can do:

- Improve quantitative precipitation estimation
- Discriminate hail from rain, possibly gauge hail size
- Identify precipitation type in winter storms
- Measure precipitation in the presence of ground clutter
- Identify electrically active storms
- Identify the presence of insects, birds, and chaff
- Improve the accuracy of VAD winds
- Provide initial conditions and constraints to numerical models
- Identify aircraft icing conditions

This report focuses on the steps undertaken by the National Severe Storms Laboratory (NSSL) to improve rainfall measurements by adding a polarimetric capability to the research WSR-88D (designated as KOUN1). One of the most important elements in obtaining a good polarimetric radar is a good antenna with low sidelobes and matched radiation patterns (i.e., the distribution of radiated power density vs. angular displacement from the beam axis) for horizontally and vertically polarized waves. The polarimetric characteristics and radiation patterns of the KOUN1radar are presented in Section II. Section III contains a critical comparison of two polarimetric bases (linear and circular) to decide which basis to implement. Section III also reviews the options of simultaneously transmitting horizontally (H) and vertically (V) polarized waves or implementing the well-tested option of alternately transmitting H and V waves. Principally, the motivation for simultaneous transmission is to do away with an expensive high power microwave switch which has been the key component in research polarimetric radars during the 1980s and 1990s. Furthermore, simultaneous transmission and reception is completely compatabile with the existing signal processing algorithms and procedures that have been implemented and tested on the national network of operational WSR-88D radars over several years. Section IV provides a theoretical analysis of the factors that might affect the precision in measurement of intrinsic polarimetric variables if simultaneous transmission of H, V waves is used.

II. PATTERN MEASUREMENTS OF THE RADIATION FIELDS FROM NSSL'S RESEARCH WSR-88D RADAR

One of the modifications being made to NSSL's WSR-88D radar is conversion from one that transmits and receives only a horizontally polarized electric field to one in which both vertically and horizontally polarized fields are transmitted and received, simultaneously, in two receiving channels. This will allow polarimetric variables (e.g., the differential phase and the correlation between horizontally and vertically polarized echoes) to be measured directly. Polarimetric variables are important to the potential improvement of rainfall rate measurements with the WSR-88D radar network.

The WSR-88D antenna has a reflector with a diameter of 8.53 m (28 feet) illuminated by a primary radiator supported by three spars (Fig. II.1a). The focal length to diameter ratio f/D of the reflector is 0.375. The frequency assigned to operate this radar is 2705 MHz, corresponding to a wavelength of 0.111 m.

II.1. Radiation pattern measurements of NSSL's research WSR-88D (the KOUN1 radar) before the change to a dual port feed.

No pattern measurements were made on the KOUN1 radar installed near the NSSL in 1989, nor, for that matter, were antenna measurements made after any of the WSR-88D antennas were installed at their respective sites (with or without radomes). Therefore, it was imperative to make measurements on the existing antenna before the primary radiator was changed from one which transmitted and detected radiation having only horizontal polarization (i.e., the electric field is horizontal) to one that transmits and detects fields having both horizontal and vertical polarizations. These measurements would serve as a baseline to compare radiation patterns obtained with the new primary radiator or feed which illuminates the paraboloidal reflector of the KOUN1 radar, as well as to determine if there were any significant changes from the radiation patterns measured at the manufacturer's (Andrew Canada, Inc.) antenna range.

II.1.1 Pattern measurements made at the manufacturer's antenna range

Radiation pattern measurements were made on several WSR-88D antennas, usually without radomes, using the antenna range of Andrew Canada. At this facility, the WSR-88D antenna is rotated azimuthally about a vertical axis, while the axis of the paraboloidal reflector remains in a horizontal plane. Although all pattern measurements are made by rotating the antenna about a vertical axis while the beam is pointed at the horizon, the paraboloidal reflector can be rotated about its axis so that pattern measurements can be made along various planes (or "cuts") through the beam (i.e., the main lobe) center.

For example, the 0° cut gives a pattern measurement as a function of the azimuthal angle for the antenna in its normal configuration (i.e., as in Fig. II.1a); for the 90° cut, the reflector is

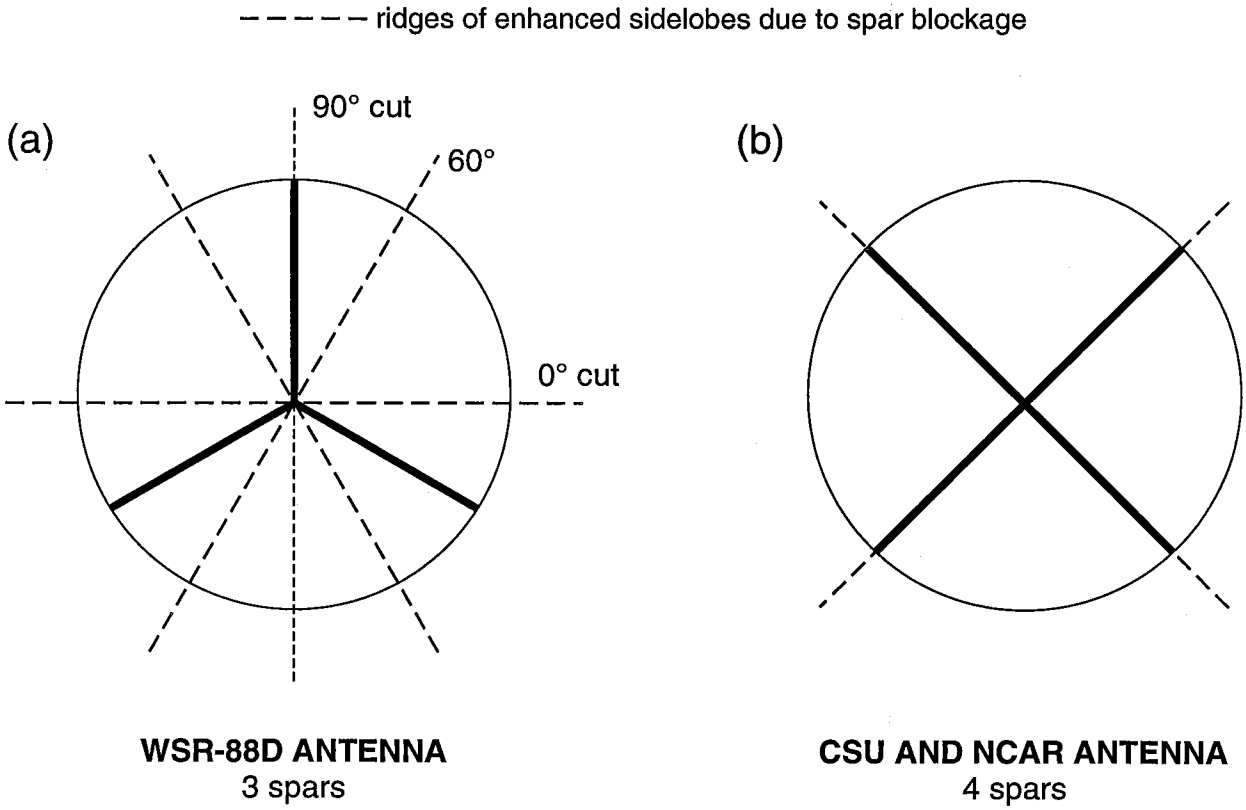

Fig. II.1 (a) Feed support configuration on the WSR-88D antenna. (b) the four-spar configuration used on antennas at the Colorado State University (CSU), and at the National Center for Atmospheric Research (NCAR).

rotated 90° about its axis, and the antenna is again rotated about the vertical to simulate a pattern measurement in the vertical plane. A sample of the one-way radiation patterns, measured on Andrew Canada's range for linear horizontally polarized waves at a frequency of 2700 MHz, is given in Figs.II.2a, b (reproduced from the Paramax Systems Corp. report, 1992). *These patterns were measured without a radome* and are the copolar patterns in the plane of the electric field (i.e., in the E-plane which is the 0° cut for a horizontally polarized fields).

To highlight the levels of the far-out sidelobes, Fig. II.2a shows the full 360° pattern for radiation below the -40 dB level, whereas Fig. II.2b shows the pattern of sidelobes nearby the main lobe and the radiation pattern of the main lobe itself (the left side on a ±20° scale, and the right side on a ±2° scale; adapted from the Paramax System Corp. report, 1992). The heavy solid lines in Fig. II.2 are the maximum sidelobe levels allowed by the NEXRAD specification number DV1208252G when the antenna is in its radome. Measurements of antenna patterns with and without a partially assembled radome, made by Andrew Canada over a ±20° interval (not presented here) indicate that the radome has negligible effect on the main lobe but alters the sidelobe levels; mostly increasing them. Nevertheless, the increase in sidelobe levels near the

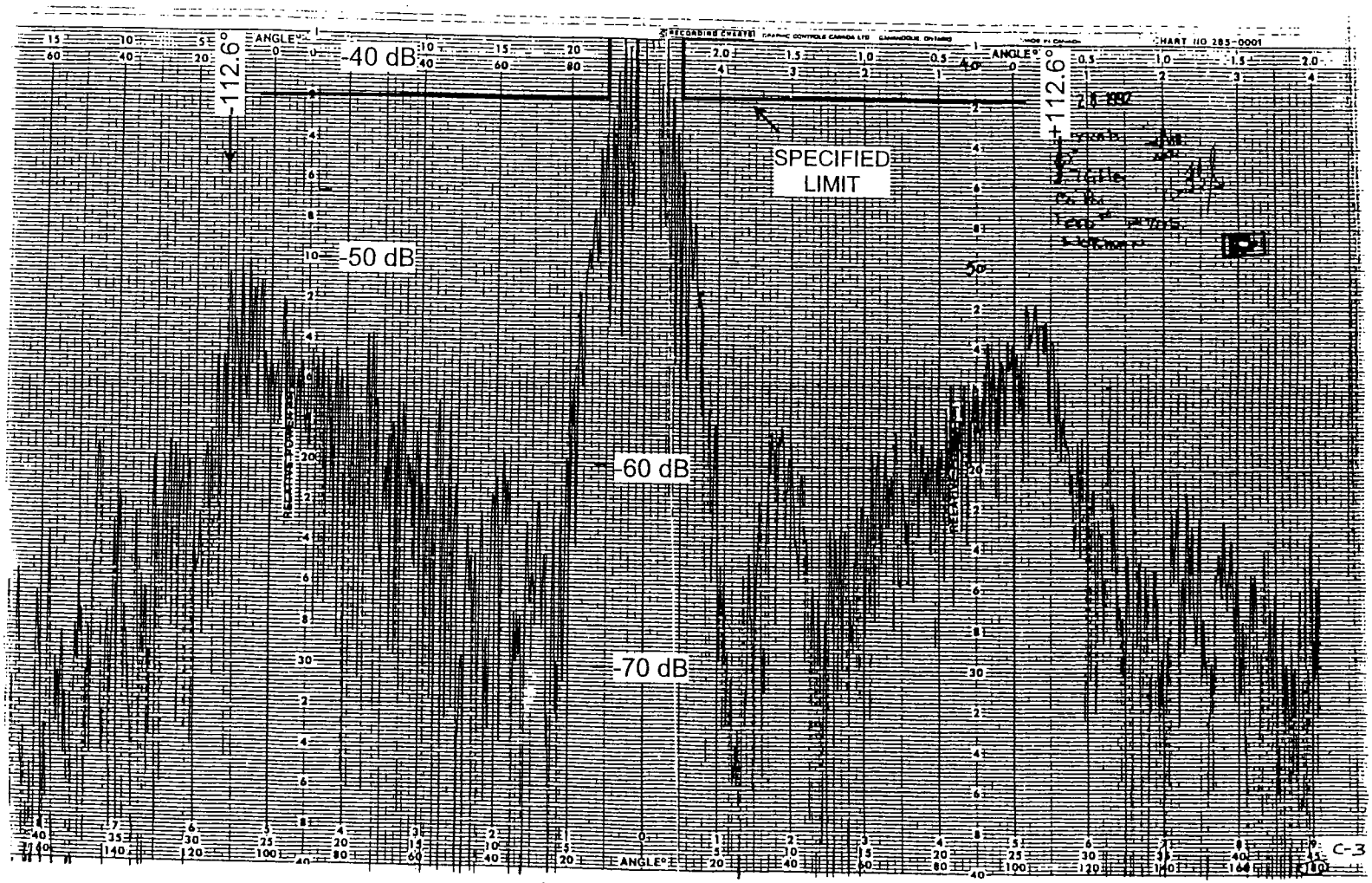

Fig. II.2 The copolar radiation (HH) pattern (0° cut) for horizontally polarized fields radiated by the WSR-88D reflector, without radome, on the antenna range of Andrew Canada Inc. The dB scale is relative to the peak of the main lobe. (a) the radiation pattern over ±180°; only the pattern portion below -40 dB is shown.

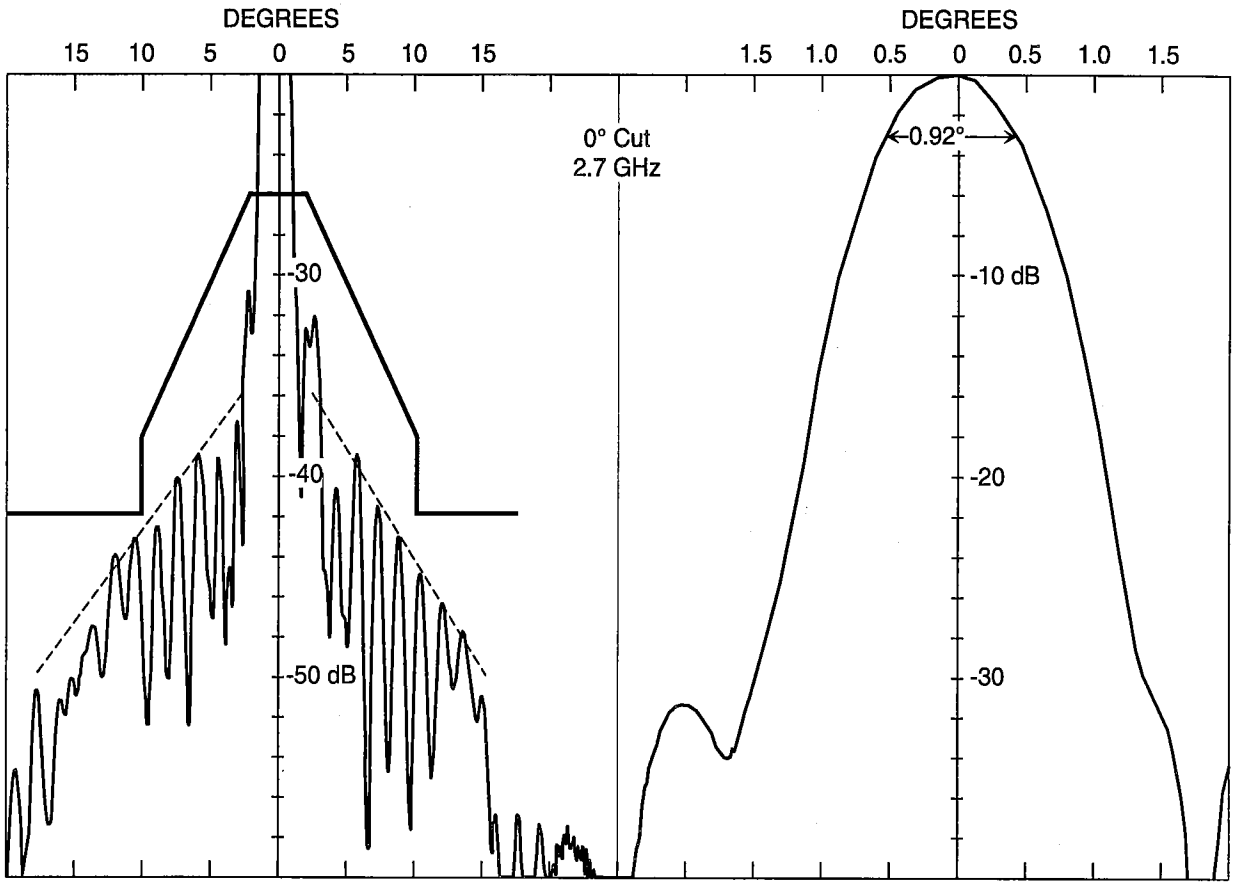

Fig. II.2 (b) left side: the near side lobes shown over an azimuthal interval of about ±20° about the main lobe; heavy solid lines are the specified maximum sidelobe levels with radome. Dashed lines are the approximate envelope of the sidelobes between 3° and about 16°. The figure to the right is the main lobe or beam pattern over an azimuthal interval of about ±2°.

main lobe is no more than 2 dB. These increases did not cause the sidelobe levels to exceed the specified limits.

The sidelobes far removed from the main beam (Fig. II.2a) show a monotonic decrease to about the -65 to -75 dB levels at ±25°, followed by an upward trend to about the -50 dB level at ±110°, beyond which the sidelobes decrease in amplitude. This increase of sidelobe level, to a peak near 110°, is inferred to be radiation transmitted principally from the feed of the WSR-88D antenna. The sudden decrease in sidelobes beyond about 110° occurs because the primary radiation from the feed and scatter from the spars is obscured by the reflector; calculations show that focus of the reflector is obscured at an angle of 112.6°, which supports the inference.

The nearby sidelobes are likely those caused by the spars (i.e., waveguides are used as spars which support the feed) and the feed, which block the radiation (i.e., secondary radiation) reflected from the paraboloid, as well as distortions of the reflector's surface which alter the phase distribution across the aperture. The spars are attached to the edge of the reflector so that none of the primary radiation from the feed is blocked by the spars. Calculations (Section II.5) of the theoretical pattern suggest that sidelobes could be more than several dB lower than that seen in Fig. II.2b, if blockages and distortions in the reflector's surface were not present. The one-way 3-dB beam width along the 0° cut is 0.92°, whereas the beam width in the 90° cut (not shown here) is 0.93°. Thus, the main lobe appears to be nearly circularly symmetric; this will be shown to be the case in Section II.1.2.4 (Fig. II.4d).

II.1.2 Pattern measurements of the KOUN1

The radiation pattern measurements of the KOUN1 radar made at NSSL were not conducted on an ideal range. Nevertheless, the terrain surrounding the KOUN1 radar is flat, and the area between the KOUN1 radar and the radiation source (i.e., a standard-gain horn mounted atop the University of Oklahoma's Energy Center, a 13-story building) contains mostly one-story wooden houses and a relative abundance of trees which are considered not very reflective. No large reflecting surfaces are evident in the area near the line-of-sight to the standard-gain horn. There are, however, a few tall metallic structures (e.g., water towers) at points far removed from the line-of-sight (Fig. II.3). Although this practical antenna range is not ideal, it does provide a suitable base to make measurements of the mainlobe and stronger sidelobes. These measurements can be compared with those made on Andrew Canada's antenna range. In addition, these measurements provide a basis for comparison of radiation patterns made on the antenna after the feed is changed to transmit and receive waves having dual (H, V) polarizations.

II.1.2.1 *Measurements of vertical axis tilt*

The tilt of the nominally vertical axis, about which the KOUN1 antenna rotates in azimuth, was checked by extending a plumb line from the top of the reflector when the antenna was in its stowed position. (In this position, the elevation angle is slightly negative.) The distance between the plumb line and the bottom edge of the reflector was measured to be a sinusoidal function of azimuth with an average separation of 25 mm. Given the reflector diameter of 853 mm, the elevation angle of the reflector axis (this should also be the beam axis) in the stowed position is −0.17°. The sinusoidal amplitude was estimated to be 7 mm with a maximum displacement at an azimuth of about 270°. This implies that the axis of rotation is tilted to the west by 0.05°. Because this tilt is much less than a beamwidth (≈ 1°), we did not make any adjustments to correct for this error.

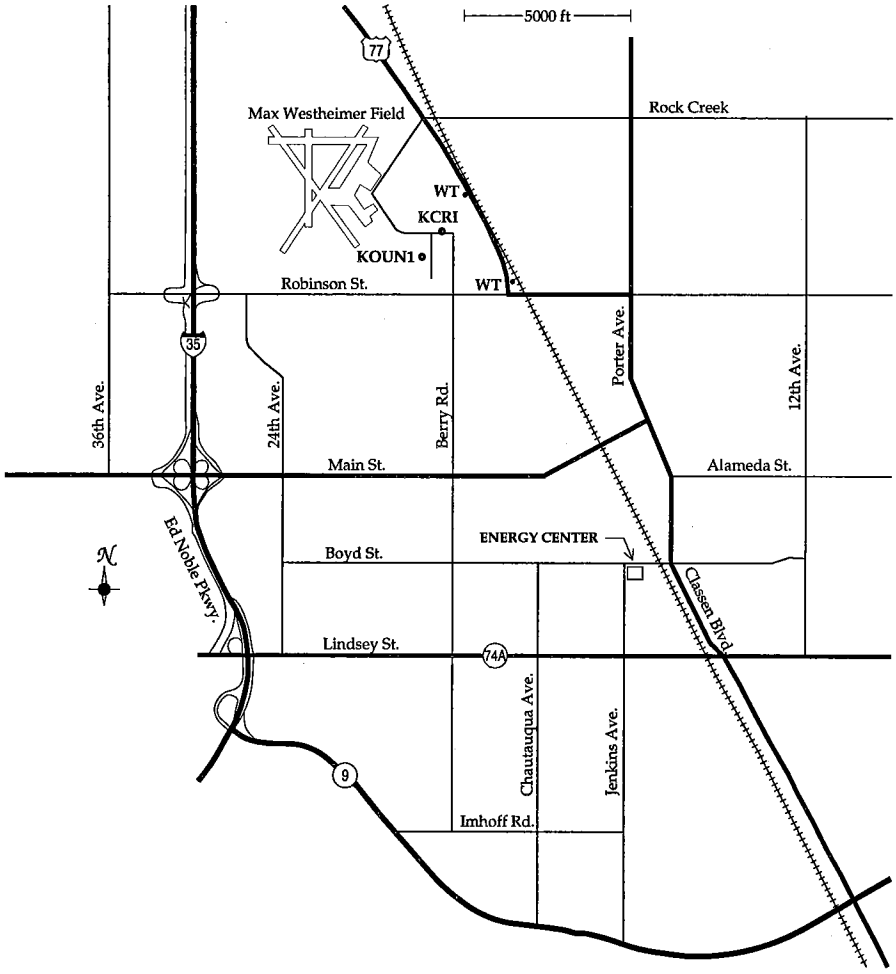

Fig. II.3 The U.S. Department of the Interior's Geological Survey map showing the locations of KOUN1, KCRI, the Energy Center, and water tower/tanks (WT) near the KOUN1 site.

II.1.2.2 *The KOUN1 antenna range*

The radiation source for the pattern measurements is 1263 feet[1] (385.0 m) above a reference ellipsoid of the earth. The KOUN1 reflector's center is 1,169 feet[2] (356.3 m) above the

---

[1]This datum was obtained from a differential Global Positioning Satellite (GPS) survey performed by Mr. Hazem Hejjb of the Electrical Engineering Department of the University of Oklahoma. The stated accuracy of the differential GPS survey is reported to be better than a few centimeters.

[2]This datum was also obtained from a differential GPS survey on top of the KOUN1 antenna platform, but the height given includes the ≈ 4.75 m distance from the platform to the center of the reflector at 0° elevation angle.

reference ellipsoid and is at a distance of 11,299 feet (3.444 km) from the source (Fig. II.3). This distance is calculated from the following GPS-derived latitude and longitude coordinates:

Standard-gain horn:	35° 12' 38.6" N; 97° 26' 25.5" W
KOUN1:	35° 14' 9.7" N; 97° 27' 44.4"W [3]

obtained from the differential GPS survey. Using the locations of the radiation source and radar antenna, we deduced that the source is located at an elevation angle of 0.48° and at an azimuth of 144.61° from the KOUN1 antenna. The 3.444 km distance places the source well into the far field region (i.e., $2D^2/\lambda = 1.31$ km).

II.1.2.3 *Pattern measurement techniques*

In this section, we present the techniques used to measure the radiation patterns when the source antenna transmits the same sense polarization the KOUN1 antenna receives; this is called the copolar pattern measurements. The source is a 10 dB standard-gain horn mounted on a tripod near the center of the north wall on the roof of the Energy Center. The signal generator was set to output a signal level of +5 dBm at a frequency of 2705 MHZ (the frequency allocated for the research WSR-88D) for all measurements. A cable connecting the generator to the horn had a measured loss of 1.1 dB, which decreased the level of signal into the input terminal of the standard-gain horn to 3.9 dBm.

Since there was no readily accessible digital data to record angular positions in the RDA (Radar Data Acquisition) shelter located beneath the antenna, a digitizing recorder was attached to an available analog signal which gave a voltage proportional to the azimuth angle. This ramp voltage, along with the log-video of KOUN1's received signal and time (to a precision of about 0.1 second), were digitized at a rate between 20 and 30 Hz. Because the analog ramp voltage was contaminated by noise, the azimuthal position had an uncertainly of about 0.1 to 0.2 degrees. Thus, to obtain a calibration of voltage vs. azimuth angle, we stopped the antenna at selected azimuth angles (typically 5° apart) and averaged the analog voltages to obtain a series of average digitized voltages vs. azimuth. These averaged data fell on a straight line, and the equation of this line (an azimuth calibration equation) was used to transform sampled voltages to azimuth angle. Furthermore, in order to avoid much of the azimuthal noise in the patterns, the antenna was scanned in azimuth over a larger interval than that required, so that the scan rate within the interval of interest was relatively constant. Then, an average scan rate was computed from

---

[3]It is to be noted that the location of the KOUN1 given in the NEXRAD Site Coordinate List shows a longitude at 97°27'48", a difference of 3.6" or about 375 feet. Because of the large difference from the GPS coordinates, we have also estimated the latitudes and longitudes of the two locations using a Department of Interior Geological Survey map. The latitudes agree with the GPS measurements within 0.1", and the source longitude differed by about 0.4", whereas the KOUN1 longitude differed by about 0.9". The accuracy in reading the survey map is not expected to be better than a few tenths of a second of arc.

reference azimuths selected at clockwise and counter-clockwise extremes within which the scan rate was determined to be nearly constant from visual observations of the scan rate indicator located on the maintenance panel in the RDA shelter. The average scan rate computation was made using the azimuth calibration equation and the time that the data were recorded. Because the sampling rate was higher than the time resolution, recorded times were interpolated to obtain a more precise estimate of the time at each of the sampling points which are assumed to be uniformly spaced. Finally, the computed average azimuthal scan rate and the datum times were used to calculate the actual azimuthal position of each datum.

The log-video of KOUN1's received signal was corrupted by an occasional impulsive noise which appeared to be associated with the transmitter-amplifier's high power input signal, even though high voltage was not applied to the klystron amplifier. These impulses were subjectively removed in post processing at places where they were obvious. The digitized samples of azimuth and log-video and time were recorded on a laptop computer.

Digital data files were labeled to record the commanded elevation angles which were inputted into the computer controlling the elevation drive. The elevation angle remained constant after it reached near its commanded setting (the elevation drive was turned off after the antenna reached near its commanded position) as the antenna scanned in azimuth. Furthermore, indicated elevation angles were obtained from readouts on the maintenance panels which showed that the elevation angles were not changing during the azimuthal scans. Another temporary antenna position readout was installed by NCAR, and it was tied to the digital data stream fed into the Radar Product Generator located in a separate facility a couple hundred meters away from the Radar Data Acquisition shelter where the antenna is located. The indicated and NCAR displays and the commanded elevation angles were manually recorded in log books. Typically, there is about a 0.1° difference between the commanded and indicated elevation angles, although differences of almost 0.2 degrees were observed; it appears that the commanded angles were closer to the true elevation angles.[4]

II.1.2.4 *Pattern measurement results*

Radiation patterns as a function of azimuth were obtained for a series of elevation angles starting at zero degrees and stepping in elevation by 0.1° increments. Fig. II.4a shows the copolar radiation pattern for NSSL's research WSR-88D (KOUN1) radar, for

---

[4] Pattern measurements (30 October 1996) before the feed was replaced showed a peak in radiation was received for a commanded elevation angle of 0.45°, which is close to the true elevation angle (i.e., 0.48°) obtained from the GPS survey (Section II.1.2.2). But, after the feed was replaced (c.a. 5 December 1996), the peak signal occurred at a commanded elevation of about 0.25°. Pattern measurements made 11 June 1997 (not presented here) showed the peak signal at a commanded elevation angle = 0.27°, about the same as measured six months earlier. Shortly after 12 June, KOUN1 was struck by lightning, and many components had to be replaced. Pattern measurements made in late July and reported here showed the boresight to be at a commanded elevation angle of 0.5°.

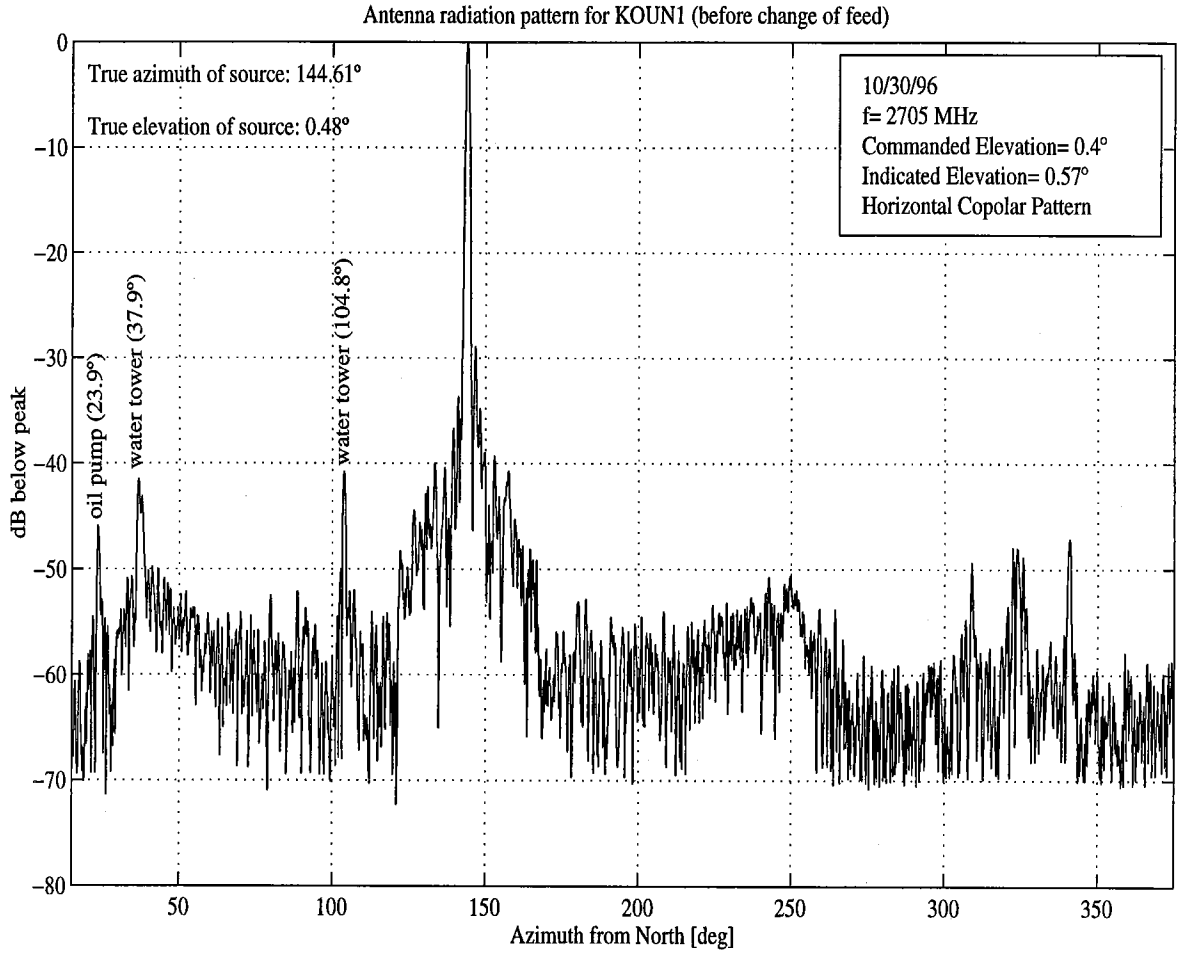

Fig. II.4 The copolar horizontally polarized radiation patterns of the KOUN1 antenna measured at NSSL in October of 1996 before changing the feed. Measurements are made at 2705 MHz, and patterns are azimuthal scans at a commanded elevation angle of 0.4°. (The boresight or beam axis is at a commanded elevation angle of 0.45°.) (a) The pattern over a 360° azimuthal scan.

horizontally polarized waves, *before the feed was changed.* Fig.II.4a is a 360° azimuthal scan for a commanded elevation angle of 0.4°. The received signals peaked at an interpolated commanded elevation angle of 0.45° and at an azimuth of 144.1° ; these are the angles which maximize the signals received from the horn atop the Energy Center, and define the boresight or beam axis. These angles compare favorably with those calculated from the GPS survey data (i.e., 0.48° elevation and 144.6° azimuth). Thus, the scan in Fig.II.4 is 0.4° below the beam axis. Because the azimuthal scan was made at a fixed non zero elevation angle, the pattern is not strictly in the same plane as the 0° cut in Fig. II.2. But differences in angular position of the two planes about the main lobe are negligibly small.

We also measured the apparent azimuth angle to the radiation source when the KOUN1 antenna was scanned both in the cw and ccw directions. The apparent azimuth changed by less than 0.1°, and thus, we conclude that backlash in the azimuthal drive is negligible.

Comparing this pattern (Fig. II.4a), measured on the site of the *KOUN1 antenna covered by the radome*, with that measured (Fig. II.2a), at Andrew Canada's range, on a newly manufactured *WSR-88D antenna without its radome*, we see general overall agreement in that the nearby sidelobes fall monotonically to a minimum of about -60 dB at about ±25° either side of the main lobe. Thereafter, sidelobe levels have an upward trend to -50 dB at about ±110°, beyond which the primary radiation from the feed and scatter from the spars are blocked by the reflector. But, in general, the KOUN1 sidelobe levels are higher. However, measurements for the KOUN1 antenna at the Norman, OK, site are made with the antenna housed in its protective radome, whereas the measurements made on Andrew Canada's range are for a newly manufactured reflector without its protective radome. Furthermore, some of prominent peaks seen in Fig. II.4a are not sidelobes at all but scatter from strongly reflecting objects such as water towers. The broad beam (beamwidth ≈ 57°) of the standard-gain horn illuminates objects far from the line of sight to the radar, and these objects scatter fields which are detected through the main lobe when KOUN1's reflector is pointed at these objects.

Two of these prominent peaks have been clearly associated with large objects seen from the KOUN1 tower, and their azimuths (indicated on Fig. II.4a) were calculated from their locations on the geological survey map. The sharply defined peak at 103.9° is associated with the water tower/tank at 104.8° (from the survey map; Fig. II.3). The water tank location obtained from the survey map is to the center of the tank, but because the tank is a cylinder which subtends an angle of about 1°, the reflecting point is likely located at a larger azimuth than to the center of the tank. Thus, the difference between the reflecting point inferred from the survey map and that observed by the radar is larger than the 0.9° difference seen in Fig. II.4a. On the other hand, the source located atop the Energy Center is at an azimuth which is 0.5° larger than the azimuth (144.1°) indicated by the radar, so some of the differences might be associated with errors in the radar observed angles.

The prominent double peak at about 37° is associated with scatter from a water tower/tank and the KCRI radar which are along a common radial line from the radar. The KCRI is a new WSR-88D radar installed in the summer of 1996 and is operated by the NWS Operational Support Facility (OSF). It is located about 959 feet (290 m) from KOUN1 and is between the water tower and KOUN1 (Fig. II.3). The center of this tank is calculated, from the survey maps, to be at 37.9° ; this difference in survey and radar indicated azimuths also suggests that there is error in the radar observed azimuth.

The distinct peak at 23.7° cannot be associated with confidence to any object seen from the KOUN1 tower. Nevertheless, there is an oil pump at 23.9° which is in the approximate direction of the peak. Although the oil pump is not very tall (i.e., less than 6 m), there is an unobstructed direct line of sight between it, the source, and KOUN1. Taller and more prominent

scattering objects (e.g., a metal warehouse at 21.8° and the Fracturing Fluid Characterization Facility at 29° ±2°, a two story building with what appears to be a metal facing at the roof line) appear too far removed from 24° to be responsible for the observed peak of radiation.

Prominent objects which could have produced the noticeable peaks between 309° and 341° have also not been identified with a high degree of confidence. The most prominent structure near the azimuth at 309° appears to be the Norman Doppler radar. But it is at an angle of about 301°. Although this is a large difference, the Norman Doppler radar is only 440 feet from the KOUN1 radar. Thus, it subtends an angle of at least 4°, and because it is estimated that the accuracy in site locations is about ±100 feet when read from the survey map, the angular error for structures at this near distance is about ±10°. Therefore, it is possible that the Norman Doppler radar is responsible for the peak at 309°.

The cluster of peaks about 324° are 180° from the main beam, and the only structures in this direction are large metal buildings on the airport; these buildings are about 1600 feet away and have a side with an orientation almost perpendicular to the line-of-sight to the radar. The lobe at about 341° appears to be associated with the York International manufacturing plant three and a half miles away.

Thus, many of the peaks seen in the pattern, especially those below about -40 dB, are not associated with sidelobes but are signals scattered from ground objects into the main lobe (i.e., the radar beam). Nevertheless, prominent peaks of radiation near the main lobe are likely to be antenna sidelobes. Thus, it appears that sidelobes of the present antenna with a radome are larger than that measured by Andrew Canada on their antenna range using a WSR-88D antenna with a partially assembled radome.

Shown on Fig. II.4b is the envelope (dashed lines) of the peak sidelobe level measured by Andrew Canada (Fig. II.2b). Comparison of the sidelobe levels in Fig. II.2b with that in Fig. II.4b suggests that nearby sidelobe levels of KOUN1 are about 2- 4 dB larger. As pointed out in Section II.1.1, some (1-2 dB) of this increase can be due to the radome. Thus, the near sidelobe levels of the KOUN1 antenna appear to be 1-2 dB higher than those expected of newly manufactured reflectors inside their protective radome.

It is not known whether the 1-2 dB higher sidelobe levels are due to changes in the antenna upon assembly at the site, deterioration of the reflector surface due to aging of the antenna (the KOUN1 was installed at NSSL in 1988, giving it an age of about 8 years at the time of measurement), the inferior antenna range, or some other factors[5]. Variability of patterns from

---

[5] At the time of the pattern measurements, it was noted that a waveguide spar was missing a strip of absorbing material intended to reduce scatter. The absorbing strip is placed on the narrow under side of the waveguide; the broad side walls are exposed to the secondary radiation. Furthermore, the reflector and some of its supporting back members had a few dents. These, and other distortions in the reflector's surface, could be responsible for enhancing the sidelobe levels.

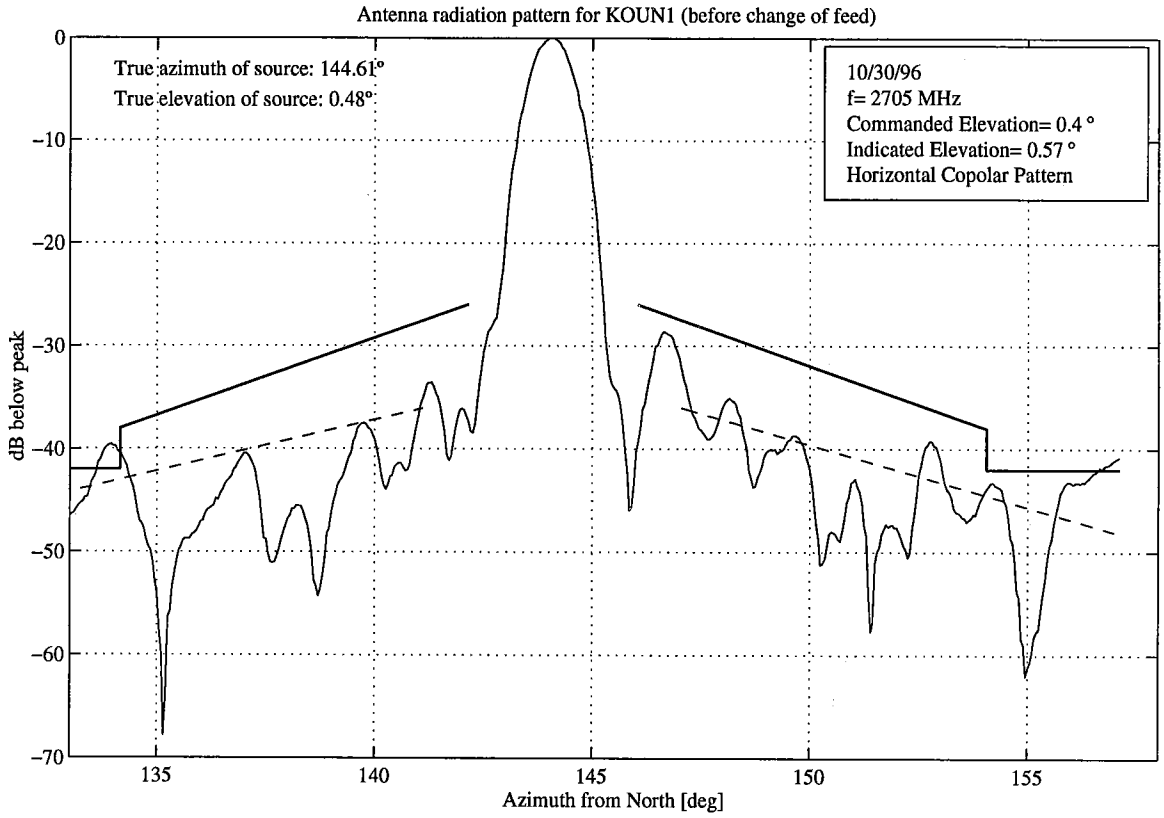

Fig. II.4 (b) The pattern over a ±13° interval. The solid lines are the specified limits for sidelobes; the dashed lines, obtained from Fig. II.2b, are the estimated sidelobe envelopes of a newly fabricated WSR-88D without radome.

antenna to antenna, even immediately after manufacturing, might also account for some of the differences. Comparison of antenna patterns for three WSR-88D reflectors, all measured on Andrew Canada's antenna range after manufacturing, shows that the first sidelobe levels differ by as much as 6.5 dB, and the second sidelobe levels differ by as much as 5.5 dB. Nevertheless, the envelope of the near sidelobes of these three antennas appears to have changed by less than 1 dB. Thus, it is expected that variability from antenna to antenna will not accont for more than 1 dB of the estimated 1-2 dB difference.

The first few sidelobes about the main beam meet specifications (solid line, Fig. II.4b) for the WSR-88D radars with radomes. The peaks at 133.5° and 157° exceed specifications, but as pointed out earlier, apparent sidelobes at levels below about -40 dB might be associated with scatter from the terrain. (See Section II. 6.3 for additional support for this conjecture.)

The pattern of the main lobe of the KOUN1 antenna is in Fig. II.4c, and this is to be compared with the pattern in Fig. II.2b (right side) which was measured on Andrew Canada's antenna range. Also plotted (dashed line) is the Gaussian function, least squares fitted (on the linear scale) down to the -20 dB level. Both the peak location and the width of the Gaussian function were varied to obtain the best fit. The 3 dB beamwidth of this fitted Gaussian is 0.89°, which compares favorably with the 0.92° width obtained from Fig. II.2b. Even at the -20 dB level, the two widths nearly agree (2.24° vs. 2.14° in the measured patterns), and the prominent null at +1.8° (Fig. II. 4c) with a weaker null at -1.8° compares favorably with that observed on the Andrew Canada range (Fig. II.2b). It is not known whether the favorable comparisons in null depths is coincidental, but the fact that it is observed on both ranges, and with and without radome, suggests it might be related to the antenna. This is a remarkable agreement considering that the antennas are not the same, and the measurements were made on different ranges.

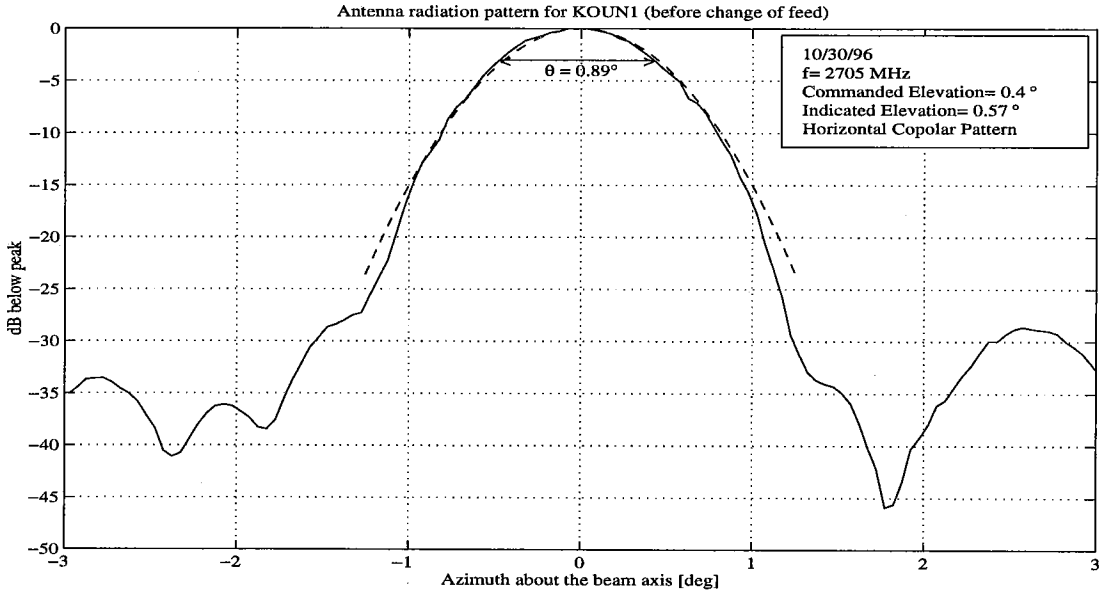

Fig. II.4 (c) An expanded view of the main lobe with a scale centered about the boresight. Dashed line is a Gaussian function least squares fitted on a linear scale (to 0.01).

Figs.II.2 and II.4 show the pattern only along a single cut. Since we were unable to rotate the antenna reflector about its axis to obtain patterns at other cuts, we have scanned the antenna in azimuth for a series of 0.1° elevation angle steps. Furthermore, the antenna's elevation scan is limited from -0.5° to about 45°. Thus, we are only able to measure the sidelobe levels about the main lobe on the lower side of the 0° cut. Fig. II.4d shows a contour map of radiation pattern levels for the lower side in 5 dB steps (starting at -15 dB below the peak of the main lobe) for the azimuthal interval ±10° about the beam axis. The irregularities of the contours surrounding the main lobe are likely due to measurement and quantization noise and are not indicative of fluctuations in the true pattern shape which this plot suggests to be circularly symmetric. The pattern also shows evidence of enhanced sidelobe levels along cuts at 0°, 60°, and 120° clockwise

from the +azimuth axis; this is where sidelobes are expected to be enhanced due to blockage by the spars (Fig. II.1).

Comparisons of the nearby sidelobe levels seen along the 0° cut (e.g., Figs.II.2b or II.4b) with those made by Andrew Canada along the 30° cut (i.e., 30° counter clockwise from the 0° cut; Fig. II.4e) show significantly higher sidelobes along the 0° cut; this is consistent with an enhanced ridge of sidelobes due to blockage by the spars. That the ridge has a series of deep nulls is likely due to interference with radiation patterns associated with (1) blockages by the feed and the other pair of spars, (2) scatter from the sides of the spars, (3) irregularities in the surface of the reflector, and (4) the illumination of the reflector.

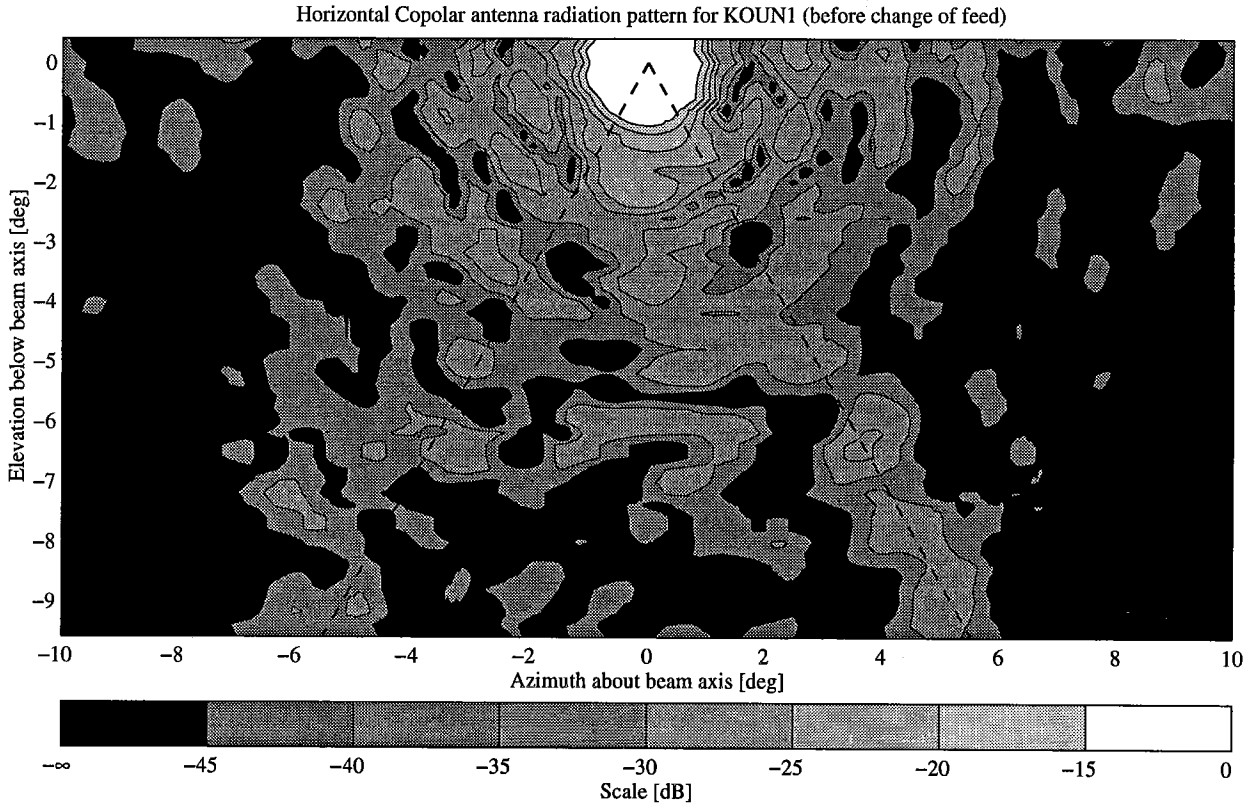

Fig. II.4 (d) A contour map of the copolar radiation pattern for horizontally polarized waves (before change of the KOUN1 feed). Contour intervals are 5 dB, starting from -15 dB below the peak to -45 dB. The dashed lines are the cuts along which sidelobes are expected to be enhanced due to spar blockage.

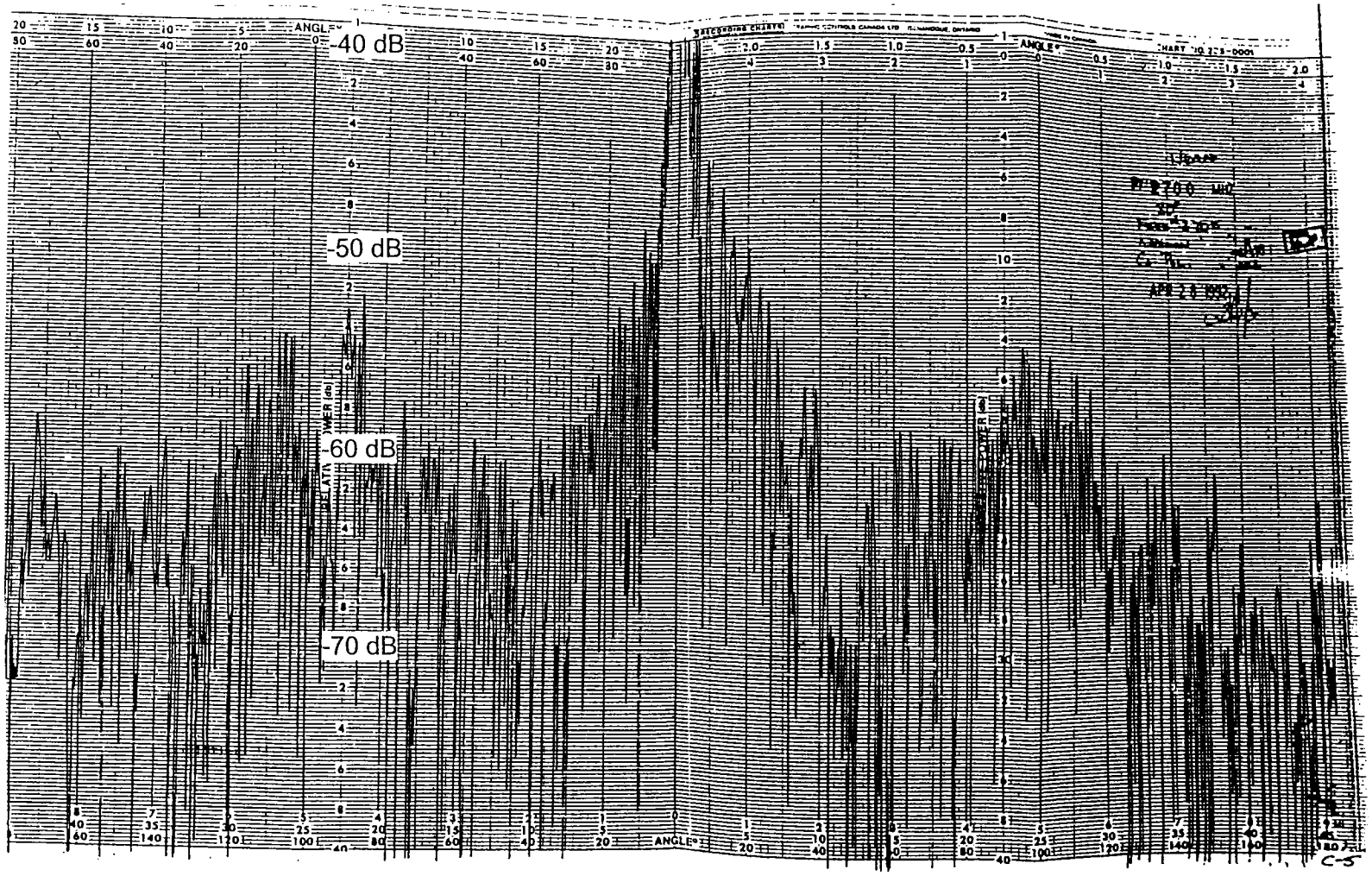

Fig. II.4e The 30° cut copolar pattern measured by Andrew Canada Inc. for a WSR-88D antenna.

II.2. Three- vs. four-spar feed support assembly

Early in the planning for modifications to the WSR-88D radar for conversion to a polarimetric Doppler weather radar, considerations were given to changing the feed support spars from a three- to a four-legged configuration. The rationale for changing to a four-legged assembly, in which spars are 90° apart and along lines 45° relative to the vertical and horizontal planes of polarization (Fig. II.1b), is to ensure symmetry of the spars relative to the directions of polarizations. This should help to match the radiation patterns for each of the polarizations; it has been suggested that artifacts in differential reflectivity fields are related to the mismatch of sidelobes in high reflectivity gradient regions (Chandrasekar and Keeler 1993). The blockage of secondary radiation by the spars creates a ridge of enhanced sidelobes in planes perpendicular to the spar's projection onto the aperture of the reflector. Thus, the three-spar support assembly generates three ridges of enhance sidelobes (Fig. II.1a), whereas the four-spar assembly generates only two ridges (Fig. II.1b).

Although the use of four spars spaced 90° apart reduces the number of ridges to two, the area over which the illumination is blocked is increased if everything else (e.g., spar width) is equal. Because each pair of spars in the four-spar assembly has projections that are twice longer than the projections of each of the spars in the three-spar assembly, the sidelobe enhancement along the ridge should be 6 dB.

Researchers at Colorado State University (CSU), the National Center for Atmospheric Research (NCAR), and NSSL have opted for a four-spar feed support assembly for their polarimetric antennas. The CSU reflector diameter is the same as that for the WSR-88D antenna, but its focal length to diameter ratio is 0.446 (vs. 0.375 for the WSR-88D). The CSU antenna radiation patterns for the antenna without radome (Radiation Systems Inc. 1993) are given in Fig. II.5. Fig. II.5a is the radiation pattern for the same polarization (horizontal) and pattern cut (0°), as shown in Fig. II.2a which is for the 3-spar WSR-88D antenna.

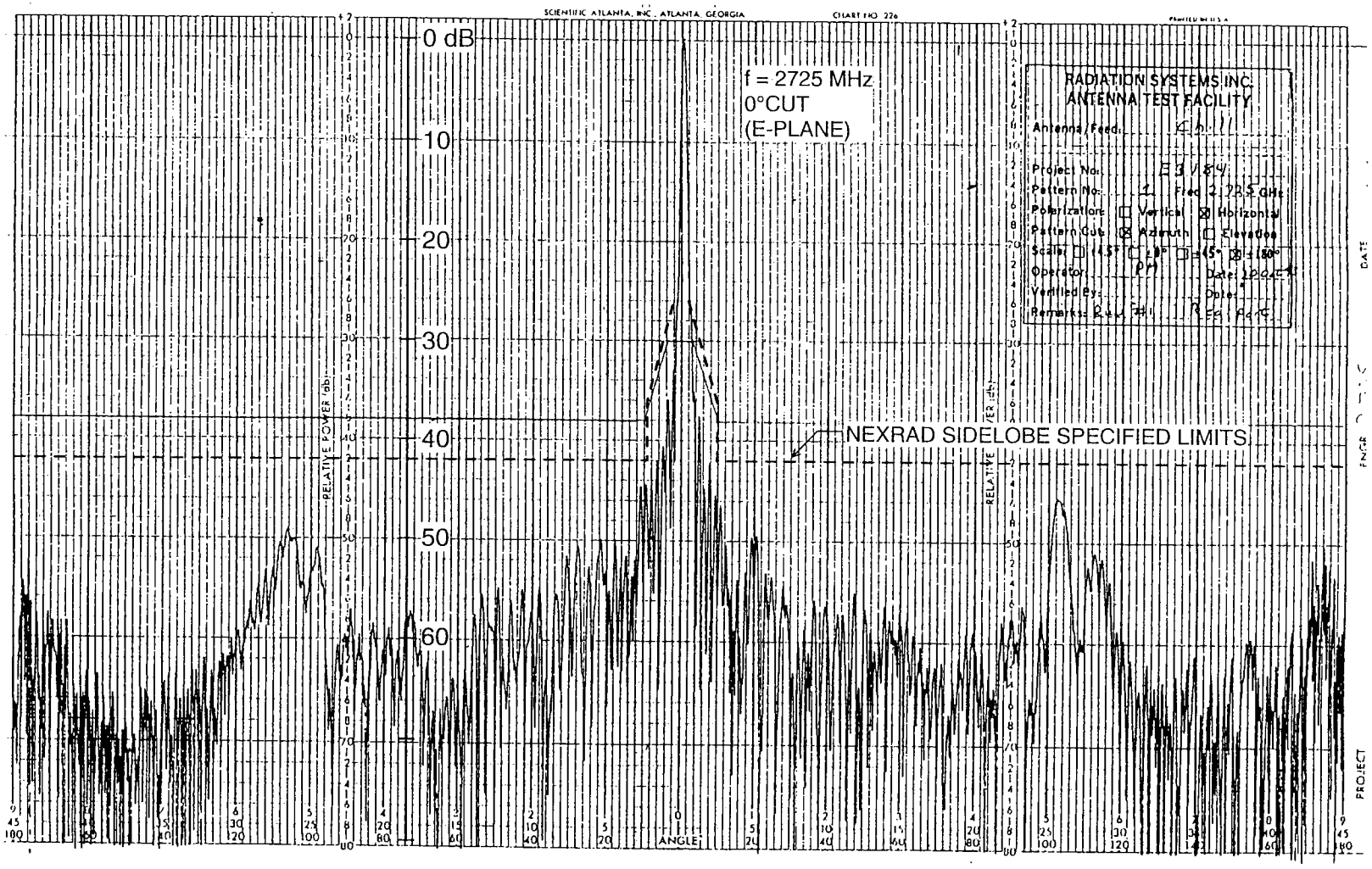

Fig. II.5 The copolar radiation pattern, for reception of horizontally polarized waves, as a function of azimuth for the CSU antenna having a four-spar feed support. The specified limits on the sidelobes for the NEXRAD antenna are given by the dashed lines; the solid lines are the sidelobe limits specified for the CSU antenna. (a) the pattern along the 0° cut; this cut is midway between the expected ridges of enhanced sidelobe levels due to blockage by the spars.

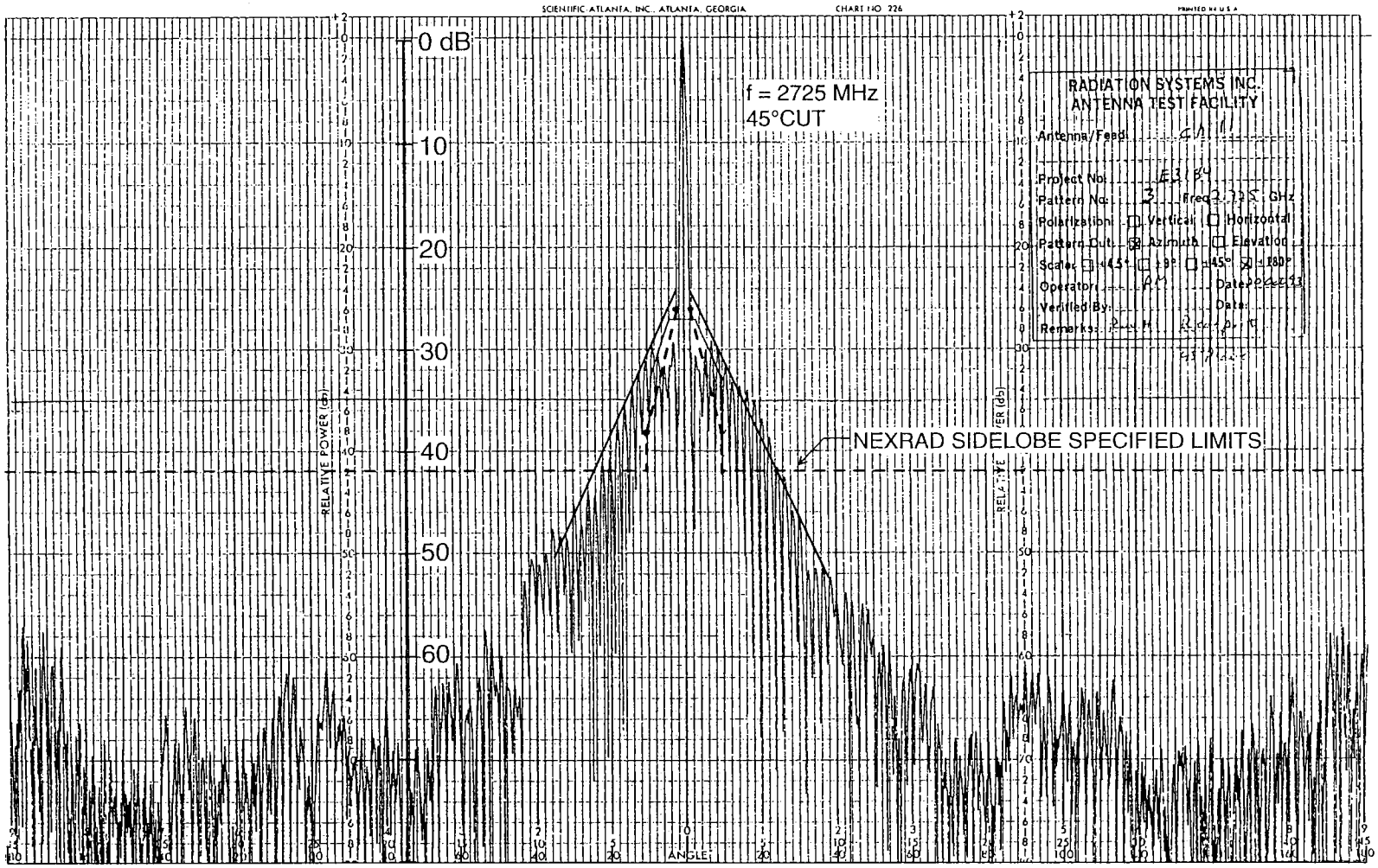

Fig. II.5 (b) the pattern along the 45° cut where enhanced sidelobes are expected.

Because the reflector diameters of the WSR-88D and the CSU antennas are the same, we should expect to see strong similarities in these patterns. But, for example, the one-way 3 dB beamwidth and main lobe gain on the CSU antenna are 1.00° and 44.6 dB vs. 0.92° and 45.6 dB[6]. Furthermore, the sidelobes (Fig. II.5a) near the main beam of the CSU antenna pattern are significantly lower than that seen for the WSR-88D antenna (Fig. II.2a). For example, at about the ±15° azimuth, the sidelobe levels of WSR-88D antenna are about 50 dB below the main lobe peak, whereas the CSU antenna's sidelobes are about 55 dB below its main lobe peak. But the WSR-88D pattern is along a cut for which one expects enhanced sidelobes due to spar blockage, whereas the CSU antenna pattern, although along the same cut, is between expected ridges of enhanced sidelobes (Fig. II.1b). Examination of the patterns along the ±45° cuts of the CSU antenna (Fig. II.5b) show that the sidelobe levels of the CSU antenna far exceed the NEXRAD specifications and are significantly worse than that of the WSR-88D pattern.

The radiation patterns of the four-spar CSU antenna and pattern measurements for the NCAR antenna (Chandrasekar and Keeler 1993) clearly show the presence of ridges of enhance sidelobe levels in planes perpendicular to the spars, but they are 12-16 dB higher than those for the three-spar configuration (compare Fig. II.2b with Fig. II.5b; both antennas without radomes). For example, at ±15° azimuth, the CSU antenna sidelobe level exceeds the NEXRAD specifications by 6-8 dB, whereas the WSR-88D antenna's sidelobes are 6-8 dB lower than these specifications. The level of enhancement is larger than the expected 6 dB, and this unexpected increase might be related to the fact that the waveguides of the CSU antenna are mounted to spars which have a slightly larger cross section than the waveguide, whereas in the WSR-88D assembly, the waveguides are the spars. Because waveguides are mounted to the feed support spars on the CSU antenna, there is a much larger area of metal which could scatter more of the secondary radiation. Furthermore, there is also some blockage of primary radiation in the CSU antenna because the spars are mounted inside the diameter of the reflector.

Because the higher sidelobe levels associated with the four-spar feed support assembly exceed the sidelobe level specifications for the WSR-88D radiation patterns, we have decided to keep the three-spar configuration. This configuration establishes a baseline of performance that could be used as a point of reference if a decision is made to convert all 164 WSR-88D radars to have a polarimetric capability. We have opted for lower sidelobe levels and accepted a risk that patterns of horizontal and vertical (H, V) polarizations might not be matched as well as that in a four-spar configuration. If sidelobe levels are sufficiently low, however, differences in H, V sidelobes shouldn't matter.

---

[6] An estimate of the KOUN1 antenna gain is obtained from Andrew Canada's report and is derived from calculations of directivity obtained from pattern measurements and estimates of waveguide and feed losses, whereas the CSU antenna gain is measured by comparing signal levels obtained with a standard-gain horn mounted on the same pedestal as the CSU antenna. This, and differences in the primary radiation patterns, might account for the differences in gain and beamwidth.

II.3. The dual port feed

Andrew Canada Inc. fabricated a feed to provide a pattern of radiation identical to the single polarization (i.e., horizontal) feed used on the WSR-88D antennas, but with the addition of a port to excite vertically polarized waves. A bottom view sketch of the dual port feed is shown in the upper right corner of Fig. II.6. Thus, the front port is on the bottom side of the feed, and it produces horizontally polarized waves (i.e., the polarization is in the plane of the figure and perpendicular to the feed axis). The front port has the same configuration as the present single port feed on the WSR-88D radars, and the new feed produces horizontally polarized waves, as does the WSR-88D feeds. But on the dual port feed, the front port is placed about 2 inches closer

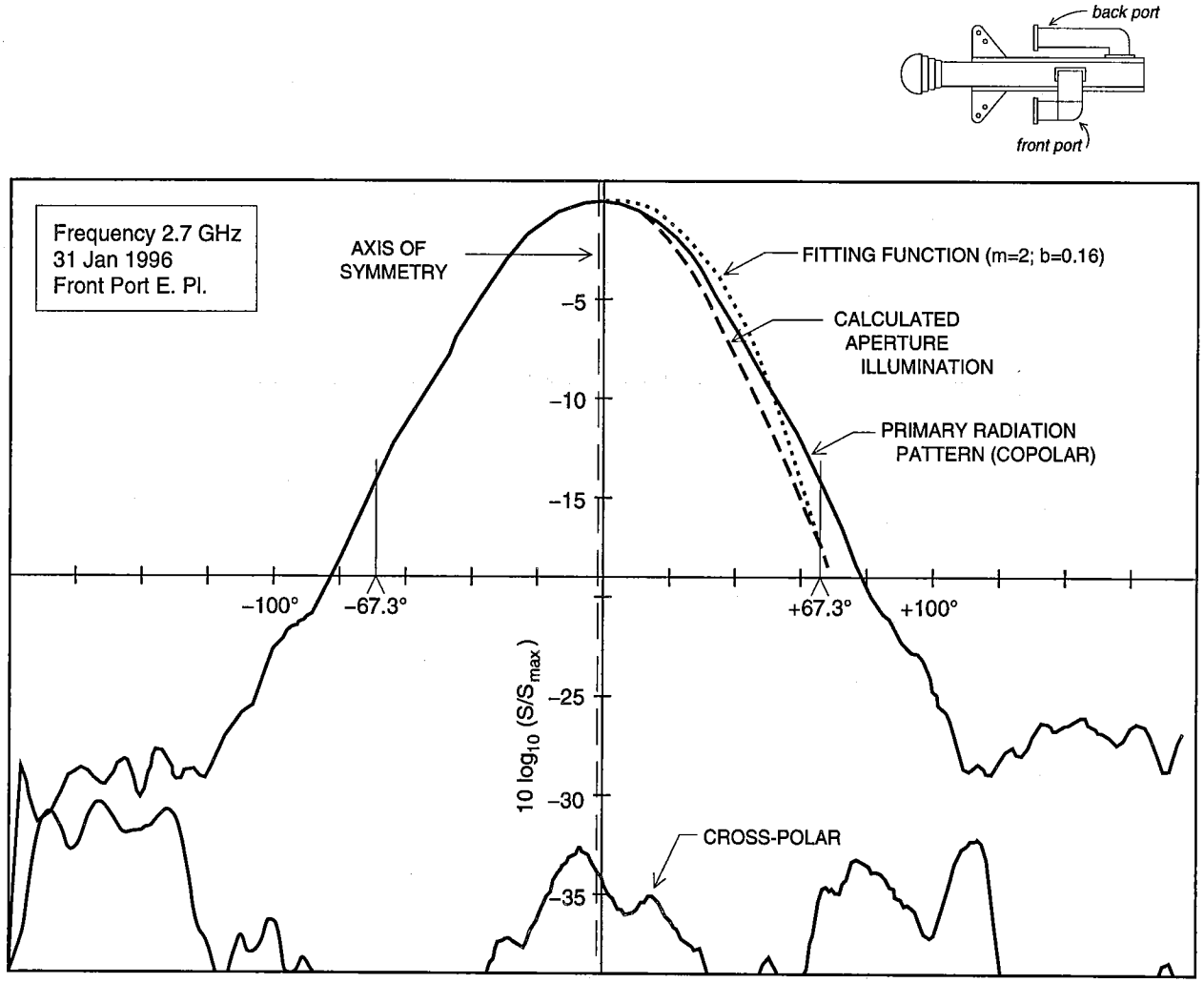

Fig. II.6 The 0° cut radiation patterns (copolar and cross-polar) for the dual port feed (bottom view sketch of this feed is in upper right corner of this figure) with the front port energized (i.e., to receive horizontally polarized waves). This figure is adapted from measurements made in Andrew Canada's anechoic chamber. Parameters *m, b* of the fitting function are defined in (II.1).

to the feed aperture, and the back port is about 5 inches away from the front port. Thus, the overall length of the feed increased only by about 4 inches, which still provides adequate clearance between the feed and the radome.

The back port of the dual port feed is located on the side of the feed, and it produces vertically polarized waves. This port appears to be a replica of the front port but simply rotated 90°. The 2.7 GHz 0° cut copolar H pattern of the dual port feed, for horizontally polarized waves of primary radiation, measured in Andrew Canada's anechoic chamber, is given in Fig. II.6. The copolar H pattern (not shown here) along the 90° cut for the front port has the same shape but is slightly broader (114° vs. 109° at the -10 dB level), consistent with theoretical patterns of the TE_{11} mode radiating from a circular aperture (Fradin 1961, Fig. 4.7); thus, the illumination at the edge of the reflector along the 90° cut is about 1 dB higher than that along the 0° cut.

The pattern of the cross-polar radiation is also plotted on this figure. We should expect a null along the principal planes (i.e., the planes, through the beam axis, containing the Electric "E", or Magnetic "H" field vectors) for radiation from a circular waveguide (Fradin 1961, p. 399). But there is radiation along these planes at levels about -30 dB and smaller relative to the copolar peak. Unfortunately, we do not have pattern data from other planes to establish whether these levels are representative of a null line (i.e., we should expect enhanced cross-polar radiation in regions away from the principal planes). The cross-polar radiation at a level of about -34 dB along the beam axis (the cross-polar radiation in the H-plane and along the beam axis is about 2 dB stronger) could be due to the cross-polar signal (i.e., vertically polarized signal) generated at the front or H port or generated elsewhere within the circular waveguide of the feed. It should be noted that the cross-polar pattern measurements were made after the source was rotated to an angular position (nearly 90° from the copolar position) until a minimum signal was obtained.[7] The coupling from port to port is, on average, measured to be about -43 dB, which suggests that the cross-polar signal is not generated within the circular guide of the feed but could be excited at the tapered portion leading to the feed's aperture. On the other hand, some of the cross polarized signals observed in this figure could be a result of scatter from the walls of the anechoic chamber which have a "silence level" of about -40 dB[7]. The 2 dB larger cross-polar signal along the beam axis for the H-plane measurements (it should equal the peak in the measurement along the E-plane) attests to the difficulty in making pattern measurements of the relatively weak cross-polar signals.

The patterns for the back port (i.e., the vertical polarization port) are identical to that of the front port. Pattern measurements were also made at 2.85 and 3.0 GHz, and the expected decrease of beamwidth at the higher frequencies was noted. The return loss for the front and back ports was measured to be less than -18 dB over the band of frequencies from 2.7 to 3.0 GHz.

---

[7] Personal communication from Mr. Ray Boyko, Andrew Canada, c.a., Jan. 1997.

II.4. Measurements of the dual port feed position

After installing the dual port feed and a waveguide spar to feed the back (vertical) port, measurements were made to determine the position of the feed axis relative to the axis of the reflector. Distances from reference holes on the feed to three points at the reflector edge near each of the spars were measured with a steel tape. From these measurements and measurements of the feed, it was established that the feed axis was displaced perpendicularly from the reflector axis (the axis of the reflector is horizontal) by 0.16" in the x (horizontal) direction and -0.22" in the y (vertical) direction; x and y are in a right handed coordinate system, with z directed along the reflector's axis from its vertex to its focal point.

For such small displacements, the beam's angular displacement from the reflector axis is opposite and equal to the angular displacement of the feed times the Beam Deviation Factor. The angular displacement of the feed is the angle between the axis of the reflector and the line drawn from the feed's center to the vertex of the reflector. The Beam Deviation Factor = 0.87 for a focal length to diameter ratio of 0.375 (Sengupta and Hiatt 1970, Fig. 10-10). Thus, the azimuth and elevation displacements of the beam are about 0.06° and 0.09°. These displacements are much smaller than a beam width and are negligible; the corresponding loss in antenna gain is also negligible (Sengupta and Hiatt 1970, Figs.10-11).

If the single port feed, originally installed on the KOUN1, was positioned on-axis (there are no records giving the location of the original feed), the pattern measurements (Fig. II.4) made before the change in feed would indicate an azimuth (elevation) angle to the radiation source which would belarger (larger) than that measured after the change of feed. The azimuth to the radiation source before the change of feed is 144.1° (Fig. II.4b), and after the change it is 144.2° (Section II.6.1, Fig. II.8b). Although this 0.1° difference is small, it is in a direction opposite than one would expect from the measurements of the dual port feed position. Nevertheless, considering that the accuracy of azimuth positioning is likely no better than about ±0.1°, and that there is no record of the original single port feed location, the two azimuths are in near agreement. On the other hand, the elevation angle to the radiation source did decrease, after the feed change, by about 0.1° (compare the commanded elevation angles in Figs. II.4b and II.10a), as expected if the single port feed was on-axis.

The focal plane was measured to be 3/16" behind (i.e., in a direction away from the reflector's vertex) the plane of the feed's aperture.

II.5. Comparison with a theoretical radiation pattern

In order to support the deductions that the near sidelobes are principally due to blockages and scatter from spars and irregularities of the reflector's surface, we calculated the sidelobe levels neglecting blockages, scatter, and surface irregularities. This calculation gives the lower limits of what could be achieved in the sidelobe levels if changes were made to the antenna (e.g., changing the feed support structure to reduce spar cross sections, checking surface tolerance, and

if necessary, readjusting the reflector panels, etc.). We use diffraction theory to compute the radiation from an aperture with a specified distribution of circularly symmetric illumination across it (Sherman 1970).

The dashed line in Fig. II.6 is the calculated aperture illumination which accounts for the decrease in illumination (solid line) from the feed because of the larger distance to the edge of the reflector versus that to its vertex. The angle between the axis of the reflector and the line drawn from the focus to the reflector's edge is 67.3°. (The ±67.3° marks drawn on this figure are relative to the axis of symmetry.) Thus, the edge illumination is about -17.2 dB.

To estimate the radiation pattern for an aperture illuminated with a distribution described by the dashed line requires numerical evaluation of a Hankel Transform. But, we can obtain an estimate of the radiation pattern by fitting the illumination function with an equation for which the radiation pattern is known. This equation for the electric field illumination function has the general form (Sherman 1970, pp. 9-21):

$$E\left(\frac{\rho}{\rho_o}\right) = \left[1-\left(\frac{\rho}{\rho_o}\right)^2\right]^m + b, \qquad \text{(II.1)}$$

where ρ is the radial distance from the beam axis, ρ_0 is the distance to the reflector's edge, m is a parameter having values typically ranging from 1 to 3, and b gives the illumination intensity at the reflector's edge.

The following normalized power density $S_n(\theta)$ across the aperture is derived from (II.1)

$$S_n(\theta) = 20\log_{10}\left[\frac{\left(1-\dfrac{(2f)^2(1-\cos\theta)^2}{(\rho_o\sin\theta)^2}\right)^m + b}{1+b}\right], \quad \textit{for } \theta \le 67.3^o, \qquad \text{(II.2)}$$

where θ is the angle subtended by the line connecting the vertex to the focus and the line drawn from the focus to a point on the surface of the reflector. Next, this aperture illumination function will be compared with that calculated from measurements (dashed line in Fig. II.6). Note that the amplitude of the feed's field, say at a point A where the reflector would be placed, is the same in the aperture plane at the point which lies on a line passing through point A and parallel to the axis of the reflector (Fradin 1961, p. 381). The factor raised to the m^{th} power goes to zero at the reflector's edge (i.e., at $\theta = 67.3°$), so b is determined by the edge illumination (i.e., $b = 0.16$ corresponding to -17.2 dB of edge illumination reported in Fig. II.6). Substituting the focal length of the KOUN1 reflector (i.e., 320 cm) and its diameter $2\rho_0 = 853$ cm into (II.2), we have

plotted equation (II.2) in Fig. II.6 for $m = 2$; we see that we have a reasonably good fit near the reflector's edge and along the beam axis, and the largest difference is at the midpoints.

The composite electric field radiated by the aperture is a sum of the fields due to the factor raised to the m^{th} power in (II.2) (i.e., the tapered illumination part) and that due to the uniform illumination (i.e., b in II.2). The radiation patterns, corresponding to these two functions illuminating a circular aperture, are given by Sherman (1970). Summing these two electric field patterns (for $m = 2$, and $b = 0.16$) and normalizing, we obtain the theoretical radiation pattern of power density

$$S(u) = 20 \log_{10} \left[\frac{\frac{48 J_3(u)}{u^3} + \frac{0.32 J_1(u)}{u}}{1.16} \right], \qquad \text{(II.3)}$$

where

$$u = \frac{2\pi \rho_o \sin\theta}{\lambda}, \quad 2\rho_o = 8.53\, m, \quad \lambda = 0.111\, m\,. \qquad \text{(II.4)}$$

Note that blockages and surface irregularities are not included in (II.3).

Eq.II.3 is plotted in Fig. II.7 (lower solid line) and compared with the envelope of sidelobes (dashed line) measured by Andrew Canada for the same polarization but from a pattern (not shown here) along a 30° cut. The 30° cut was chosen from the Andrew Canada's pattern file because it is not practical to obtain a 30° cut pattern measurement on the KOUN1 antenna and, furthermore, it is this pattern which lies midway between the ridges of high sidelobes due to blockages by the spars. Therefore, the 30° cut pattern should be closer to the theoretical pattern which ignores all blockages as well as irregularities of the surface. Measured sidelobe levels are not circularly symmetric and do not show any consistent dependence on angle away from the main lobe. Therefore, the envelope shown in Fig. II.7 was obtained from the side of the 30° cut which exhibited a more uniform trend of sidelobe levels; the assumption is that this side of the cut was less affected by artifacts of the antenna range.

The first few sidelobes are principally due to the tapered component of the illumination function, and they exhibit a relatively fast decay as a function of angle, whereas the sidelobes at angles larger than 4° are principally due to the uniform component of the illumination function, and these sidelobes have a much slower decay with increasing angle. The higher measured sidelobes are attributed to the blockage and scatter from the feed, its spars, and irregularities in the surface of the reflector.

Also plotted in Fig. II.7 is the pattern measured at the KOUN1 site after the new feed was installed (see Section II.6 for more data and discussion on pattern measurements with the new feed). From this figure, we see that the theoretical pattern agrees quite well with the pattern

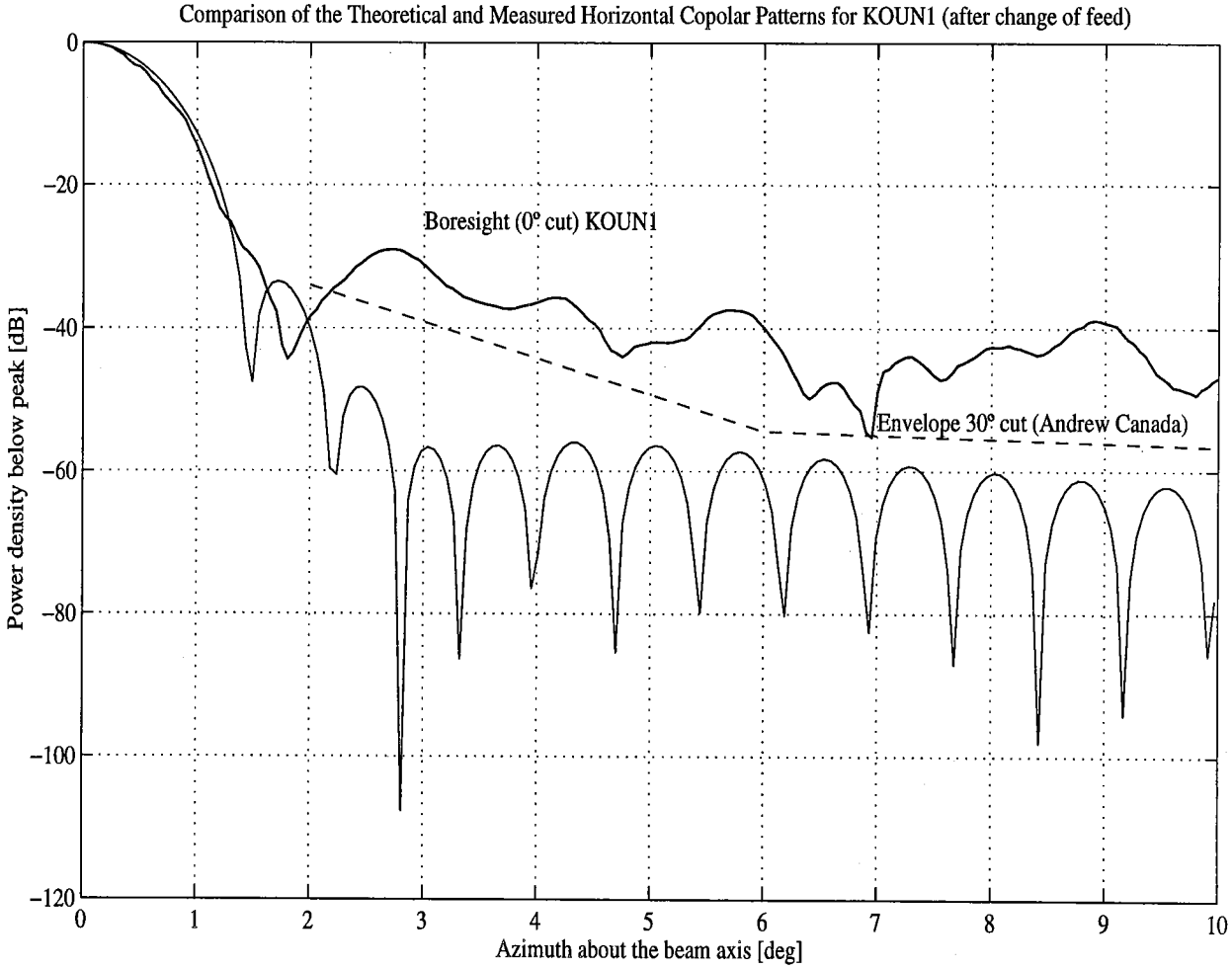

Fig. II.7 The theoretical radiation pattern (lower solid line) of the KOUN1 antenna neglecting blockages and reflector irregularities. Also shown is the copolar pattern (upper solid line), for reception of horizontally polarized waves, measured (0° cut) with the KOUN1 antenna after the new dual-port feed was installed. The dashed line is the envelope of the sidelobes (30° cut) measured by Andrew Canada for a WSR-88D antenna without radome.

measured (after the feed change) down to the -25 dB level. As pointed out in Section II.1.2, the sidelobes measured along the 0° cut for the KOUN1 antenna are several dB larger than those measured along the 30° cut because the pattern at the 0° cut passes through the ridge of enhanced sidelobes, due to spar blockage, and because sidelobes measured at the KOUN1 site are a few dB larger (partly due to the radome) than those measured at the Andrew Canada range when patterns along the same cut are compared (Section II.1.2). It is concluded that the analytical expression given by (II.3) adequately describes the main lobe of the measured radiation pattern and also shows that there is a possibility to reduce sidelobes significantly if needed. For example, the top spar which does not carry signals to the feed could be replaced with one having a smaller cross section; this would reduce the sidelobe levels a few dB along the ridge perpendicular to this spar (i.e., the 0° cut, Fig. II.1a). Furthermore, covering the sides of the waveguide spars with a thin layer of absorbing material (i.e., similar to that presently applied to the under or narrow wall side of the two waveguide spars) could reduce scatter from the spars and lower the antenna sidelobes.

A simple formula to derive θ_1, the 3 dB width of the beam obtained from (II.3), is

$$\theta_1 \approx 1.4\frac{\lambda}{D}, \tag{II.5}$$

and the angular diameter θ_0 of the first null circle is about

$$\theta_0 \approx 4\frac{\lambda}{D}. \tag{II.6}$$

The angular diameter of the first null circle defines the main lobe or beam of the antenna. Substituting the wavelength (0.111m) and diameter values into (II.5), this simple formula gives $\theta_1 \approx 1°$, which is larger than that measured (i.e., $\approx 0.9°$) which is also seen from the graphs in Fig. II.7. The angular diameter of the null obtained from (II.6), however, is smaller (i.e., $\theta_0 \approx 1.5°$) than that measured (i.e., $\approx 1.8°$).

It can also be shown (Sherman 1970, Fig. 11) that, for the parameters (i.e., m = 2; b = 0.16) corresponding to the theoretical pattern, about 99% of the radiated power would be transmitted through the main lobe. By integrating the power over the main lobe (i.e., the pattern within 1.8°) and the power over the sidelobes out to ±10°, we find that 97% of the power is within the main lobe; a lower value should be expected if the sidelobes where integrated over the entire angular domain. The somewhat lower measured value of 97% instead of 99% is due to the larger sidelobes associated with blockage and scatter from the feed and its supporting spars, distortions in the reflector's surface, scatter from the ground which increases the sidelobe levels on average, and errors in approximating the measured illumination function (Fig. II.6).

II.6. Radiation pattern measurements for the KOUN1 antenna after installation of the dual port feed

Using the same setup as described in Section II.1.2, pattern measurements for both the horizontal and vertical polarizations were made after the new dual port feed was installed. When measurements are made of the copolar and cross-polar patterns, the port which is not connected to the receiver is terminated with a matched impedance. The standard gain horn is leveled to transmit either horizontally H or vertically V polarized waves; that is, we did not rotate the horn to obtain a minimum or maximum in cross-polar or copolar signals when the KOUN1 beam was boresighted on the source. Therefore, any misalignment, or rotation of KOUN1's feed about its axis from its nominal position, will result in a coupling of either the H or V source radiation into the V or H ports of KOUN1's dual port feed. Calculations presented in Section II.6.7 are used to estimate the amount of rotation or tilt of the polarization ellipse caused by inadvertent rotation of the feed. Measurements reported in this section indicate that the rotational uncertainties in the installation of the feed are within the measurement accuracy (about $\pm 0.1^{\circ}$). Uncertainties in feed axis position in the plane perpendicular to the reflector's axis are presented in Section II.4.

II.6.1 Copolar measurements for the front (H) port

Fig. II.8a gives the copolar pattern for horizontally polarized waves after the new dual polarized feed had been installed. Compare this pattern (Fig. II.8a) for horizontal polarization with the one in Fig. II.4a because both should ideally be the same. The two patterns agree remarkably out to the first sidelobes, and thereafter, there is general similarity, although the magnitudes of sidelobes and scatter from objects changed a few dB. Note that the commanded elevation angle is set at 0.5° for the data presented in Fig. II.8a; this corresponds to the boresight elevation angle but differs from that for data collected earlier (i.e., see Figs.II.4a,b; the horizontal copolar pattern data collected in December did not include a full 360° scan, and therefore, Fig. II.8a data had to be collected in late July, 1997) because components were changed in the antenna system after a lightning strike which occurred in mid June 1997.

To ease the comparison of the important sidelobes near the main lobe, we have plotted in Fig. II.8b the data collected on December 5, 1996, on the same stretched scale ($\pm 13^{\circ}$) as the pattern plotted in Fig. II.4b which is the pattern for the single port feed. Comparing Figs.II.4b and II.8b, it is apparent that the two patterns are nearly the same; there are places in the sidelobes where the new pattern shows increases and decreases of a few dB relative to the secondary radiation pattern measured with the single port feed. Some of this could simply be due to the fact that the elevation angles are not precisely the same in these two data sets. For example, the elevation angle (0.4°) for data collected for Fig. II.4b was 0.05° below the elevation angle of the boresight (i.e., at 0.45°; see footnote, Section II.1.2.3), whereas for the data collected for Figs. II.8b, the elevation angle (0.30°) was 0.03° above the elevation of the boresight (i.e., at 0.27°); all angles here refer to the commanded ones.

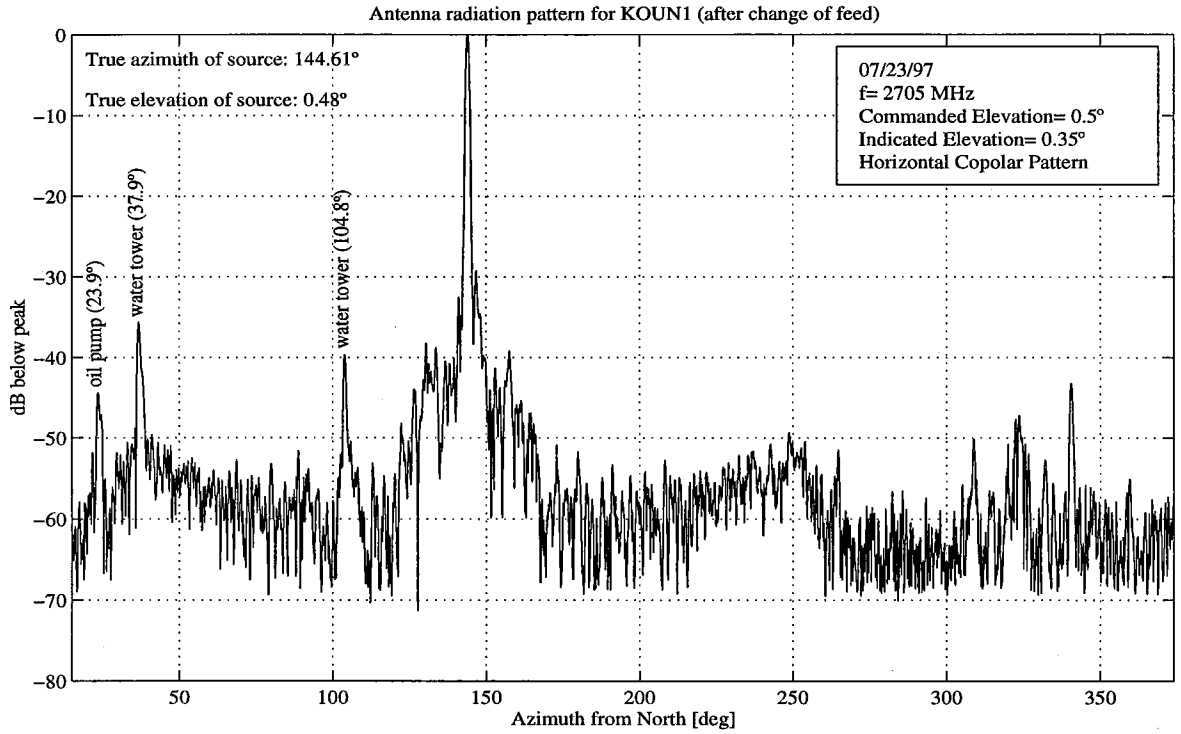

Fig. II.8 (a) The 0° cut pattern through the boresight (commanded elevation angle is 0.5°) for a scan of KOUN1 copolar H radiation after the dual-port feed was installed. (The beam axis is at a commanded elevation angle of 0.5°.) The front port is connected to the receiver.

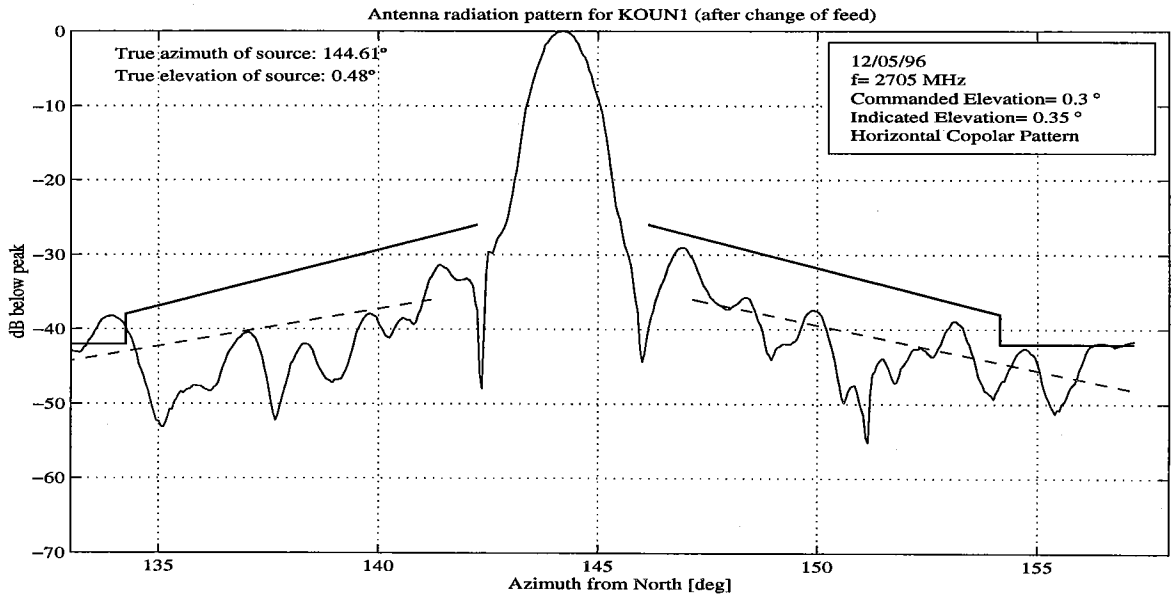

Fig. II.8 (b)The same as in Fig. II.8a, but on a stretched scale for data collected on 12/05/96. This figure should be compared with Fig. II.4b (i.e., the pattern for the research WSR-88D with the single-port feed).

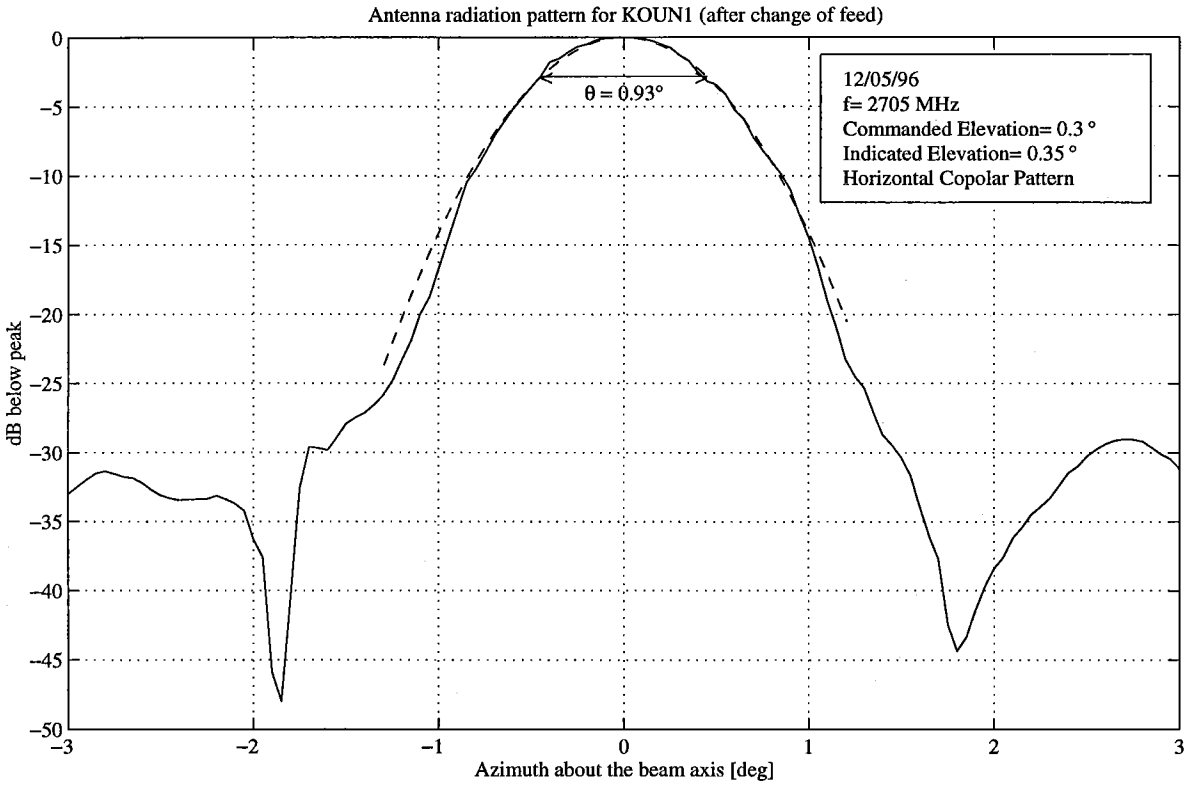

Fig. II.8 (c) Expanded view of the beam pattern after the feed change; this should the compared with Fig. II.4c which is the beam pattern for the single port feed.

Figure II.8c is an expanded view of the beam pattern after the change to a dual port feed; this pattern should be compared with Fig. II.4c, which is the pattern before the feed change. We see that the patterns are nearly identical down to the -20 dB level. The dashed line on Fig. II.8c is the fitted Gaussian function. Comparing the one-way 3 dB beamwidths of the fitted Gaussian functions in these two figures we see they are in reasonable agreement (i.e., 0.93 ° vs. 0.89°). It is also noted that the theoretical expression for the 3 dB beamwidth (II.5) gives a value of 1.04°. This larger theoretical value might be due to the imperfect fit to the actual aperture illumination (Fig. II.6).

Figure II.8d is a contour plot of the copolar radiation pattern for horizontally polarized waves transmitted with the dual port feed installed. This pattern should be compared with Fig. II.4d, which is the same field generated with the single port feed. These patterns are in good agreement. From these comparisons, it can be concluded that the H or front port copolar pattern of the new dual port feed is practically a replica of that for the single port feed of the WSR-88D radars.

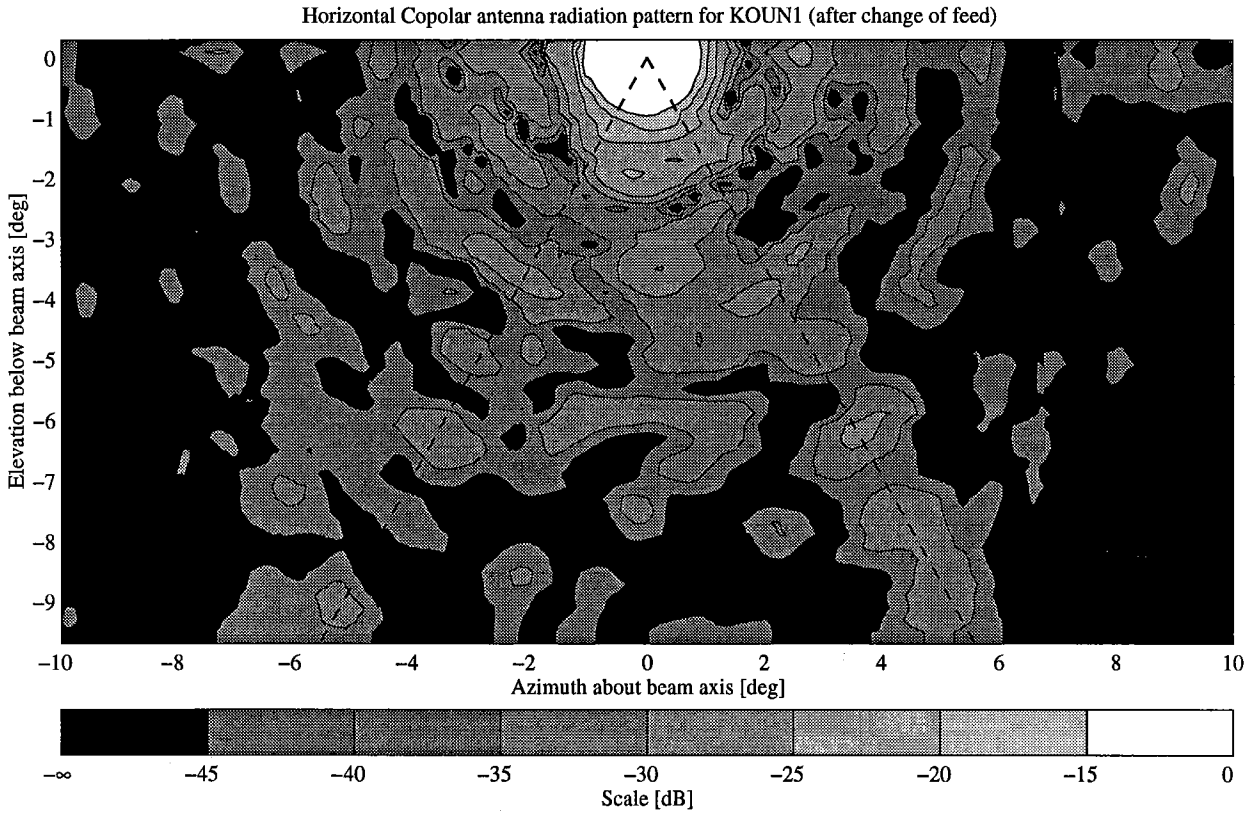

Fig. II.8 (d) A contour plot of the horizontal copolar radiation field.

II.6.2 Cross-polar patterns for the WSR-88D and CSU antennas

Before presenting the cross-polar radiation pattern measurements made with the KOUN1 radar, we first discuss the causes of cross-polar fields and then compare cross-polar pattern measurements for the H port made by the manufacturers of the WSR-88D and CSU antennas. This will establish a baseline for comparisons with measurements made with the KOUN1 antenna.

A parabaloidal reflector, illuminated by a linearly polarized source (e.g., Hertzian dipole, or the TE_{10} mode of a rectangular aperture feed), has in its aperture cross-polarized fields with maxima roughly centered in the sectors between the principal planes (Fradin 1961, Fig. 7.5). These fields alternate in direction from quadrant to quadrant, and thus, based upon symmetry arguments, there should be no cross-polarized (cross-polar) radiation in the principal planes. The radiation pattern of the cross polarized field will be enhanced in regions away from the principal planes.

Because the circular aperture of the single port WSR-88D feed (as well as the new dual port feed) is principally excited with the TE_{11} mode, the radiation field of the feed also has cross-polarized fields in the same sectors as that for the reflector. But the cross-polar electric field vectors associated with the feed are in opposite direction to that which would be present in the reflector's aperture if the feed generated pure linearly polarized waves (e.g., the TE_{10} mode in a rectangular waveguide feed). Thus, the circular waveguide feed eliminates to a substantial degree the cross polarized fields in the aperture (Fradin 1961, p. 399). This cancellation should decrease the amount of cross-polar radiation which is transmitted or received with the KOUN1 antenna.

Before presenting the measurements made on the KOUN1 antenna, we show (Fig. II.9) the cross-polar pattern measurements at the 0° cut for the H port (i.e., vertically polarized waves are transmitted, and the horizontal port, the only port of the WSR-88D feed, is connected to the receiver) made by Andrew Canada on one of the WSR-88D antennas without radome. There are three patterns in this figure. The pattern with peak in the center of this figure is the ±180° pattern, and its dB scale is on the left side; this pattern shows the cross-polar sidelobes over the full 360° of the azimuthal scan. The top pattern on the right side of this figure is a small portion of the copolar main lobe plotted for reference (note this pattern has been shifted downward by 20 dB to accomodate both the copolar and cross-polar patterns on the same plot). The dB scale on the right side of this figure is to be used with the cross-polar pattern on the right side which is plotted on the expanded scale of 5° per major division to show the principal features of the cross-polar lobes near the beam axis.

A comparison of Fig. II.9 with patterns (not shown here) obtained at the 30°, 45°, 60°, and 90° cuts illustrates that the radiation along the principal planes (i.e., the 0° and 90° cuts) is indeed significantly less (i.e., about 10 to 15 dB) than along the other cuts. The most surprising feature of the cross-polar pattern is the presence of a well-defined lobe along the axis of the main beam. Although this lobe is well below the cross-polar levels specified (-27 dB; Paramax Systems Corp. 1992) for the WSR-88D antennas, it is contrary to what is expected for circularly symmetric reflectors. Among the possible explanations for this anomaly are (1) blockage and scatter from the feed and its supporting structure, (2) surface irregularities, and (3) cross-polar radiation from the feed illuminating the reflector.

There is some support for the third explanation. For example, the on axis cross-polar field emitted by the dual port feed is about 33 dB below the copolar peak (Section II.3, Fig. II.6), and the peak of the cross-polar pattern for the antenna (Fig. II.9) is 32 dB below the peak of the copolar signal. Furthermore, the 10 dB widths of the copolar and cross-polar patterns of the antennas agree to within 0.1°. Although the pattern in Fig. II.6 is the primary pattern of radiation from the dual port feed whereas the pattern in Fig. II.9 is the secondary pattern of the reflector illuminated with a single port feed, it is expected that the performance of the dual and

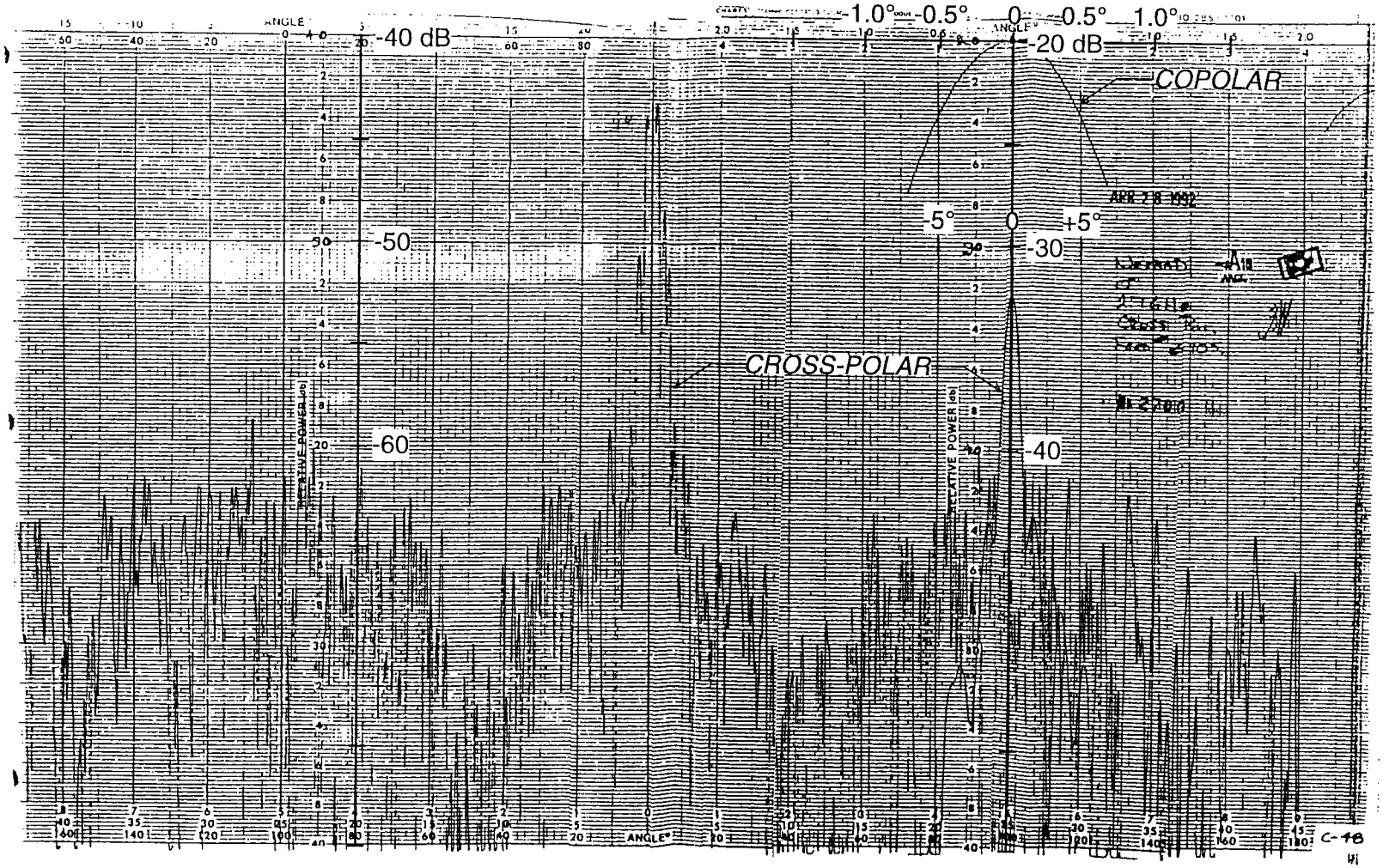

Fig. II.9 The cross-polar radiation patterns for the H port of a WSR-88D antenna without radome measured along the 0° cut on Andrew Canada's antenna range. The pattern with the peak centered on the figure is measured over a ±180° interval, whereas the lower pattern on the right is the cross-polar pattern plotted on the stretched scale as indicated. The short pattern above and to the right is the copolar main lobe plotted for reference on a more stretched scale of 0.5° per major division, but its magnitude has been reduced by 20 dB.

single port feeds are identical, as can be deduced from comparison of copolar patterns before and after the feed change.

In final support of hypothesis (3), we refer to the pattern measurements made on the CSU antenna (Radiation Systems 1993). No pronounced peak in the cross-polar fields was observed in the principal planes of the CSU antenna; Fig. II.10 shows the copolar and cross-polar measurements in the 0° cut of the CSU radiation pattern, and similar results, not shown here, are observed for patterns along the 90° cut. The scale on the left side of Fig. II.10 is for the cross-polar pattern, whereas the scale on the right side is for the copolar pattern. For the experimental measurements made with the CSU antenna, it should be pointed out that the source antenna was rotated about its axis *until a null was observed in the copolar port*, whereas in the experimental procedure used by Andrew Canada, the source antenna was rotated 90° from the position it had for the copolar measurements. The tilt angle (Section II.8, Appendix) to achieve a null was not listed in the 1993 report from Radiation Systems which described the CSU measurements. Ignoring the principal lobe in Fig. II.9 and comparing the other lobes with those in Fig. II.10, we note that the magnitudes of the cross-polar lobes for the WSR-88D and CSU antennas are of comparable value. Thus, the cross-polar radiation patterns of the two antennas (i.e., CSU and the WSR-88D antennas) might be in better agreement than deduced by simply focusing on the absence or presence of a main lobe in the cross-polar pattern; that is, the cross-polar pattern of the CSU antenna could possibly also have a pronounced peak on the axis.

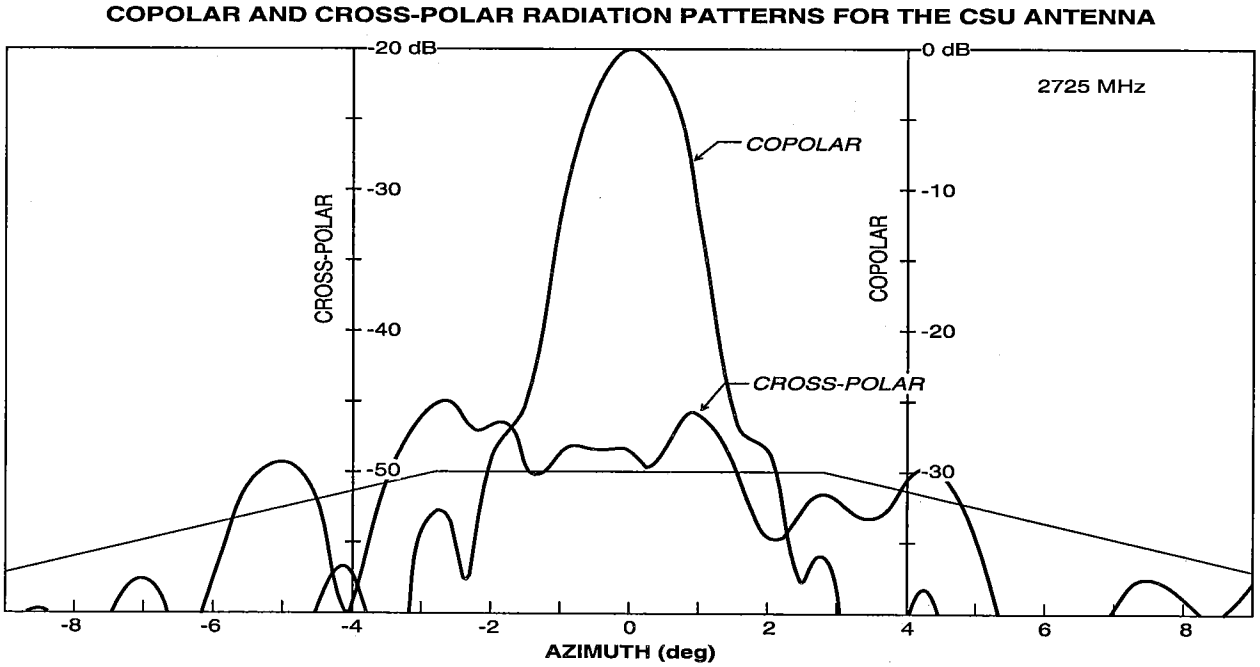

Fig. II.10 The CSU antenna's copolar and cross-polar radiation along the 0° cut for the H port (adapted from the report "Electrical acceptance test procedure CSU antenna", Nov. 12, 1993). The left dB scale is to be used with the cross-polar pattern, whereas the right dB scale is to be used with the copolar pattern.

This favorable agreement between the cross-polar radiation patterns for the CSU and WSR-88D antennas does not hold, however, for radiation patterns measured outside the principal planes. For example, comparing the CSU and WSR-88D cross-polar patterns (not shown here) at the 45° cut, we find that the CSU antenna's cross-polar levels hover around the -38 dB level out to ±9°, whereas the cross-polar levels of the WSR-88D antenna fall well below the -50 dB level and remain for the most part below -50 dB for the full ±180° azimuthal scan. Unfortunately, the CSU data do not extend beyond ±9°, so we are unable to make comparisons of levels far removed from the main lobe. In most cases, it is the lobes nearest the main lobe that are annoying when observing scatter from precipitation.

II.6.3 H-port cross-polar measurements made on KOUN1

The front or H-port cross-polar patterns were measured by transmitting vertically polarized waves from the standard-gain horn atop the Energy Center. The rectangular aperture of the standard-gain horn was leveled to insure that only vertically polarized radiation is transmitted. It was noticed, during the preliminary cross-polar measurements made in December 1996, that to obtain an on-axis null in the signal received at KOUN1, the standard-gain horn had to be tilted (less than a few degrees) suggesting that (1) the dual port KOUN1 feed is not level (i.e., the feed is tilted about its axis), (2) the front port, which should receive/transmit only horizontally polarized waves, is also receiving/transmitting vertically polarized waves (i.e., there is cross-polar coupling in the feed), or (3) scatter from the terrain generates cross-polar signals which would tilt the observed polarization ellipse; scattered cross-polar signals 35 dB below the already weak (35 dB below the copolar peak radiation) cross-polar radiation can tilt the polarization ellipse by 1° . For the latter reason, we made tilt measurements on a nearby tower which provided a much higher elevation angle to the boresight and, thus, less scatter from the terrain; the tilt measurements are reported in Section II.6.4.

With the standard gain horn leveled, first the copolar signal was maximized (i.e., the KOUN1 antenna was pointed at the standard gain horn transmitting horizontally polarized waves). A copolar radiation pattern was measured to establish a reference level for the cross-polar patterns, and the horn was rotated precisely 90° about the line-of-sight by leveling the orthogonal side of the rectangular horn. Then, cross-polar pattern measurements versus azimuth were made at 0.1° elevation angle increments from -0.5° to +3° , and in increments of 0.2° for the elevation range above 3°.

As with the Andrew Canada cross-polar pattern measurements, we also found a significant peak of cross-polar radiation along the axis of the reflector (Fig. II.11a). Comparing the cross-polar patterns measured for the KOUN1 antenna with those measured by Andrew Canada for the WSR-88D antennas without radome (Fig. II.9), we see reasonable agreement. The on-axis peak in Andrew Canada's measurement is about 33 dB below the copolar peak, whereas for the KOUN1 measurements, the cross-polar peak is about 36 dB below the copolar peak. The cross-polar sidelobes near the main lobe are between 40 and 50 dB below the copolar

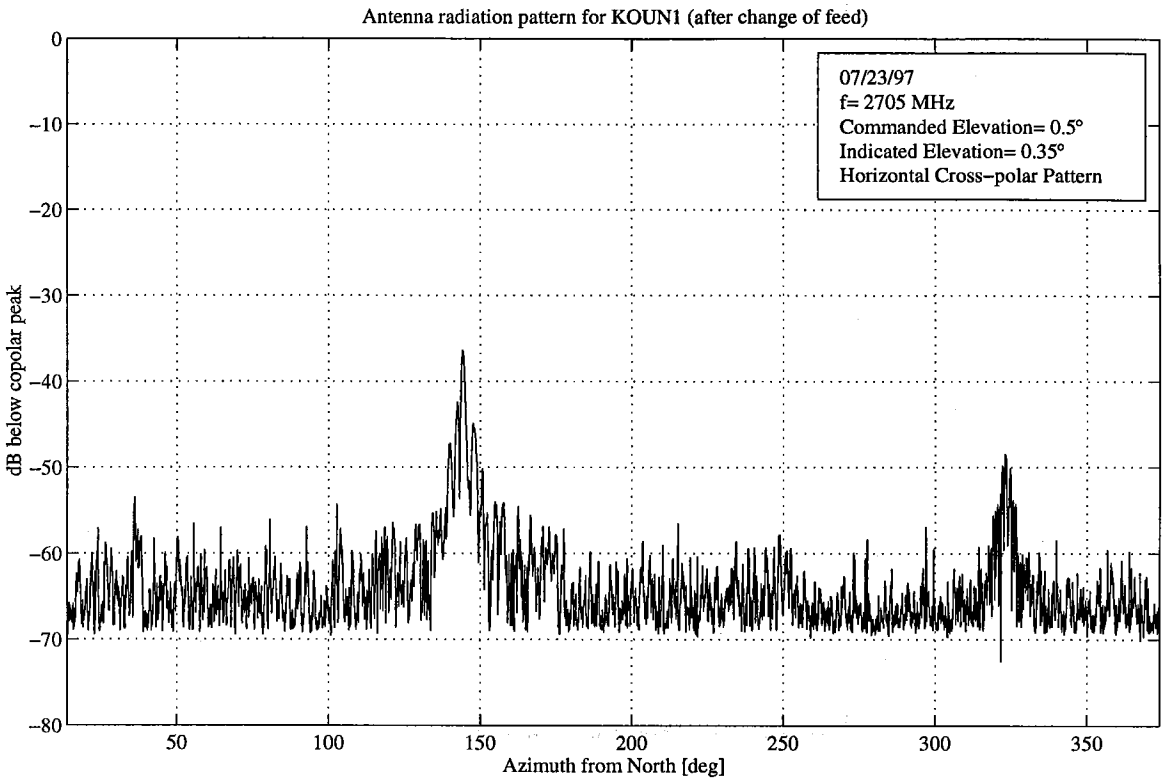

Fig. II.11 The cross-polar patterns for the H port measured on the KOUN1 antenna after the dual port feed was installed. The standard-gain horn is leveled to transmit vertically polarized fields, and the KOUN1 receives horizontally polarized fields (i.e., the front port is connected to the receiver). (a) the pattern on a ±180° scale.

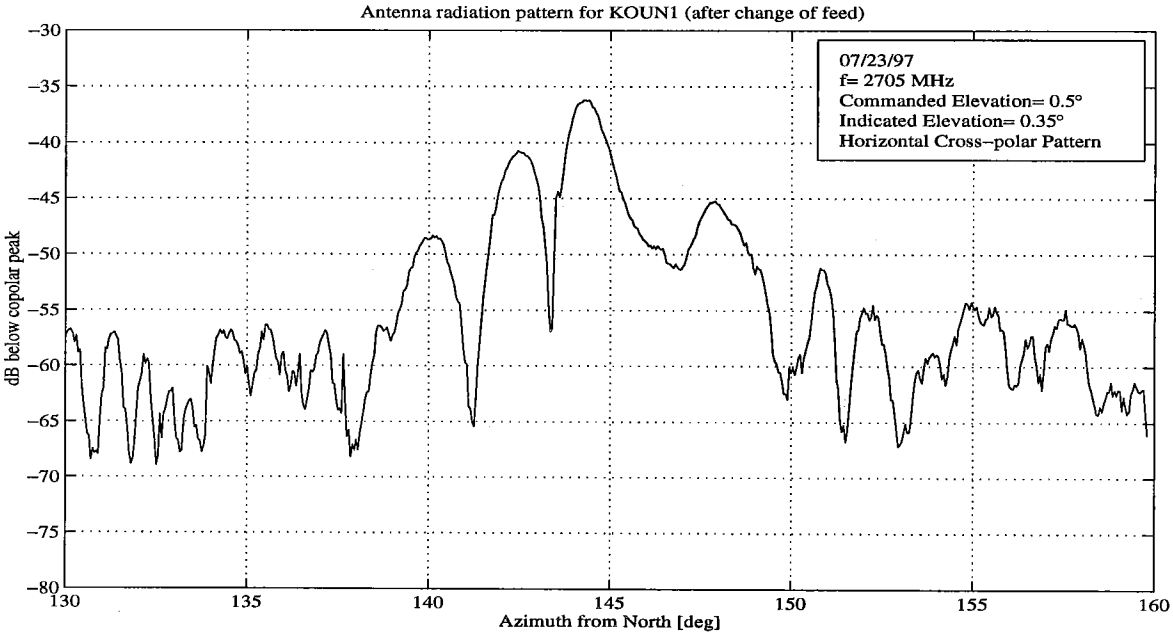

Fig. II.11. (b) The pattern on a stretched scale.

peak in both measurements, and the sidelobes far removed from the main peak average about 65 dB for both measurements.

As pointed out earlier (Section II.3), evidence suggests the on-axis peaks of cross-polar radiation in the WSR-88D and KOUN1 pattern measurements are due to on-axis peak of cross-polar radiation emitted by the feed. Support for this contention is that the peak of cross-polar radiation occurs exactly at the same azimuth (i.e., 144.2°; Fig. II.11b) as does the copolar peak, and that the peak of cross-polar radiation is about 36 dB below the copolar peak, as seen in Fig. II.11b; this compares favorably with the peak level (34 dB) in the feed's cross-polar radiation reported in Fig. II.6. As mentioned in Section II.6.2, there are several possibilities for the source of cross-polar radiation along the axis of the beam where, ideally, there should be no radiation.

Fig. II.11c is a contour plot of the cross-polar radiation field radiated by the front (H) port. The most striking features of this plot are the ridges of prominent sidelobes along the lines perpendicular to the feed support spars in the lower half of the reflector (Fig. II.1a), whereas there is no prominent line of sidelobes along the 0° cut (i.e., perpendicular to the vertical spar in

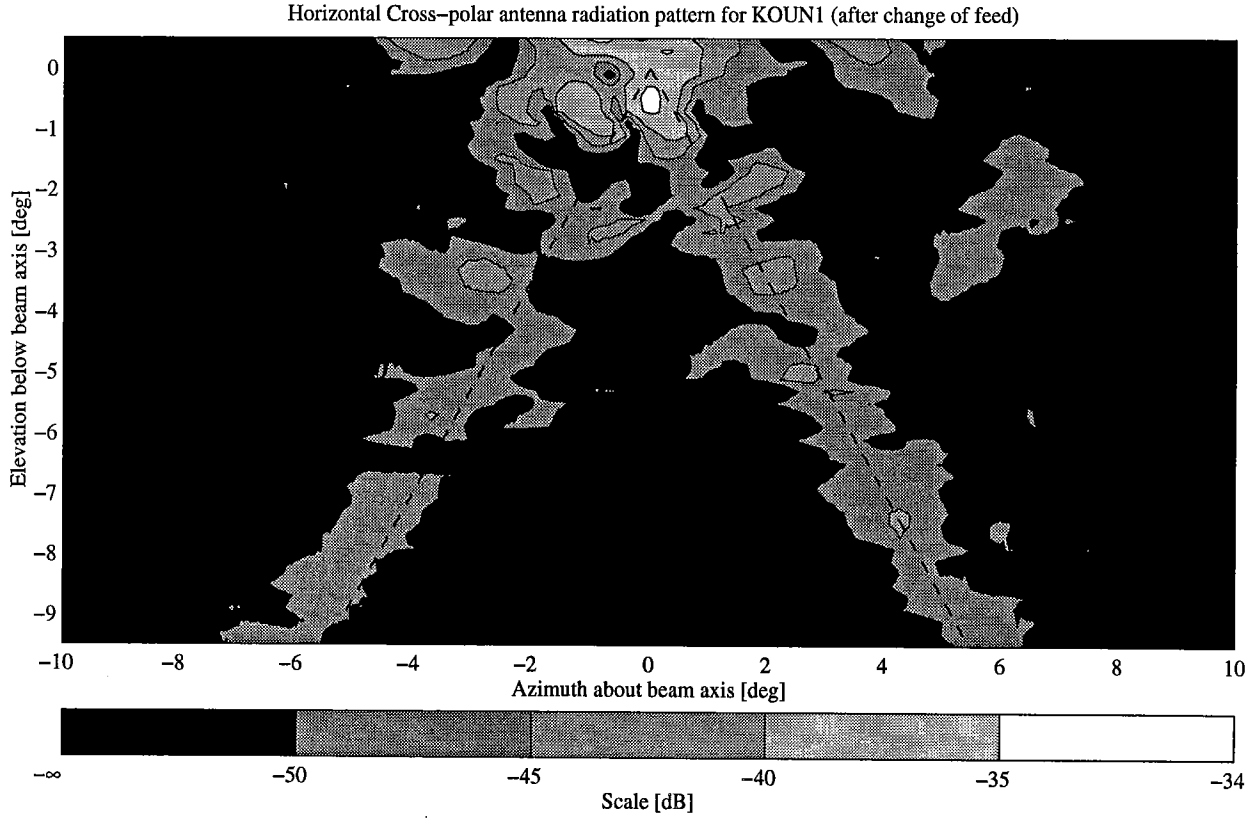

Fig. II.11 (c) A contour plot of the cross-polar reception at the H port.

the upper half of the reflector). The vertical spar does not couple as much energy from the copolar field to the cross-polar field because the horizontally polarized copolar field is perpendicular to the vertical spar, whereas it is oblique to the spars in the lower half of the reflector. It is also noted that there is very little cross-polar signal outside these ridges as expected and explained in Section II.6.2.

The starting gray scale in Fig. II.11c is the peak level of the cross-polar signal. Thus, we see that the peak cross-polar signal is -34 dB, and the peak is located about 0.5^0 below the beam axis. The -34 dB level corresponds, however, closely to the on-axis cross-polar signal of the feed (Fig. II.6). This adds confidence in the interpretation that the peak of cross-polar radiation is due to the cross-polar radiation emanating from the feed.

We also conducted cross-polar pattern measurements on the KOUN1 antenna with the dual port feed after achieving a null by rotating the source horn about its axis (although the tilt was not measured it appeared to be less than a couple of degrees) and found, as in the CSU measurements, a cross-polar pattern without a well pronounced peak. The elimination of the cross-polar peak by tilting the standard gain horn to produce an on-axis null was quite evident in the vertical cross-polar pattern; the peak decreased from -32 dB (see Fig. II.13b; Section II.6.6) to -40 dB, but the first sidelobe increased a few dB to about -40 dB. The decrease in the horizontal cross-polar peak was one or two dB.

Cross-polar measurements are more difficult to interpret and to compare with theoretical calculations because of scatter from the terrain surrounding the radar site and because cross-polar signal levels are typically less than -30 dB below the copolar signal. Furthermore, the cross-polar signal could be copolar radiation converted to cross-polar radiation upon scatter from the terrain. At an elevation angle of 0.45°, the first null of the pattern is directed at the specular point which is computed to be about 1636 m from KOUN1. Thus, at this elevation angle, the main lobe illuminates ground with increasing intensity from this null point to the Energy Center, where the terrain is most strongly illuminated. (The inverse square loss due to increase in range is about 6 dB, but the increase in radiation due to the increase of illumination for rays closer to the beam axis is more than 30 dB; Fig. II.8c.) The angle between the main lobe axis and the terrain near the Energy Center is about 0.9°, and from the radiation pattern in Fig. II.8c, it is determined that this terrain is illuminated with an intensity about 13 dB below the main peak (or, for reception, the KOUN1 antenna has a reception sensitivity to signals scattered from the terrain near the source of about 13 dB below that if the beam axis was pointed directly at the ground). Trees and other scattering objects depolarize copolar radiation so that some of the incident copolar radiation is converted to scattered cross-polar radiation.

Measurements (e.g., Long 1975, Fig. 7-6) suggest that the coupling between cross-polar and copolar fields for scatter from trees is typically larger than -10 dB, and some data show the cross-polar scattered field to be larger than the scattered copolar field. Furthermore, if vegetation is dense and covers the ground, as is the case here, the effective reflection coefficient for scattering is of the order of 0.1 (i.e., -20 dB in power), regardless of the polarization (Beckmann

and Spizzichino 1963, p. 339). Accepting these rough estimates of scattering levels, it is expected that the scattered copolar signal level could be as large as about 33 dB below the signal received directly along the boresight (20 dB is accounted for by the reflection coefficient and 13 dB by the reduced illumination of the terrain for a beam elevated 0.9° above the ground), and that the cross-polar signal might be at most 10 dB less than this. In conclusion, it is anticipated that copolar signals at levels less than 33 dB below the main lobe peak could be suspected of error due to terrain interference, whereas the cross-polar signals a few dB below this level could be in error. Thus, it is not surprising that cross-polar sidelobes near the main lobe exceed by few dB those measured by Andrew Canada, as can be seen by comparing Figs. II.4b and II.2b. Furthermore, as pointed out in Section II.1.2.4, the few copolar sidelobes that exceed the specified limits sketched in Fig. II.4b also could easily have been caused by terrain scatter.

II.6.4 Copolar measurements for the back (V) port

Fig. II.12a gives the vertical copolar radiation pattern of the KOUN1 antenna. In this case, the transmitting source atop the Energy Center is leveled to transmit pure vertically polarized waves, and the back port (i.e., for vertically polarized waves) of the dual port feed is connected to the receiver to allow copolar pattern measurement. Comparing the vertical copolar pattern with

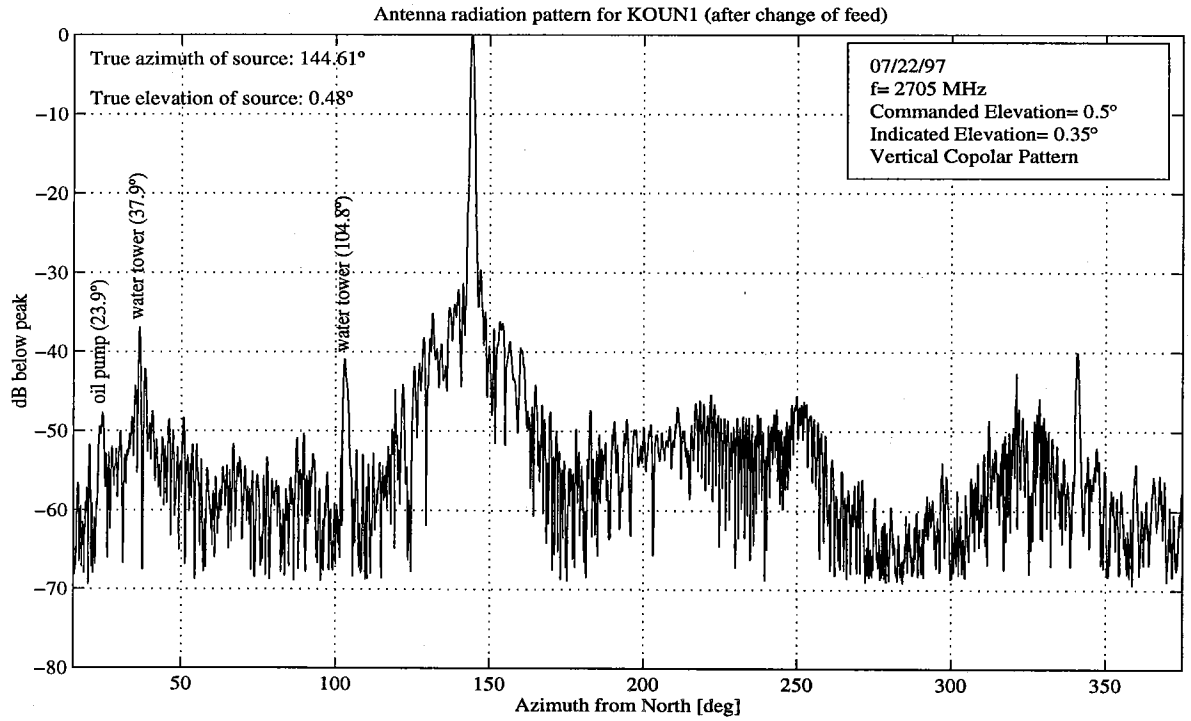

Fig. II.12 The copolar radiation pattern for reception of vertically polarized waves at the back port. Measurements are made at 2705 MHZ, and patterns are from azimuthal scans at a commanded elevation angle of 0.3°. (The boresight or beam axis is at a commanded elevation angle of about 0.28°.) (a) The pattern over a 360° azimuthal scan.

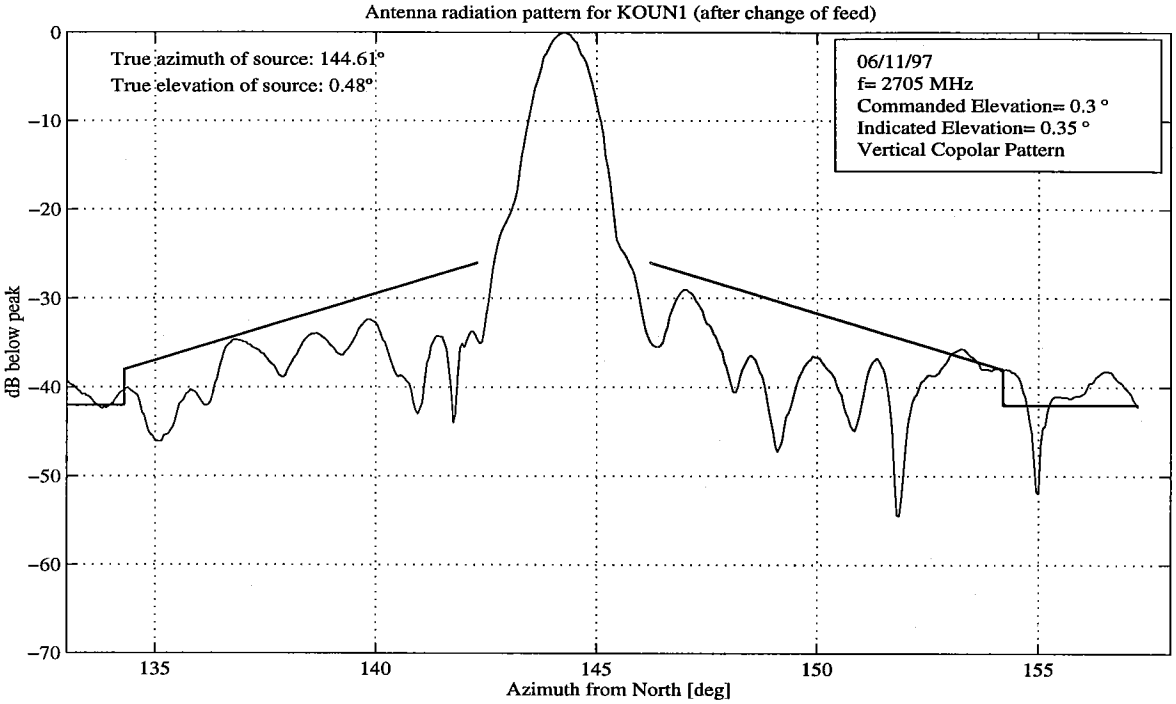

Fig. II.12 (b) The pattern over a ±13° azimuthal interval about the beam axis. The solid lines are the specified limits of sidelobe levels for the antenna in a radome.

the horizontal copolar pattern presented in Fig. II.8a, we see strong similarities. The sidelobe levels, for the most part, are higher for the vertical copolar radiation. The higher sidelobe levels for vertically polarized waves might be due to the larger scatter from the terrain; vegetation has growth which is principally vertically oriented.

To facilitate comparison in the important region about the main lobe, we plot in Fig. II.12b the same data on an expanded azimuthal scale. This plot should be compared with that for horizontally polarized waves (Fig. II.8b). Although the sidelobes for the vertically polarized waves are overall a few dB higher in some places, the sidelobes do not exceed the limits specified except for a small departure about the 155° azimuth mark.

Fig. II.12c depicts an expanded view of the principal lobe of V copolar radiation, and comparing this with the main lobe for horizontally polarized waves (Fig. II.8c), we see good agreement down to the -15 to -20 dB levels. (A more comprehensive comparison is presented in Section II.6.7.) Also shown in Fig. II.12c is the Gaussian function fitted to the data from which we calculated 0.90° for the one-way 3 dB beamwidth. This beamwidth for vertically polarized waves is close to the 0.93° beamwidth for horizontally polarized waves (Fig. II.8c).

A contour plot of the V copolar pattern is in Fig. II.12d. This should be compared with the H copolar pattern (Fig. II.8d). It reinforces our early remark that the two patterns compare

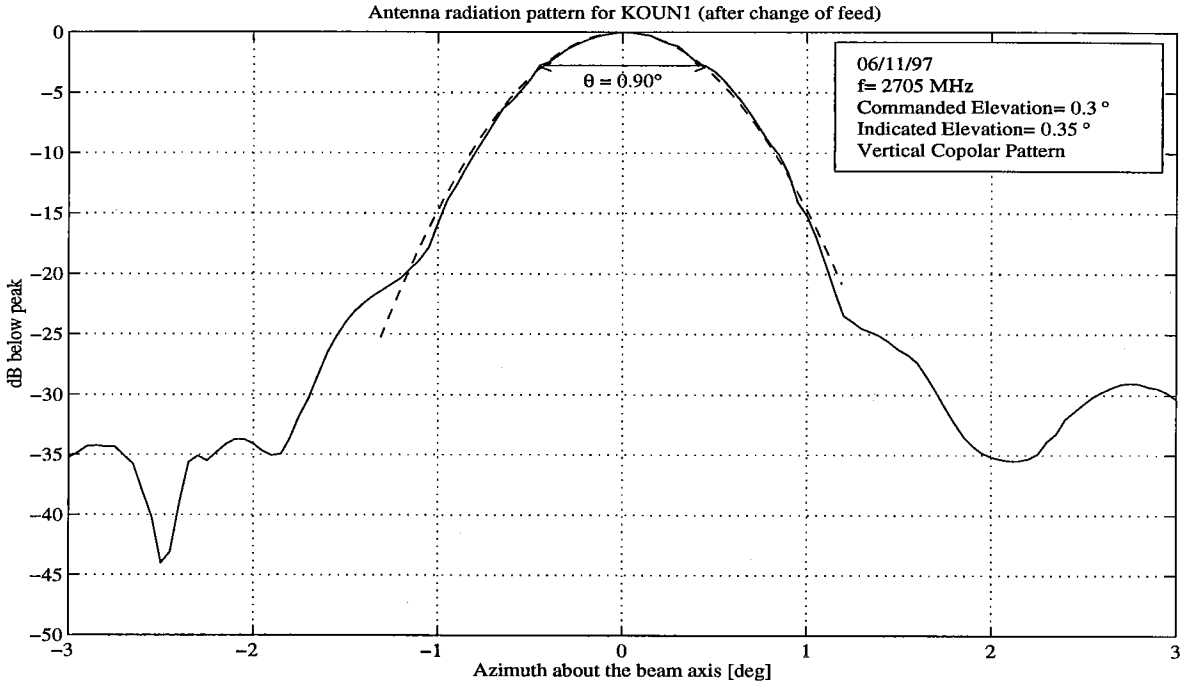

Fig. II.12 (c) An expanded view of the main lobe or beam with a scale centered about the boresight.

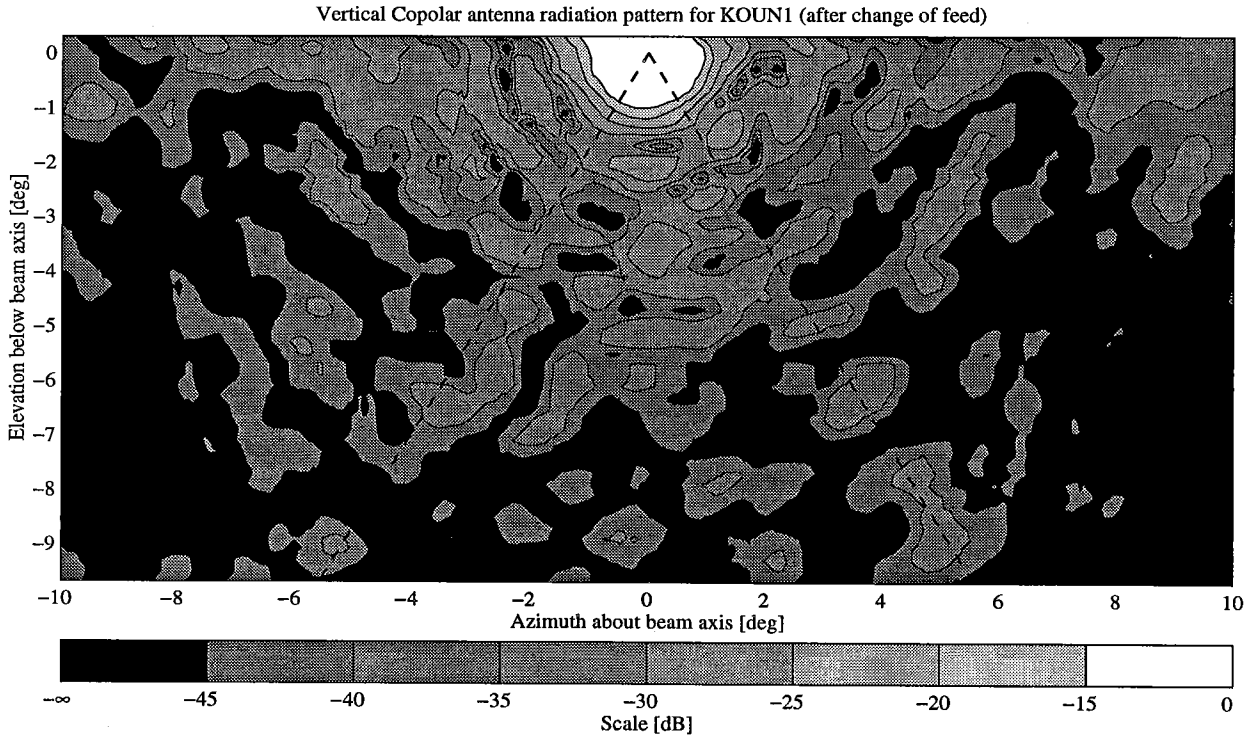

Fig. II.12 (d) The copolar radiation pattern for reception of vertically polarized waves. Contour intervals are 5 dB starting at -15 dB and ending at -45 dB below the peak. The dashed lines are where the sidelobes are expected to be enhanced due to spar blockage.

well, but the sidelobes for vertically polarized waves are somewhat higher in many places. Comparisons of the two patterns are discussed in more detail in Section II.6.6.

II.6.5 V-port cross-polar measurements made on KOUN1

In Fig. II.13a, b, we plot the cross-polar radiation pattern for the backport (V). Comparisons with the horizontal cross-polar radiation (Figs. II.13a,b) show remarkable similarity, although the vertical cross-polar signals appear to be a few dB higher in a few places. Perhaps this is an artifact of the antenna range in which there is a larger conversion of the horizontally polarized radiation transmitted from the standard gain horn to vertically polarized radiation upon scatter from the vegetation than the vice versa conversion. Alternatively, these differences may be due to the differences in the cross-polar radiation characteristics of the dual port feed and/or reflector and its supporting structures

. Fig. II.13c shows a contour plot of the backport (V) cross-polar radiation; it should be compared with Fig. II.11c, which is a contour plot of the frontport (H) cross-polar radiation. As already pointed out, the near sidelobes of the backport cross-polar radiation appear to be higher, but the far out sidelobes are somewhat lower.

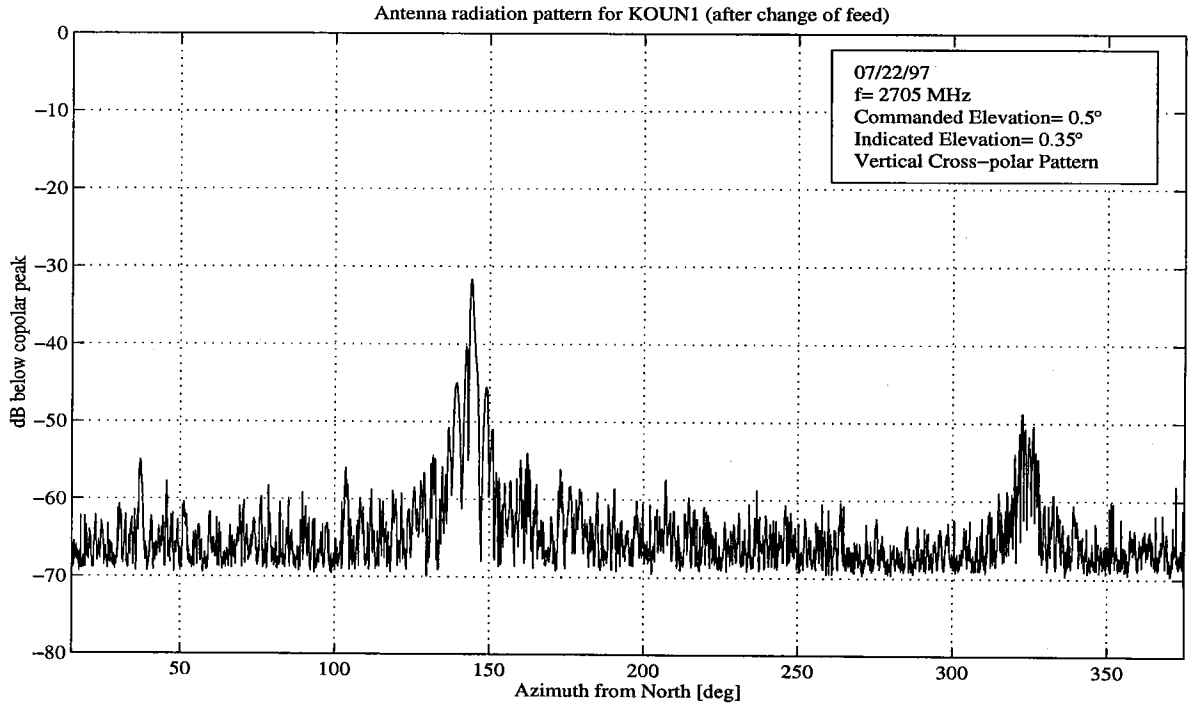

Fig. II.13 The cross-polar patterns for the V port measured on the KOUN1 antenna after the dual port feed was installed. The standard-gain horn was leveled to transmit horizontally polarized fields, and the KOUN1 received vertically polarized fields (i.e., back port was connected to the receiver). (a) The pattern on a ±180° scale.

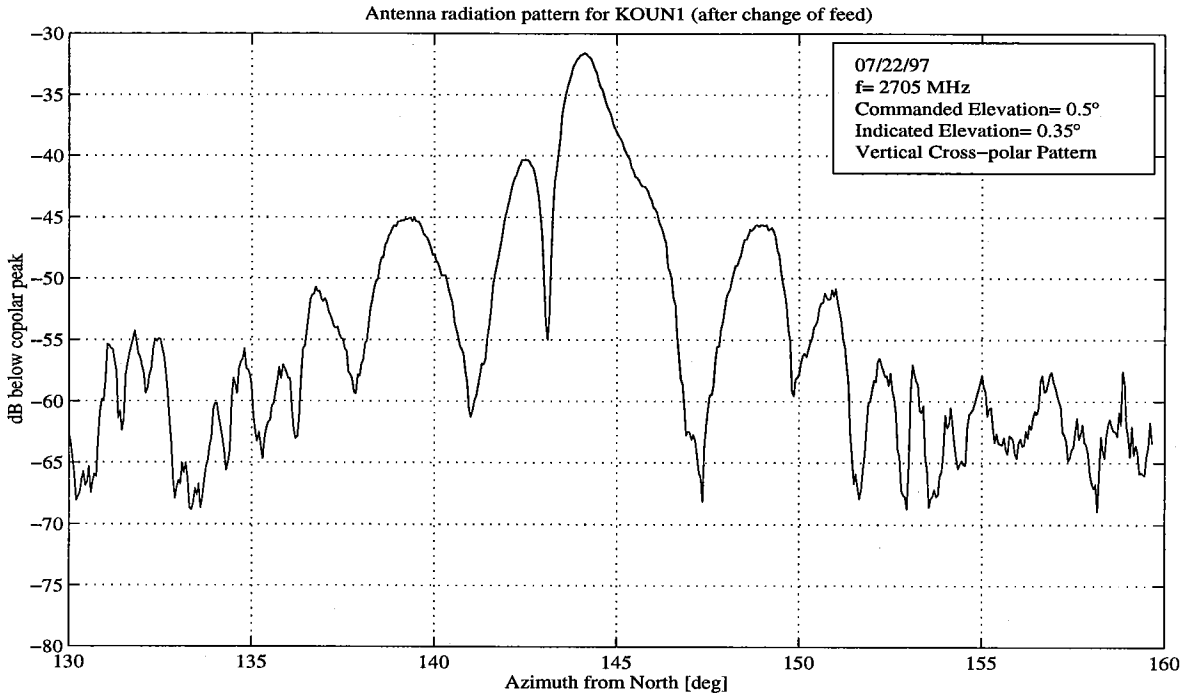

Fig. II.13 (b) The pattern on a stretched scale.

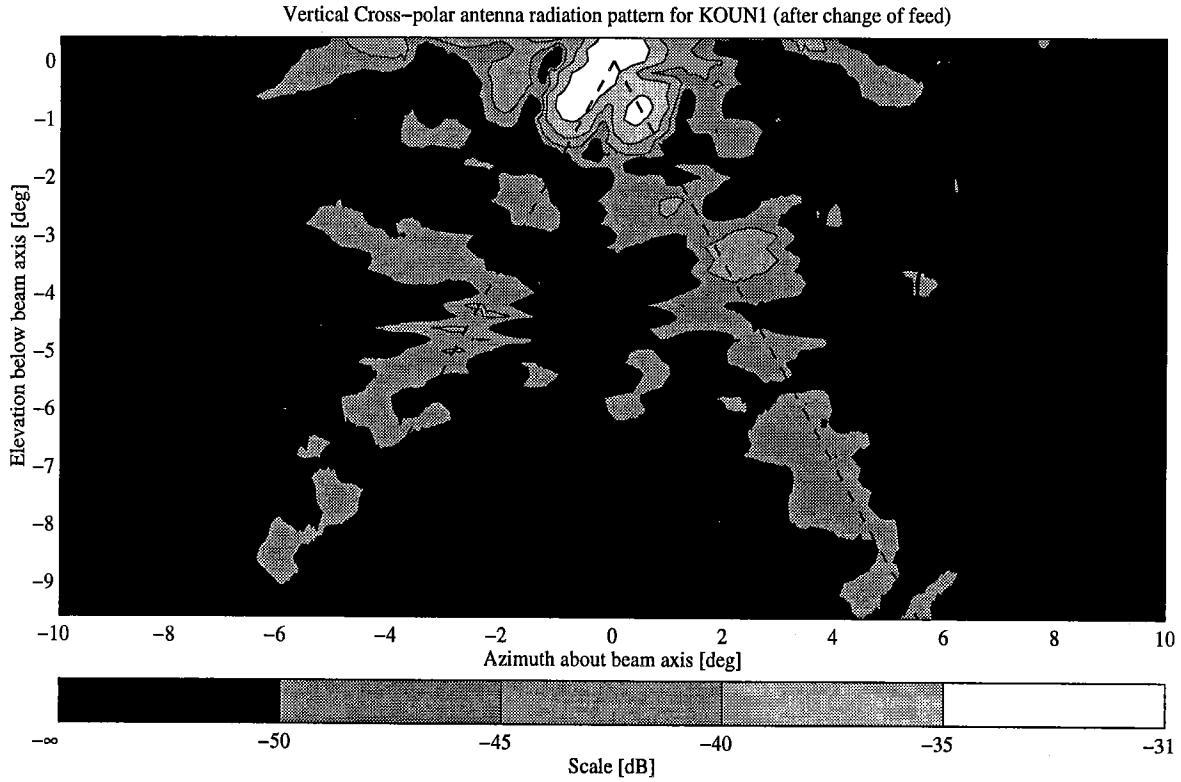

Fig. II.13 (c) A contour plot of the cross-polar reception at the V port.

II.6.6 Comparisons of H and V patterns

To place the comparisons of H, V patterns on a more quantitative footing, we present them together in Fig. II.14a (the H and V patterns vs. azimuth angle through the boresight) and in Fig. II.14b (the H and V patterns vs. elevation angle, also through the boresight). As can be seen from these two figures, the patterns agree for the most part to a fraction of a dB down to the -20 dB level. Bear in mind that some of the differences could be due to measurement noise discussed in Section II.1.2.3. Also note that the first few sidelobes along the elevation scan (Fig. II.14b) agree better than along the azimuth scan. This is attributed to the fact that the main lobe in the elevation scan is directed well above the scatterers on the ground, whereas for the azimuth scan, the lower edge of the main lobe illuminates ground scatterers. Thus, sidelobes in the azimuth scan are more likely subjected to interference from scatter of the main lobe from ground objects rather than the bottom half of sidelobes seen in the elevation scan.

These comments suggest that the patterns might be better matched than that indicated by the plots. To minimize the influence of noise in the comparison of H, V patterns, it is better to compare the fitted Gaussian functions (Figs. II.8c and II.12c). The 3 dB beamwidths of the fitted Gaussian functions agree to within 0.03°, which is likely within the measurement tolerance; this beamwidth difference corresponds to about a 0.1 dB difference at the 3 dB points of the antenna pattern. Differences between the data and the fitted Gaussian functions are as much as 0.4 dB in the range of normalized gains from 0 to -10 dB, and most likely, these differences are errors in measurement and are not representative of the true fluctuations of the gain. Much more precise antenna pattern measurements on a well designed antenna range are needed to better quantify the differences in the H and V patterns.

$$10\log_{10}\left|\frac{P_v(\theta,\phi)}{P_v\text{max}} - \frac{P_h(\theta,\phi)}{P_h\text{max}}\right|,$$

To obtain an indication of the difference in patterns for the entire region about the beam axis, we have plotted in Fig. II.14c the difference contours obtained from the equation where the vertical line denotes magnitude. Since data for the H and V patterns were obtained several months apart, one pattern was shifted by about 0.05° in azimuth (no shifts in elevation were required) to obtain the best match by eye. The gray scaling is made relative to the peak difference, which in this case is -5 dB. But, as can be seen from the figure, the differences over most of the main lobe (i.e., within about 1.5° from the beam axis) is well below -10 dB. Furthermore, the larger differences occur in the upper part of the main lobe (i.e., above 0°), and it is suspected that these larger differences could be due to the scatter from the main lobe, because it more strongly illuminates ground scatterers when the upper part of the main lobe is scanned. This latter observation points to the limitation of the KOUN1's mock antenna range.

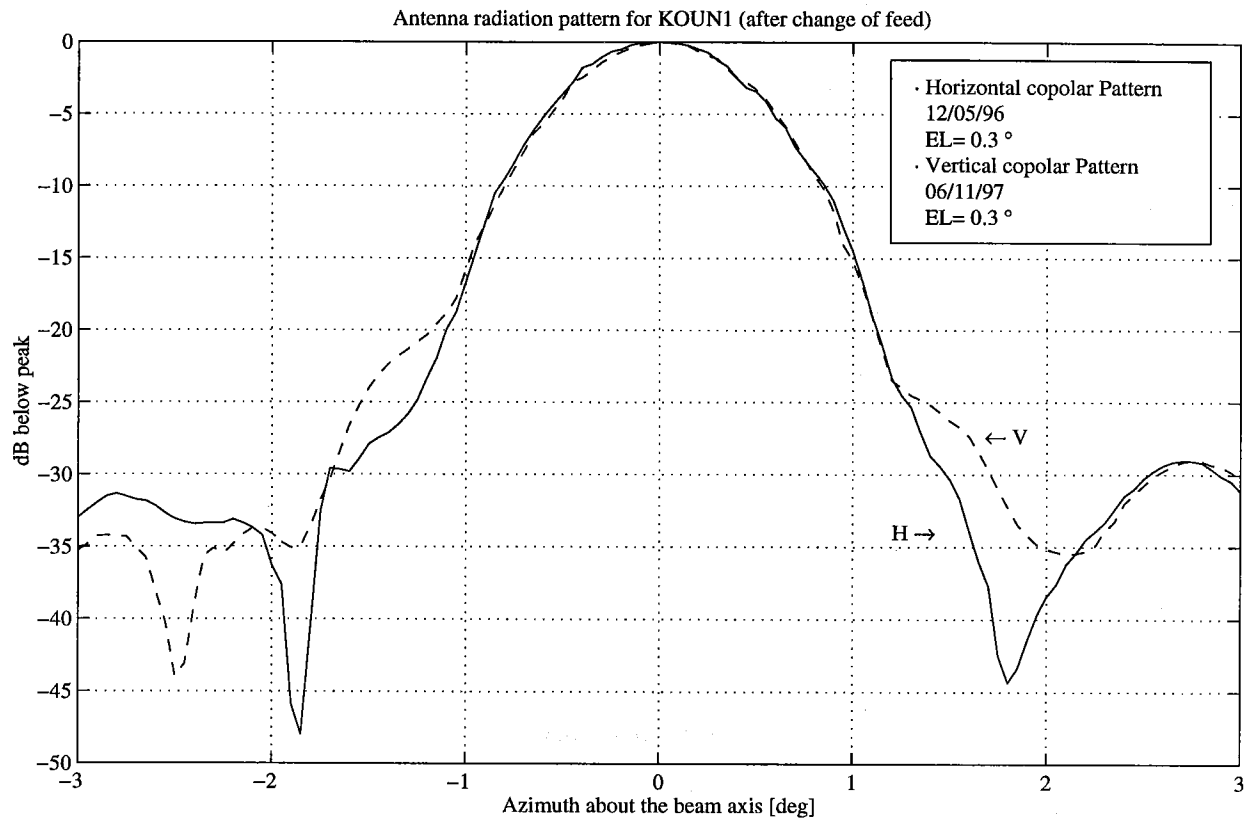

Fig. II.14 (a) A comparison of the copolar main lobe patterns for H and V radiation as a function of azimuth through the boresight.

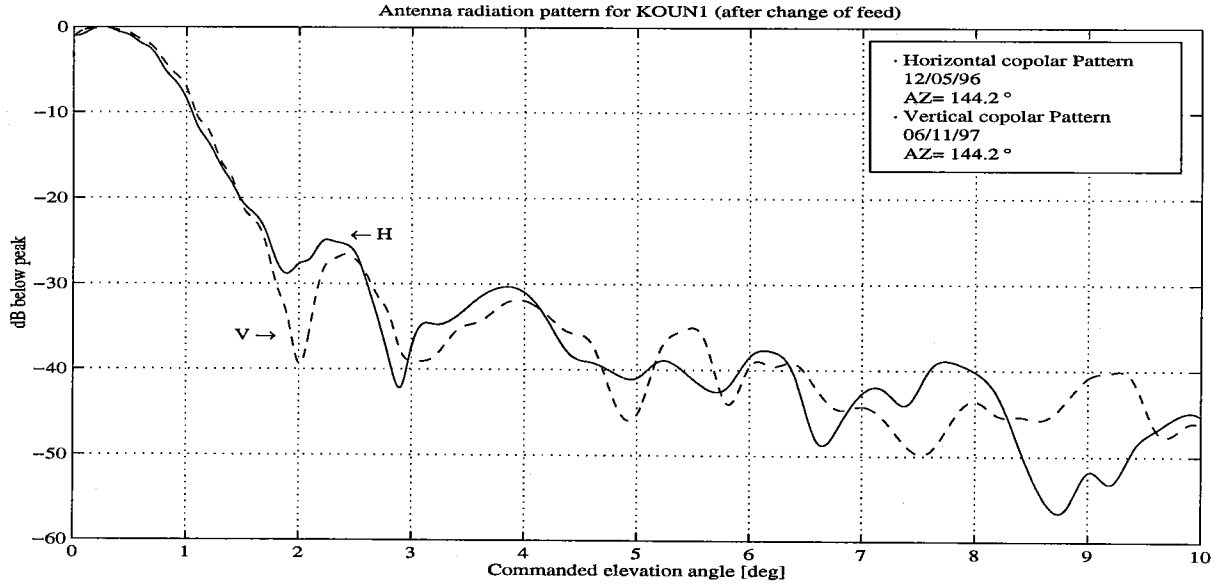

Fig. II.14 (b) The same as (a), except the scan is along the elevation direction.

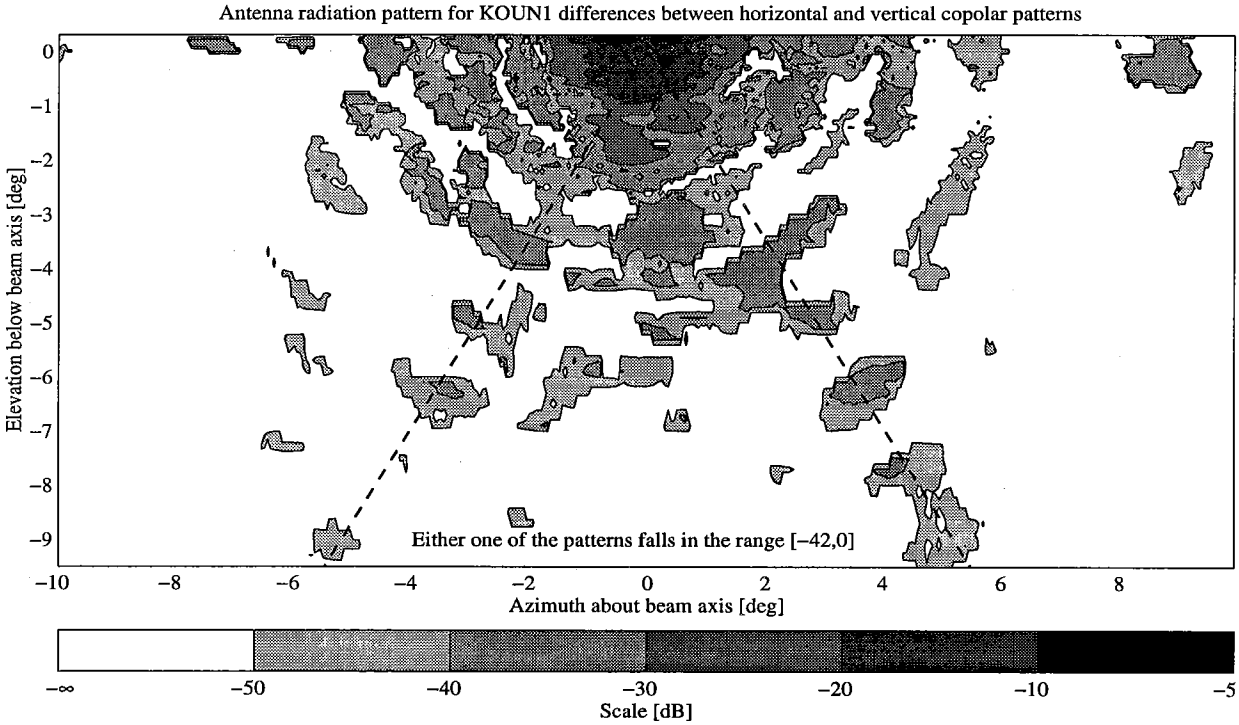

Fig. II.14 (c) A contour map of the difference in the V and H copolar pattern powers. Differences are plotted only if both patterns have relative gain values in the range -42 to 0 dB.

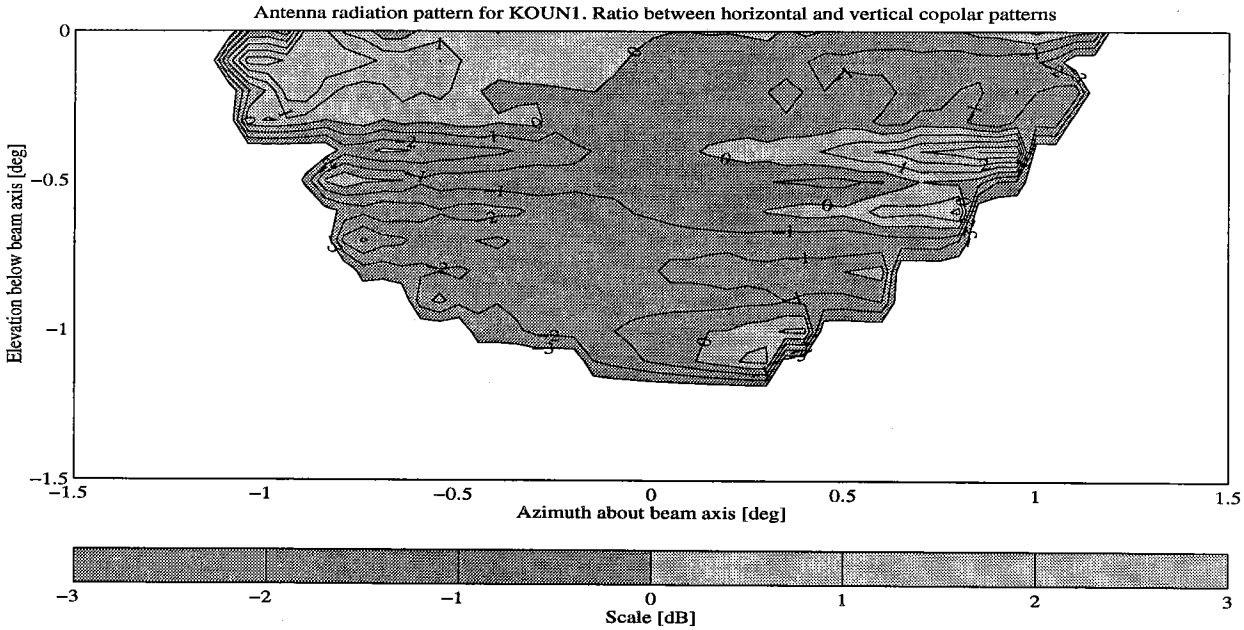

Fig. II.14 (d) An expanded view of the differences in V, H patterns about the main lobe; if the H pattern is larger, the difference is labeled with a positive dB gray scale code.

Plotted in Fig. II.14d are contours of the ratio P_h/P_v (in dB) about the beam axis (i.e., for points below the boresight and having antenna gain > -20dB). This plot shows that, for the most part, the patterns agree within ±1 dB, and that the agreement is best where the gain is largest (i.e., near the beam axis). For points far removed from the axis, the difference is larger, as expected. But, because the antenna gain is much smaller in these regions, the larger dB values are not as significant as points closer to the axis.

II.6.7 Measurements of the tilt of the polarization ellipse

Cross-polar radiation combines with copolar radiation to form, in general, elliptically polarized fields (Section II.8, Appendix). The tilt of the major axis of the polarization ellipse is a function of the relative strengths of the two orthogonal components (i.e., the horizontally and vertically directed electric fields) and the relative phase between the two. If the relative phase is 0 or 180^0, the resultant field will be linearly polarized with a tilt angle

$$\tau = \tan^{-1}\left(\frac{A_V}{A_H}\right), \tag{II.7}$$

where τ is measured ccw from the horizontal and is the angle between the direction of the electric field of the linearly polarized wave and the horizontal, and A_V, A_H are the amplitudes of the vertical and horizontal components of the electric field vector (Fig. II.A.1). τ is positive ccw from the horizontal if both A_V and A_H are in phase, and negative, or cw, from the horizontal if they are out of phase.

If the phase difference β between the vertically and horizontally polarized fields is not 0 or 180^o, the field will be elliptically polarized, and the polarization ellipse will have a tilt angle given by

$$\tau = \frac{A_V}{A_H}\cos\beta \ (radians). \tag{II.8}$$

Eq.(II.8) is derived in the Appendix (i.e., Section 2.8); we have used the simpler approximate form because cross-polar field A_V is much weaker than copolar field A_H (for the front or H port). If the wave is principally vertically polarized (i.e., the back port is connected to the receiver), then A_V and A_H need to be interchanged in (II.8), $A_V >> A_H$, and τ is the tilt angle measured ccw from the vertical.

If the the cross-polar wave is produced by an angular rotation α of the feed about its axis, a feed which otherwise generates pure H or V waves, the phase β will be 0^o, and $\tau = \alpha$. Thus, a

measurement of τ would give the rotation of the feed. On the other hand, if the cross-polar wave is generated by imperfections in the feed, β could have any value, and the wave would be, in general, elliptically polarized, and $\tau \neq \alpha$. A measured tilt angle of zero does not necessarily mean that the wave is linearly polarized. For example, if $\beta = \pm\pi/2$, (II.8) shows that $\tau = 0$, even though there might be significant cross-polar signal. But we can still correct, if necessary, for any tilt of the polarization ellipse by rotating the feed. Although this will not produce a linearly polarized wave, a correct rotation will minimize the cross-polar wave.

Because a peak in cross-polar radiation was observed along the boresight (Fig. II.11a), there was concern that the peak might be related to the fact that the feed is incorrectly oriented about its axis and, thus, not transmitting or receiving pure horizontally (or vertically) polarized waves (e.g., the front port, normally receiving only H waves, is receiving some portion of a vertically polarized wave). In order to have confidence that the cross-polar signal is generated by the feed and not by cross-polar coupling due to terrain scatter, we made the tilt measurements atop the KCRI tower (Fig. II.3). This places the radiation source in the near field of the antenna where the KOUN1 beam is still collimated (i.e., at a 300 m distance, the beam is essentially cylindrical in shape). Considering the height of the towers (i.e., 20 and 30 meters), the angle to the terrain is several degrees below the beam axis (compared to about 1° when the radiation source was atop the Energy Center); thus, the scatter from the terrain should be significantly reduced.

The KOUN1 antenna was boresighted on the copolar signal from a leveled standard gain horn atop the KCRI tower. The standard-gain horn was mounted onto a precision jig [8] which had a rotational accuracy of about ±0.1°. The standard gain horn was rotated about its axis until a minimum was established. The amount of rotation to establish the minimum was noted. With the front port (H) connected to the receiver, the measured tilt τ is zero degrees within the accuracy of measurement (i.e., about ±0.1°). With the rear port (V) connected, the tilt is also about zero degrees within the measurement accuracy. The cross-polar measurements suggest that the feed generates, along the boresight, cross-polar signals at levels about 34 dB below the copolar peak, and that the rotational postion of the feed is correct to within 0.1° to 0.2°

II.7. Errors in measurement of polarimetric variables due to pattern mismatch

Ideally, H and V patterns should be perfectly matched, and cross-polar coupling should be negligible. Some of the mismatch, in peak gain for example, could be due to differences in the signal levels at the ports of the feed or differences in the gain of the respective receivers (if two independent receivers are used), and not necessarily mismatch in the feed itself or in differences in response of the reflector to H and V illuminations. Thus, calibration of the H, V receivers must be made in any case, even if the patterns are perfectly matched. Calibration of H, V channels using, for example, backscattered data along vertical beam in stratiform rain would hide any

[8] This component was obtained, courtesy of Mr. Joel Young, from the Instrument Shop of the University of Oklahoma's Physics Department.

mismatches in the patterns; these mismatches could become evident in regions of reflectivity gradients.

Herzegh and Carbone (1984) have identified anomalously large negative differential reflectivities (e.g., down to about -6 dB) in regions of high reflectivity gradients near storm cores. These were caused by mismatched sidelobes in the high reflectivity regions, whereas the main lobe was located in a region of low reflectivity. But the radar antenna used in these measurements had quite high sidelobe levels. For example, the azimuthally integrated *two-way* sidelobe levels exceeded about -50 dB out to elevation angles of ± 10° from the boresight; similarly, high sidelobe levels were found for the patterns integrated in elevation! So it is not surprising that sidelobe mismatches of several dB would result in differential reflectivity biases when the sidelobes intersect a high reflectivity core (i.e., about 65 dBZ) and the main lobe is in a low reflectivity region (i.e., about 10 dBZ). Furthermore, it is likely that measurements of reflectivity in the low reflectivity regions could be contaminated by echo power entering through the sidelobes.

But if sidelobe levels are very small, then sidelobe mismatch wouldn't matter that much in biasing differential reflectivity or reflectivity. As a point of contrast to the poor performance of the antenna used for the storm observations reported by Herzegh and Carbone (1984), we refer to the *one-way* sidelobe levels seen in Fig. II.12d and deduce from it that the *two-way* sidelobe levels should be less than -70 dB over most of the ± 10° region, which is 20+ dB less than that reported by Herzegh and Carbone (op. cit.). Thus, many of the reported anomalies should disappear simply by lowering the sidelobe levels, even if sidelobes are poorly matched.

To determine the biases in the polarimetric variables, such as Z_{DR}, one can measure the H, V antenna patterns and convolve these with measured reflectivity fields (Pointin et al. 1988); this is basically the approach used by Herzegh and Carbone (1984). Although we could apply such techniques to the patterns measured for the KOUN1 antenna, we have elected not to follow this approach because inaccuracies in pattern measurements could falsify the bias results. We plan to modify the pedestal so that we can collect data with the beam vertically directed. In this case, Z_{DR}, and K_{DP} should be zero because the drop's axis of symmetry is vertical for non-canted drops.

II.8. Appendix: The relation between copolar and cross-polar amplitudes and phases and the tilt of the polarization ellipse

Discussion in Section II.3 suggests that the dual port feed radiates cross-polar fields about 33 dB below the copolar level. The cross-polar radiation from the feed can appear in the radiation pattern of the reflector for two reasons. First, even if the feed is not misaligned (i.e., $\alpha = 0^\circ$, see Fig. IV.1 and associated text for definition of α) and the horizontal (front) and vertical (back) ports are orthogonal, and the plane of the horizontal port is mechanically horizontal (the ports are defined as the rectangular apertures at the side of the feed's circular guide, see Fig. 6), the feed's cross-polar signal could be generated within the feed itself due to imperfections in the feed or due to asymmetries in the location of tuning stubs that are within the circular guide of the feed. Secondly, the cross-polar radiation could be caused by misalignment in the assembly of the feed onto the KOUN1 reflector.

A feed that is generating purely horizontally or vertically polarized waves would, because of misalignment of the feed, radiate both H, V waves. In this case, the polarization would still be linear, but the polarization direction would be tilted by an angle τ equal to the angle α that the feed is rotated around its axis. In general, elliptically polarized signals are transmitted, and the major axis of the polarization ellipse has a tilt which is a function of the phase difference β between the horizontal and vertical components of the electric field. In this appendix, we present relations which are useful in determining, from antenna pattern measurements, the tilt of the major axis of the polarization ellipse relative to the horizontal. Under the assumption that the feed generates purely H or V linear fields (i.e., if properly aligned), the measured tilt would be equal to the rotation α of the feed about its axis.

In the far field of the KOUN1 antenna, the electric field lies in planes (sometimes called the planes of polarization) perpendicular to the direction of propagation and is, in general, composed of two orthogonal components that have a phase difference β. Although the direction of propagation in our experimental setup is not zero, it is elevated by a sufficiently small (i.e., $\approx 0.5^\circ$) elevation angle relative to the horizontal, so we can still refer to these components as the horizontal and vertical electric fields. Thus, the two components can be written as

$$\begin{aligned} E_H &= A_H \cos \omega t \,, \\ E_V &= A_V \cos(\omega t + \beta) \,. \end{aligned} \tag{A1}$$

By eliminating the ωt between these two equations, we obtain the following relation:

$$\frac{E_V^2}{A_V^2} + \frac{E_H^2}{A_H^2} - 2\frac{E_V E_H}{A_V A_H}\cos\beta = \sin^2\beta \,, \tag{A2}$$

which is the general equation of an ellipse having its major and minor axis oriented at a tilt angle τ relative to the horizontal direction (Fig. II.A1). But if $\beta = 0$ or π, the equation reduces to

$$\frac{E_V}{A_V} \mp \frac{E_H}{A_H} = 0, \tag{A3}$$

which is the equation of a straight line inclined relative to the horizontal with a slope $\pm A_V/A_H$; the wave is linearly polarized, τ is negative if β is π, and is positive if β is 0. But if $\beta = \pm\pi/2$, then the wave is elliptically polarized, and the polarization ellipse has its major and minor axes parallel to the horizontal and vertical directions; if $A_V = A_H$, the wave is circularly polarized. The + or - sign determines the rotation of the electric field vector tip around the polarization ellipse.

To determine the relation between A_V, A_H, and τ, we express the general equation of the ellipse in terms of the new coordinate axes $E_{h'}$, $E_{v'}$ (Fig. II.A.1) which is aligned along the major

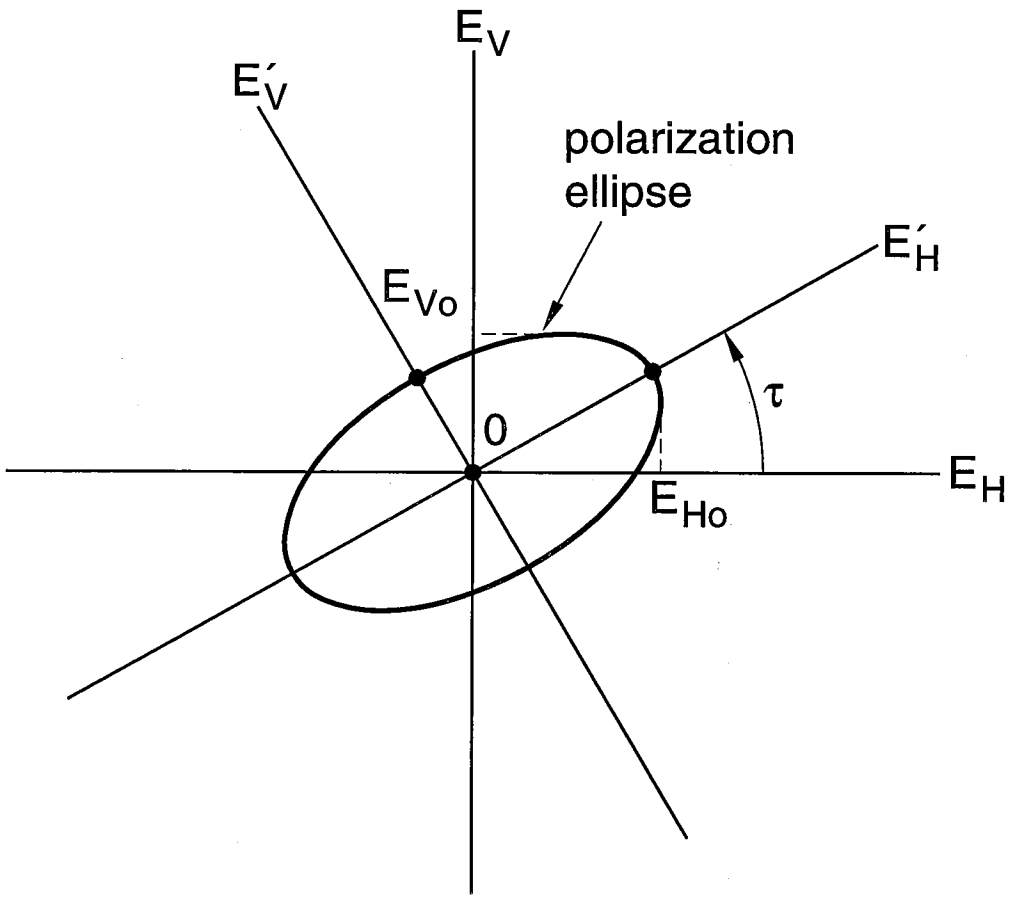

Fig. II.A.1 The polarization ellipse in the plane of polarization viewed toward the antenna under test.

and minor axes of the ellipse. This will give an equation similar to (A1) but expressed in terms of tilt angle τ. But since the major and minor axes are now aligned along the $E_{h'}, E_{v'}$ directions, the terms containing the cross product $E_{h'}E_{v'}$ must vanish. Setting the terms containing this cross product to zero gives the relation we seek. That is,

$$\tau = \frac{1}{2}\tan^{-1}\left(\frac{2A_H A_V \cos\beta}{A_H^2 - A_V^2}\right). \qquad \text{(A4)}$$

Note that if A_H, A_V are of equal magnitude and are simultaneously transmitted, as is planned for polarimetry measurements with the KOUN1 radar, $\tau = \pm\pi/4$ independent of β. Changing β from 0 to $\pm\pi/2$ changes the combined transmitted field from a linear polarized wave inclined at $\pi/4$ to a circularly polarized (RHC or LHC) wave. (Waves are elliptically polarized if $0 < \beta < \pm\pi/2$.) If $\beta = \pi + \theta$, the polarization ellipse will have a tilt fixed at $\tau = -\pi/4$, and the combined transmitted wave would be elliptically polarized and rotate around this ellipse in either a cw or ccw direction, depending on whether $-\pi/2 < \theta < 0$, or $0 < \theta < \pi/2$.

III. SELECTION OF THE POLARIMETRIC BASES AND IMPLEMENTATIONS

Common polarization bases are linear and circular. Two orthogonal wave polarizations, horizontal H and vertical V, comprise a linear polarization basis (there are other linear bases), whereas left and right hand circularly (LHC and RHC) polarized waves comprise the circular basis. Some of the earliest observations of precipitation with polarimetric radar used the circular basis (e.g., Barge 1970). Observations of severe storms showed relatively large circular depolarization ratios (i.e., CDR, the conversion of LHC to RHC polarization, or vice versa) caused by nonspherical hydrometeors in regions of high reflectivity. Because the converted or cross polarized signal is created by the slight nonsphericity present in most hydrometeors, it is weak, and the observations of CDR are confined to regions of high reflectivity. The emphasis of this earliest research was to detect and measure hail fall. Later, to improve rainfall measurements, Seliga and Bringi (1976) proposed a polarimetric radar with a linear basis in which H and V polarized waves are alternately transmitted. In the H, V polarization basis, H, V reflectivities are measured. Small differences in these reflectivities are caused by the nonsphericity of the rain drops, but in this case, measurements can be made in weak as well as strong reflectivity regions.

The early work with the linear polarization basis focused on combining differential reflectivity (or differential propagation phase, Seliga and Bringi 1978) with reflectivity (either H or V reflectivity) to estimate a two parameter drop size distribution, and thus, to eliminate the need to invoke an empirical relation between rain rate R and reflectivity factor Z. Battan (1973) lists no fewer than 69 different R, Z relations, obtained mostly from disdrometer data, showing large variations in these relations. Haddad and Rosenfeld (1997) present a rigorous mathematical basis for two empirical methods to derive R, Z relations from data. They demonstrate that the Probability Matching Method gives the optimal relation *if the original data is classified a priori in such a way that one might reasonably expect a one-to-one relation between R and Z.* Even if one finds a way to obtain this elusive one-to-one relation, there are many other factors (e.g., radar calibration, ground clutter, etc.), some more important than estimating drop size distributions or classifying rain types, which favor a polarimetric radar to improve the estimation of rainfall. Of critical importance to the favorable utility of a polarimetric radar is the selection of an appropriate polarization basis and its practical implementation. Considerations that can lead to a basis choice and a few options for designing the system are described next.

III.1. Linear vs. circular polarimetric bases

The selection of a polarimetric basis should be founded on the electric and geometric properties of the hydrometeors. For example, it does little good to select a basis for purely engineering reasons, as was the case for the pre-production NEXRAD (i.e., WSR-88D) radars for which a single state (i.e., RHC or LHC) circular basis was chosen for transmission and reception to reduce the radio frequency losses within the radar. This would have been a good engineering choice if hydrometeors were spherical, but since most are not, and many are strongly aspherical,

there is significant loss of echo power for propagation through severe storms (Doviak and Zrnic 1993, Section 8.5.2.3). The purpose of selecting a polarimetric basis, different than the single linear polarimetric state (i.e., horizontally polarized waves) of the present WSR-88D radars, is to retrieve additional and/or better information about the type and quantity of precipitation. Therefore, the selected polarimetric basis should be one that can provide the most accurate information about precipitation without noticeably degrading the existing capabilities of the WSR-88D, while constraining the cost of implementation and maintenance.

Most hydrometeors' shapes can be simply characterized by a spheroid. Thus, there are only a few essential hydrometeor properties that can influence the magnitude and phase of the back scattered polarimetric signals. These are:

1) its electrical size which is a function of the hydrometeor's complex susceptibilities (or polarizabilities) p_a, p_b (see Doviak and Zrnic 1993, Section 8.5.2.4 for definition; note that a,b replaces the v,h in their equations, and see web site www.noaa.nssl.gov/papers/books.html for other corrections) to produce electric dipole moments along its minor "a"or its major "b" axes (the susceptibilities are a function of the hydrometeor's refractive index, size, and axis ratio),

2) its apparent canting angle (i.e., the angle of the hydrometeor's axis of symmetry projected onto the plane of polarization),

3) the distribution or dispersion of the apparent canting angles (i.e., hydrometeors usually wobble and vibrate as they respond to turbulent forces and shear), and

4) its ellipticity or shape.

If there is no precipitation in the intervening media between the radar and the scattering volume (i.e., so that there are no propagation effects), the circular polarization basis provides relatively simple relations, as demonstrated in Section III.1.1, between the above cited properties and the elements (i.e., the measurands), $\langle s_{ij} s^*_{kl} \rangle$, of the backscattering covariance matrix $\boldsymbol{S}$. The indices $i, j, k,$ and l are r (RHC) or l (LHC) for the circular polarization basis and h or v for the H, V linear basis; the first and second indices refer to the polarization received and transmitted.

The electric field backscattered from a hydrometeor at range r_n is (Doviak and Zrnic 1993, Eq. 8.42),

$$E_{ij} = P_j^{1/2} \frac{s_{ij}(n) \eta_o^{1/2} g^{1/2} f(\theta,\phi)}{2\pi^{1/2} r_n^2} e^{-j2kr_n}, \qquad \text{(III.1)}$$

where s_{ij} is the ijth element of $\boldsymbol{S}$ for the nth hydrometeor, $k = 2\pi/\lambda$ is the precipitation-free wavenumber, P_j is the transmitted power that produces a "j" polarized incident electric field, g is the power gain of the antenna, $f(\theta,\phi)$ is the angular distribution of incident radiation, η_o is the

free-space impedance, and E_{ij} is the rms received field. The magnitude of the incident field at the scatterer is given by $P_j^{1/2}\eta_o^{1/2}f(\theta,\phi)/(2r_n\sqrt{\pi})$ so that the convention regarding the scattering coefficient s_{ij} agrees with that of McCormick and Hendry (1975); that is, if drops are spherical, $<|s_{hh}|^2> = <|s_{vv}|^2> = \sigma_b/4\pi$, where σ_b is the hydrometeor's backscattering cross section as defined by Eq. (3.6) of Doviak and Zrnic (1993). The elements of $\boldsymbol{S}$ are related to polarizabilities p_a, p_b of the spheroidal scatterer by the following equations:

$$\begin{aligned} s_{hh} &= k^2[(p_a - p_b)\sin^2\delta\sin^2\psi + p_b], \\ s_{vv} &= k^2[(p_a - p_b)\sin^2\delta\cos^2\psi + p_b], \\ s_{hv} &= s_{vh} = k^2(p_a - p_b)\sin^2\delta\sin\psi\cos\psi, \end{aligned} \tag{III.2}$$

where δ is the angle between the hydrometeor's axis of symmetry and the incident wave normal. (Fig. 8.15 in Doviak and Zrnic 1993, shows the geometric relation between the wave normal $\boldsymbol{k}$, canting angle ψ, and δ.) If hydrometeors are spherical, $p_a = p_b$.

III.1.1 The circular polarimetric basis in absence of propagation effects

The following equations, adapted from the works of McCormick and Hendry (1975) and Ryzhkov (1993), relate the backscattering matrix elements in the circular polarization basis to the hydrometeor's properties in the absence of propagation effects. In the convention adopted here, the first index (e.g., r) of the matrix element refers to the polarization (e.g., RHC) of the received echo, whereas the second index (e.g., l) refers to the polarization (e.g., LHC) of the field incident on the hydrometeor. Five principal measurands are

1) size:

$$<|s_{lr}|^2> = <\tilde{\sigma}>, \tag{III.3}$$

where $\tilde{\sigma}$ is a size parameter defined by

$$e^{j\phi_o/2}\tilde{\sigma}^{1/2} = \frac{k^2}{2}[(p_a - p_b)\sin^2\delta + 2p_b], \tag{III.4}$$

and is a real number, and ϕ_o is the phase angle of the complex right side of (III.4). If the hydrometeors are spherical, $\tilde{\sigma} = k^4|p_b|^2$, and because $4\pi<|s_{hh}|^2> \equiv \sigma_b$, it is seen from (III.2) that $<\tilde{\sigma}> = \sigma_b/4\pi$. The angle brackets denote an ensemble average of the hydrometeor's properties (e.g., equivolume diameter D_e, canting angle ψ, etc.); that is,

$$<s_{ij}s_{kl}^*> = \int P(\boldsymbol{X})s_{ij}s_{kl}^* d\boldsymbol{X}, \tag{III.5}$$

where $P(\boldsymbol{X})$ is the probability density of the scatterer's properties. For example, $P(\boldsymbol{X})$ could be the probability density $P(D_e)$ of drop sizes. Although $P(D_e)$ has the same functional dependence on D_e as does the drop size distribution $N(D_e)$, it is not equivalent to it; $P(\boldsymbol{X})$ is normalized so that the integral of $P(\boldsymbol{X})$ over all possible values of $\boldsymbol{X}$ is one, whereas $N(D_e)$ is normalized to the drop diameter and unit volume (Doviak and Zrnic 1993, p. 73). The drop size distribution, however, can be used to compute $P(D_e)$. That is,

$$P(D_e) = \frac{N(D_e)}{\int_o^\infty N(D_e)dD_e}. \tag{III.6}$$

2) size weighted shape:

$$<|s_{rr}|^2> = <\tilde{\sigma}|\nu|^2>, \tag{III.7}$$

where

$$\nu = \frac{(p_b - p_a)\sin^2\delta}{(p_a - p_b)\sin^2\delta + 2p_b} \tag{III.8}$$

is a complex number related to the shape of the hydrometeor. For water drops, ν is nearly a real number (i.e., it has a very small imaginary part) with values between 0 (for spheres) and 0.25 (for oblate drops of large diameter, i.e., $D \approx 6$ mm). Thus, the LHC back scattered wave is the only echo component if RHC waves are incident on spherical scatterers (i.e., $s_{rr} = 0$). If the scatterers are strongly oblate with their axis of symmetry vertical, and the incident wavenormal is horizontal (i.e., $\delta = \pi/2$), $\nu \approx 1$.

3) a canting angle measurand:

$$<s_{rr}s_{lr}^*> = -r<\tilde{\sigma}\nu>e^{-j2\bar{\psi}}, \tag{III.9}$$

where $\bar{\psi}$ is the mean canting angle, and

$$r = e^{-2\sigma_\psi^2} \tag{III.10}$$

measures the effects of canting angle dispersion about $\bar{\psi}$; σ_ψ is the standard deviation of the canting angles (Oguchi 1983). The above three measurands can be obtained by transmitting RHC

polarized waves and receiving both RHC and LHC waves. This had been the mode of operation (except that LHC waves were transmitted) of the 10 cm polarimetric radar in Alberta, Canada. This radar was operated by the Alberta Research Council for the primary purpose of distinguishing rain from hail (McGuinness et al. 1987). The principals of these measurements are discussed by McCormick and Hendry (1975) who show that because v is nearly real (for hydrometeors, except those that are large and asymmetrical), the mean canting angle can be estimated from the argument of $\langle s_{rr} s_{lr}^{*} \rangle$. Moreover, using the scattering coefficients published by Oguchi (1973) for an assumed Laws-Parsons drop size distribution, and the Spilhaus (1948) shape relation, McCormick and Hendry (1975) provided a method whereby the canting angle dispersion can be approximately estimated from $|\langle s_{rr} s_{lr}^{*} \rangle| / [\langle |s_{rr}|^2 \rangle \langle |s_{lr}|^2 \rangle]^{1/2}$.

These three measurands are insufficient, however, to extract accurately the four hydrometeor properties listed previously. But if RHC and LHC waves are alternately transmitted, then there are two other measurands. They are

4) the conjugate canting angle measurand:

$$\langle s_{ll} s_{rl}^{*} \rangle = -r \langle \tilde{\sigma} v \rangle e^{+j2\bar{\psi}} \tag{III.11}$$

and

5) a measurand whose phase gives the mean canting angle:

$$\langle s_{rr} s_{ll}^{*} \rangle = -r \langle \tilde{\sigma} |v|^2 \rangle e^{-j4\bar{\psi}} . \tag{III.12}$$

Because the argument of the measurand $\langle s_{rr} s_{ll}^{*} \rangle$ is only a function of $\bar{\psi}$, the mean canting angle can be found directly from it. The calculation of the canting angle dispersion, on the other hand, requires two of the measurands, $\langle |s_{rr}|^2 \rangle$ and $\langle s_{rr} s_{ll}^{*} \rangle$, but no assumptions are needed about the distributions of hydrometeor size and shape.

Although there are other measurands (in general, there are 16, but because of reciprocity, the four by four covariance matrix reduces to a three by three matrix), they are either equal to the listed ones (e.g., $\langle |s_{rr}|^2 \rangle = \langle |s_{ll}|^2 \rangle$) or are complex conjugates of them. Both RHC and LHC waves are required to be *alternately* transmitted and *simultaneously* received to obtain complete polarimetric information. The simultaneous transmission of both components of a polarimetric basis can simply lead to the effective transmission of a single component in another polarimetric basis and, thus, might not provide any additional information about the properties of the hydrometeors.

III.1.2 The H, V linear polarimetric basis in absence of propagation effects

The intrinsic polarimetric measurands which can be estimated using a radar that processes the H, V polarized back scattered signals (Ryzhkov 1993) consist of

1) horizontal reflectivity:

$$<|s_{hh}|^2> = <\tilde{\sigma}> + 2Re\{<\tilde{\sigma}v>\}r\cos 2\bar{\psi} + \frac{<\tilde{\sigma}|v|^2>}{2}(1 + r^4\cos 4\bar{\psi}). \qquad \text{(III.13)}$$

2) vertical reflectivity:

$$<|s_{vv}|^2> = <\tilde{\sigma}> - 2Re\{<\tilde{\sigma}v>\}r\cos 2\bar{\psi} + \frac{<\tilde{\sigma}|v|^2>}{2}(1 + r^4\cos 4\bar{\psi}), \qquad \text{(III.14)}$$

where $Re\{\}$ denotes the real part of the argument. For hydrometeors that are nearly spherical, $p_a \approx p_b$, so that from (III.8), $v \approx 0$. Thus, the second and third terms in the above equations are small compared to the first term. It is the presence of these small terms which result in the differential reflectivity factor defined (in dB) as

$$Z_{DR} = 10\log_{10}\left(\frac{<|s_{hh}|^2>}{<|s_{vv}|^2>}\right). \qquad \text{(III.15)}$$

3) the depolarization measurand:

$$<|s_{hv}|^2> = \frac{1}{2}<\tilde{\sigma}|v|^2>(1 - r^4\cos 4\bar{\psi}). \qquad \text{(III.16)}$$

The ratios $<|s_{hv}|^2>/<|s_{hh}|^2>$ and $<|s_{hv}|^2>/<|s_{vv}|^2>$ are the linear depolarization ratios which measure the tilt of the symmetry axis and the effectiveness that nonspherical scatterers have in converting the polarized waves from H to V, or vice versa.

4) the H, V correlation measurand:

$$<s_{hh}s_{vv}^*> = <\tilde{\sigma}> - 2jIm\{<\tilde{\sigma}v>\}r\cos 2\bar{\psi} - \frac{<\tilde{\sigma}|v|^2>}{2}(1 + r^4\cos 4\bar{\psi}), \qquad \text{(III.17)}$$

where $Im\{\}$ is the imaginary part of the argument. Two other rarely used measurands are

5)

$$\langle s_{hh} s_{hv}^{*} \rangle = -\langle \tilde{\sigma} v^{*} \rangle r \sin 2\bar{\psi} + \frac{\langle \tilde{\sigma} | v |^{2} \rangle}{2} r^{4} \sin 4\bar{\psi} \qquad \text{(III.18)}$$

and

6)

$$\langle s_{vv} s_{hv}^{*} \rangle = -\langle \tilde{\sigma} v^{*} \rangle r \sin 2\bar{\psi} - \frac{\langle \tilde{\sigma} | v |^{2} \rangle}{2} r^{4} \sin 4\bar{\psi}. \qquad \text{(III.19)}$$

Although the measurands in the linear basis have a more complicated relation between the hydrometeor's properties than that found with the circular basis (Section III.1.1), propagation effects and other practical considerations discussed in the next sections negate this apparent difficulty with the linear polarimetric basis.

III.1.3 The H, V linear polarimetric basis in the presence of propagation effects

Because most hydrometeors have axes of symmetry vertical, H or V linearly polarized waves practically remain in the same pure polarization state as they propagate through rain (i.e., a horizontally transmitted wave remains horizontal). In contrast, circularly polarized waves depolarize, generally to a partially polarized elliptical state, as they propagate through rain, and propagation effects must be considered to obtain the backscattering coefficients. Although there is no depolarization of H and V waves propagating through precipitation (if the axes of symmetry are vertical), there could be differential attenuation and differential phase shift between the two waves. Nevertheless, the waves propagate independently. For weather radars operating at long wavelengths (i.e., > 10 cm), attenuation is usually negligible. This permits direct measurement of many of the back scattering coefficients of the hydrometeors within the sampled resolution volume, whereas measurements with circularly polarized waves require corrections.

The backscattering properties of the hydrometeors within the sampled resolution volume are, for the most part, the ones sought after by the radar meteorologists. One exception is the specific differential phase which is a function of the forward scattering properties of the propagation medium. The specific differential phase K_{DP} (i.e., the difference in H, V propagation wavenumbers $k_{h,v}$) is used to estimate rainfall without the need to calibrate the radar.

If there is rain between the radar and the sampled resolution volume, the wave's polarization can undergo change as it propagates to this volume, and the wave incident on it might no longer have the same polarization as that transmitted. The changes in polarization state can be determined by applying the normalized (i.e., common factors are omitted) transmission matrix to the incident and scattered fields. Canting angles are believed to be narrowly distributed about a

mean near zero (Jameson 1983; Beard and Jameson 1983). Under these conditions, the transmission matrix $\boldsymbol{T}$ reduces to

$$\boldsymbol{T} = \begin{bmatrix} T_h & 0 \\ 0 & T_v \end{bmatrix}, \tag{III.20}$$

in which the matrix elements,

$$\begin{aligned} T_h &= \ell_{hv}^{-1/2} e^{-j\frac{\phi_{DP}}{2} + j\sigma_\psi^2 \frac{\phi_{DP}}{2}} \\ T_v &= e^{-j\sigma_\psi^2 \frac{\phi_{DP}}{2}}, \end{aligned} \tag{III.21}$$

are obtained from more general formulas of Oguchi (1983). The propagation differential phase ϕ_{DP} is the phase difference between the received H and V waves in absence of canting angle dispersion, and (III.21) assumes that the phase difference at transmission is zero, ℓ_{hv} ($\ell_{hv} \geq 1$) is the one-way differential *power* loss.

The transformation matrix $\boldsymbol{V}$, which relates the polarization state of the electric field vector (E_h ,E_v) as it leaves the radar to that polarization state of the scattered wave received by the radar, is, therefore,

$$\boldsymbol{V} \equiv \begin{bmatrix} V_{hh} & V_{hv} \\ V_{hv} & V_{vv} \end{bmatrix} = \begin{bmatrix} T_h & 0 \\ 0 & T_v \end{bmatrix} \cdot \begin{bmatrix} s_{hh} & s_{hv} \\ s_{vh} & s_{vv} \end{bmatrix} \cdot \begin{bmatrix} T_h & 0 \\ 0 & T_v \end{bmatrix}. \tag{III.22}$$

Thus, the measured differential reflectivity factor $\tilde{Z}_{dr}$, in presence of propagation effects, is

$$\tilde{Z}_{dr} \equiv \frac{<|V_{hh}|^2>}{<|V_{vv}|^2>} = \frac{|T_h|^4 <|s_{hh}|^2>}{|T_v|^4 <|s_{vv}|^2>} = \frac{1}{\ell_{hv}^2} Z_{dr}, \tag{III.23}$$

where Z_{dr} is the intrinsic differential reflectivity (i.e., the differential reflectivity of the sampled resolution volume). Equation (III.23) indicates that the measured or observed differential reflectivity factor $\tilde{Z}_{dr}$ is biased by the square of the differential transmission loss. In stratified rain at 10 cm and longer wavelengths, the attenuation is usually negligible, and $\tilde{Z}_{dr}$ is a very good estimate of Z_{dr}. In convective storms and along squall lines, the differential transmission loss can be significant, and the loss needs to be estimated. Bringi et al. (1990) have shown that it is

possible to estimate the two-way attenuation and the differential attenuation by means of the propagation differential phase ϕ_{DP}.

Likewise, the observed linear depolarization ratio $\tilde{L}DR_{vh}$ (Doviak and Zrnic 1993, p. 242),

$$\tilde{L}dr_{vh} \equiv \frac{<|V_{vh}|^2>}{<|V_{hh}|^2>} = \frac{|T_v|^2 <|s_{hv}|^2>}{|T_h|^2 <|s_{hh}|^2>} = \ell_{hv} \cdot Ldr_{vh}, \qquad \text{(III.24)}$$

is, in general, a biased estimated of the intrinsic Ldr_{vh}. (The lower case 'dr' is used to denote the ratio, whereas the upper case 'DR', e.g., LDR_{hv}, is used to express the ratio in decibel units.)

The last important linear polarimetric parameter is the measured correlation coefficient at zero lag $\tilde{\rho}_{hv}(0)$ defined by

$$\tilde{\rho}_{hv}(0) \equiv \frac{<V_{hh}V_{vv}^*>}{\sqrt{<|V_{hh}|^2> <|V_{vv}|^2>}} = \frac{|<s_{hh}s_{vv}^*>|}{\sqrt{<|s_{hh}|^2> <|s_{vv}|^2>}} e^{j\phi_{DP}(1 - 2\sigma_\psi^2) - j(\delta_{vv} - \delta_{hh})}, \qquad \text{(III.25)}$$

in which $\delta_{vv} - \delta_{hh}$ is the phase shift (usually very small) between H and V waves produced upon backscatter from nonspherical scatterers. If H and V waves are simultaneously transmitted and received, $\tilde{\rho}_{hv}(0)$ is directly computed, but if H and V waves are alternately transmitted, $\tilde{\rho}_{hv}(0)$ needs to be estimated from H, V signals obtained from alternate samples. The measured differential propagation phase is biased by the dispersion in the canting angles of the drops along the propagation path, whereas the magnitude of the correlation coefficient is not biased by propagation effects. The differential propagation phase ϕ_{DP}, although biasing the intrinsic differential phase shift ($\delta_{vv} - \delta_{hh}$) upon scatter, is a very useful parameter because it is strongly related to rainfall rate. Thus, ϕ_{DP} is not looked upon as a nuisance parameter but is sought after to improve rainfall estimates.

III.1.4 The circular polarimetric basis in presence of propagation effects

The transformation from a linear to a circular polarization basis is given by

$$\boldsymbol{E}_c = \boldsymbol{C}\boldsymbol{E}_\ell, \qquad \text{(III.26)}$$

where $\boldsymbol{E}_c$ is a column vector whose two elements are the RHC and LHC components of the circularly polarized electric field, $\boldsymbol{E}_l$ is the column vector for H, V linear polarized waves, and $\boldsymbol{C}$ is defined by

$$\boldsymbol{C} \equiv \frac{1}{\sqrt{2}}\begin{bmatrix} 1 & j \\ 1 & -j \end{bmatrix}. \tag{III.27}$$

We can use the matrix $\boldsymbol{C}$ to convert the incident circular polarimetric basis to a linear one so that we can directly use the elements of the matrices for backscatter $\boldsymbol{S}$ and transmission $\boldsymbol{T}$ already specified for the linear basis. Thus, the transformation matrix $\boldsymbol{V}^{(c)}$ for circularly polarized waves is

$$\boldsymbol{V}^{(c)} \equiv \begin{bmatrix} V_{rr} & V_{lr} \\ V_{rl} & V_{ll} \end{bmatrix} = \frac{1}{2}\begin{bmatrix} 1 & j \\ 1 & -j \end{bmatrix} \cdot \begin{bmatrix} T_h & 0 \\ 0 & T_v \end{bmatrix} \cdot \begin{bmatrix} s_{hh} & s_{hv} \\ s_{hv} & s_{vv} \end{bmatrix} \cdot \begin{bmatrix} T_h & 0 \\ 0 & T_v \end{bmatrix} \cdot \begin{bmatrix} 1 & 1 \\ j & -j \end{bmatrix}, \tag{III.28}$$

from which we find that

$$\begin{aligned} V_{rr} &= \frac{1}{2}(T_h^2 s_{hh} + 2jT_h T_v s_{hv} - T_v^2 s_{vv}), \\ V_{lr} = V_{rl} &= \frac{1}{2}(T_h^2 s_{hh} + T_v^2 s_{vv}), \\ V_{ll} &= \frac{1}{2}(T_h^2 s_{hh} - 2jT_h T_v s_{hv} - T_v^2 s_{vv}). \end{aligned} \tag{III.29}$$

From the elements of the transformation matrix $\boldsymbol{V}^{(c)}$, one can calculate the various covariance terms associated with reception of the two circularly polarized components. Much of the early effort in utilizing the matrix elements in (III.29) (which include the effects of propagation) was to extract the sampled resolution volume's backscattering matrix elements; this required corrections for the effects of propagation (e.g., Jameson and Davé 1988; Bebbington et al. 1987).

On the other hand, because rainfall estimates are derived from covariance terms associated with the linear polarimetric basis, the usual procedure in estimating precipitation type and fall rate is to extract the covariance terms in the linear polarimetric basis from the components of $\boldsymbol{V}^{(c)}$ (e.g., McGuinness et al. 1987; Holt 1988). In particular, because the specific differential phase (i.e., K_{DP}, the range rate of change of the propagation differential phase ϕ_{DP}) and the differential reflectivity Z_{DR} have many robust properties for the measurement of rainfall (Ryzhkov and Zrnic 1996; Zrnic and Ryzhkov 1996), we shall focus our attention on the extraction of ϕ_{DP} and Z_{DR} from the elements of $\boldsymbol{V}^{(c)}$.

Torlaschi and Holt (1993) showed that, under the condition that all drops are equi-oriented with a vertical axis of symmetry, the differential phase is related to the covariance elements by

$$arg\left\{\frac{<|V_{lr}|^2>-<|V_{rr}|^2>}{2} - jIm[<V_{rr}V_{lr}^*>]\right\} = \phi_{DP} + \delta_l, \tag{III.30}$$

where δ_l is

$$\delta_l = arg\left\{\frac{<|s_{lr}|^2> - <|s_{rr}|^2>}{2} + jIm[<s_{rr}s_{lr}^*>\right\}. \tag{III.31}$$

Torlaschi and Holt (1993) state that $\delta_l \approx 0$ if scatter is from rain at 10 cm wavelength. Thus, using nonswitched (e.g., only RHC waves are transmitted) circularly polarized transmitted waves and measurements of the covariance elements for the two received components of circular polarization, the argument of the bracketed term should give an unbiased estimate of propagation differential phase ϕ_{DP}.

On the other hand, if we substitute the matrix elements (III.29) for the terms within the argument of (III.3.0), we obtain

$$\begin{aligned}&\frac{<|V_{lr}|^2>-<|V_{rr}|^2>}{2} - jIm\{<V_{rr}V_{lr}^*>\} = \\ &\frac{1}{2}Re\{T_h^2T_v^{*2}<s_{hh}s_{vv}^*>\} + \frac{j}{2}Im\{T_h^2T_v^{*2}<s_{hh}s_{vv}^*>\} - \frac{1}{2}|T_hT_v|^2<|s_{hv}|^2>,\end{aligned} \tag{III.32}$$

a solution valid even if drops are not equi-oriented. The last term on the right of this equation has been ignored by Torlaschi and Holt (1993) because $s_{hv} = 0$ if *all* drops have a vertical axis of symmetry. By substituting (III.21) into the above equation, we obtain

$$\frac{<|V_{lr}|^2>-<|V_{rr}|^2>}{2} - jIm\{<V_{rr}V_{lr}^*>\} = \frac{1}{2}\ell_{hv}^{-1}\left[e^{-j\phi_{DP}(1-2\sigma_\psi^2)}<s_{hh}s_{vv}^*>-<|s_{hv}|^2>\right]. \tag{III.33}$$

It can be shown that for rain, the argument of $<s_{hh}s_{vv}^{*}>$ is much less than 1°, and so the argument of the left side of (III.3.3) is, to a good approximation, given by

$$arg[L.S.] = arg\left[e^{-j\phi_{DP}(1-2\sigma_{\psi}^{2})} - \frac{<|s_{hv}|^{2}>}{<|s_{hh}s_{vv}^{*}|>}\right], \tag{III.34}$$

which can be written as

$$arg[L.S.] = arg\left[e^{-j\phi_{DP}(1-2\sigma_{\psi}^{2})} - \frac{Ldr_{vh}\sqrt{Z_{dr}}}{|\rho_{hv}(0)|}\right]. \tag{III.35}$$

For rain within the sampled resolution volume, the last term is negligible with respect to the first (Doviak and Zrnić 1993, see Table 8.1 for values of Ldr, etc.). However, if the scattering volume is filled with a mixture of rain and hail, Ldr can be as large as 0.1, $|\rho_{hv}(0)|$ is larger than 0.9, and $Z_{dr} \approx 1$ (op. cit.). Therefore, the second term has a magnitude about 10% of the first term in the brackets, and correspondingly, there could be a 10% bias in the estimate of ϕ_{DP}. It can be shown that the corresponding biases in K_{DP} and rainrate R are of the same order as for ϕ_{DP}. Although the 10% error is a worst case situation, conditions of rain hail mixture are often encountered, and thus, the second term in (III.3.5) could have an impact on the measurment of rainfall.

Torlaschi and Holt (1993) also showed that the differential reflectivity factor can be derived from the elements of the transformation matrix:

$$Z_{DR} = 10\log\frac{<|V_{lr}|^{2}> + <|V_{rr}|^{2}> - 2Re(<V_{rr}V_{lr}^{*}>)}{<|V_{lr}|^{2}> + <|V_{rr}|^{2}> - 2Re(<V_{rr}V_{lr}^{*}>)} + \hat{A}_{hv}, \tag{III.36}$$

where A_{hv} is the differential attenuation which can be estimated from measurements of ϕ_{DP} (Bringi et al. 1990).

It is apparent that computation of Z_{DR} and ϕ_{DP} involves three measurands (provided the differential attenuation is zero), whereas a similar computation in a linear basis involves two for the Z_{DR} measurand, and one for ϕ_{DP} measurand. The cross-polar and copolar powers in the circular polarimetric basis can differ by as much as ± 20 dB, depending on ϕ_{DP}. Therefore, noise can degrade the correlation $<V_{rr}V_{lr}^{*}>$, which is the product of a weak and strong signal.

III.1.5 Comparisons of linear and circular polarimetric bases

As pointed out earlier, because most hydrometeors are nearly spherical, an obvious limitation of the circular basis is that the measurands, with the exception of (III.3.), are products of a strong signal with a weak one. Thus, in general, hydrometeor information will be strongly corrupted by

receiver noise except in regions of very strong reflectivity (e.g., Barge (1970) was able to extract $<|s_{rr}|^2>$ data only in regions where reflectivity factor is larger than 45 dBZ). In turn, other polarimetric parameters that are usefully related to rainfall measurements (e.g., specific differential phase, K_{DP} , and differential reflectivity Z_{DR}) cannot be reliably retrieved in many rainy regions, as found by English et al. (1991).

An important application, if not the most important of a polarimetric capability on a weather radar, is to improve the accuracy of rainfall measurements. Differential reflectivity, Z_{DR} , and specific differential phase, K_{DP}, emerge as powerful measurands because they have proven to provide robust estimates of rainfall, overcoming many of the limitations inherent in the *Z, R* relations (presently used for the network of WSR-88Ds). Although K_{DP} can be calculated from the reception of RHC and LHC polarized waves, the calculation is indirect, the signals are weak, and errors (already large from computations using linear polarization data in which signals are strong) would be much larger.

Furthermore, hydrometeor shape is oblate for large raindrops, and the axes of symmetry remain essentially aligned with the vertical in absence of strong wind shear or air accelerations (Section IV.2). Thus, for beams at low elevation angles, the propagation medium will convert RHC polarization to LHC polarization, but it will not convert H to V polarized waves, nor vice versa. Because circularly polarized waves are converted from one sense to another, there could be severe underestimates of reflectivity (e.g., see Fig. 8.12 of Doviak and Zrnic' 1993) if only the copolar (or main) channel is used to estimate reflectivity. The reflectivity factor Z_c for circularly polarized waves, normalized to the reflectivity factor Z_h for horizontally polarized waves, is given by

$$\frac{Z_c}{Z_h} \equiv \frac{<|V_{lr}|^2>}{<|V_{hh}|^2>} = \frac{1}{4}[1 + A + B], \qquad \text{(III.37)}$$

where

$$A \equiv \frac{\ell_{hv}^2}{Z_{dr}} \ , \quad B \equiv \frac{2\ell_{hv}|\rho_{hv}(0)|}{\sqrt{Z_{dr}}}\cos[\phi_{DP}(1 - 2\sigma_\psi^2)]. \qquad \text{(III.38)}$$

This equation, in decibel units, is plotted in Fig. III.1 as a function of the differential phase ϕ_{DP}, assuming $Z_{DR} = 2$ dB (the upper case subscripts denote decibel units), $|\rho_{hv}(0)| = 0.95$, $\ell_{hv} = 1$, and $\sigma_\psi^2 = 0$. It is quite apparent that if ϕ_{DP} is larger than about 20°, the bias in Z_c is significant, and for $\phi_{DP} > 50°$, it is unacceptable. Torlaschi and Pettigrew (1990) showed that for observations of convection storms with circularly polarized transmissions, propagation effects at a 10 cm wavelength can lead to an underestimation of the reflectivity factor by an amount that is of the same order of magnitude as the attenuation at 5 cm wavelengths.

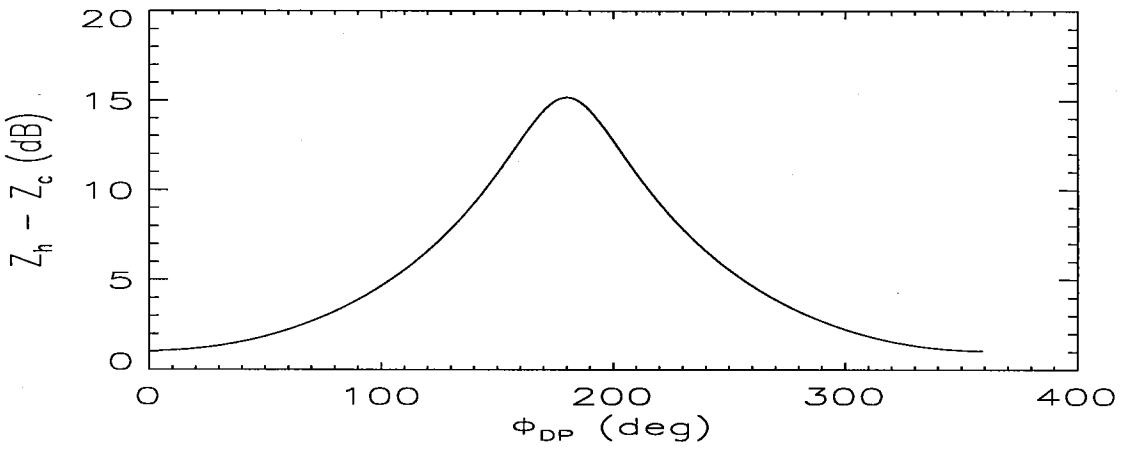

Fig. III.1 The difference in reflectivities measured (in dB) with linearly and circularly polarized waves versus propagation differential phase ϕ_{DP}. Canting angle dispersion and diffential attenuation are assumed negligibly small; Z_{DR} = 2 dB and $|\rho_{hv}(0)|$ = 0.95 are the intrinsic values in the sampled resolution volume.

The first several WSR-88D radars that were delivered to the USA's National Weather Service had the circular polarization basis implemented, but there was no provision to overcome the reflectivity bias caused by propagation through severe storms in which many hydrometeors are strongly nonspherical. To obtain a meaningful measure of the hydrometeor's reflectivity factor, it is mandatory that both LHC and RHC echo powers be added. These and other reasons might be why radar meteorologists have selected the linear polarization basis for seven of the eight 10-cm wavelength polarimetric radars used at research facilities (Zrnic 1996).

The Circular Depolarization Ratio (Cdr), defined as

$$Cdr \equiv \frac{<|s_{rr}|^2>}{<|s_{lr}|^2>}, \qquad \text{(III.39)}$$

is invariant to the orientation of the drop's symmetry axis, unlike that for the linear depolarization ratio. Thus, *in absence of propagation effects,* the Cdr is directly measured, and it is more useful in quantifying the ellipticity of nonspherical scatterers such as ice crystals. Barge (1974), using drop size spectra from various geographical regions, showed that for the same reflectivity factor, tropical rain had CDR (upper case DR is used to denote the ratio in dB) values several dB lower than that of other rains. This observation suggests that tropical rain has a relatively high abundance of small drops which are nearly spherical.

But the CDR independence on drop axis orientation does not outweigh the advantage that the linear basis has for the measurement of rainfall. Moreover, *in the presence of precipitation along the propagation path* the circular basis is handicapped (McGuinness et al. 1987), as explained in Section III.1.4. For example, the Cdr has a dependence on differential propagation phase given by

$$Cdr \equiv \frac{<|V_{rr}|^2>}{<|V_{lr}|^2>} = \frac{1 + A - B + 4\,\ell_{hv}\,LDR_{vh}}{1 + A + B}. \qquad \text{(III.40)}$$

This equation, in decibel units, is plotted in Fig. III.2 for the same parameters as those used to plot Fig. III.1. Fig. III.2 demonstrates the significance that propagation effects have on the measurement of *Cdr*. Thus, measurements with a circular polarization basis require correction for propagation effects as suggested by, for example, Bebbington, et al. (1987).

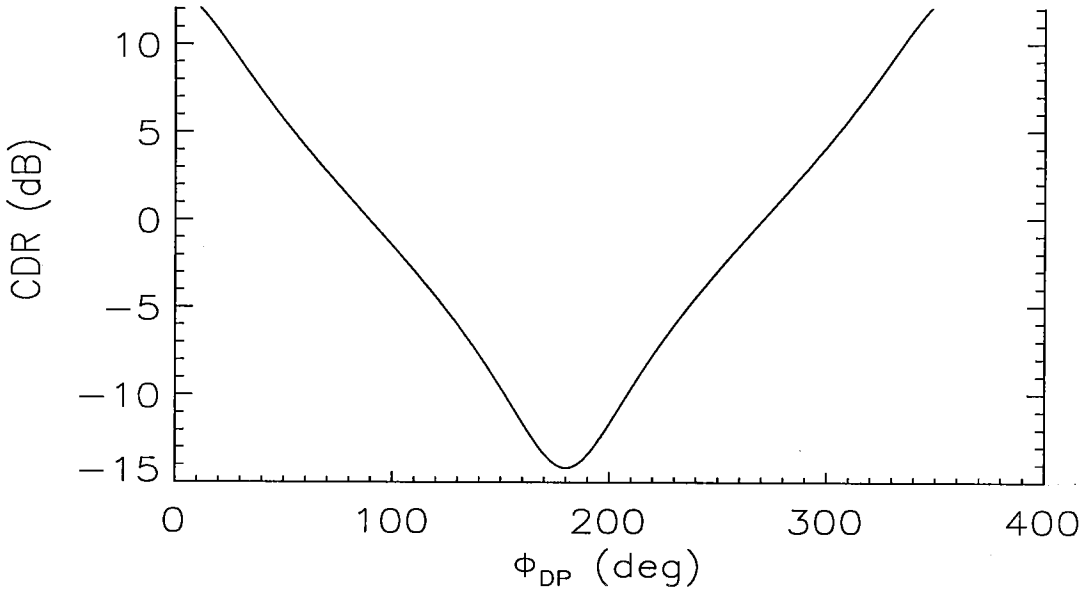

Fig. III.2 The Circular Depolarization Ratio (CDR) in dB versus ϕ_{DP}. The intrinsic CDR value is that for $\phi_{DP} = 0$. Parameter values are the same as in Fig. III.1.

As discussed in Section III.1.1, the canting angle dispersion can be estimated, in absence of propagation effects, from $ORTT \equiv |<s_{rr}s_{lr}^*>| / [<|s_{rr}|^2><|s_{lr}|^2>]^{1/2}$. In presence of precipitation along the propagation path, however, the elements of the $\boldsymbol{V}^{(c)}$ must be used in place of s_{rr} etc. Thus, we obtain

$$ORTT \equiv \frac{|\langle s_{rr} s_{lr}^{*} \rangle|}{\langle |s_{rr}|^2 \rangle^{1/2} \langle |s_{lr}|^2 \rangle^{1/2}}$$

$$= \frac{\left| 1 - A + j \frac{2\ell_{hv} |\rho_{hv}(0)|}{\sqrt{Z_{dr}}} \sin[\phi_{DP}(1 - 2\sigma_{\psi}^2)] \right|}{(1 + A + B)^{1/2} \left(1 + A - B + 4\ell_{hv} LDR_{vh}\right)^{1/2}}, \qquad \text{(III.41)}$$

from which we can deduce the effects of the propagation medium. This equation is plotted in Fig. III.3. for the same parameters as for the previous figures. It demonstrates that propagation effects significantly bias *ORTT* and corrections are necessary to estimate the intrinsic canting angle dispersion within the sampled resolution volume.

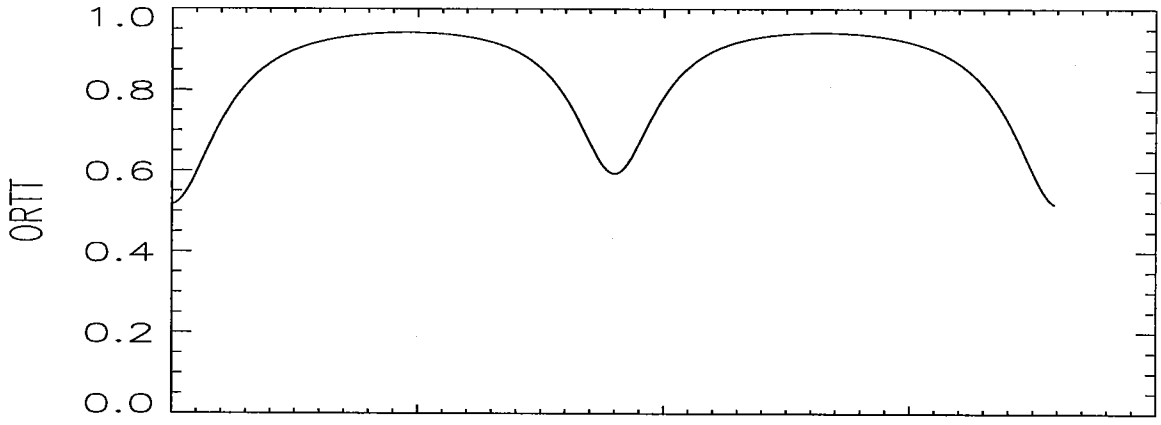

Fig. III.3. The canting angle dispersion parameter *ORTT* vs. ϕ_{DP}. The intrinsic *ORTT* value is that for $\phi_{DP} = 0$. Parameter values are the same as in Fig. III.1.

In conclusion, although the circular polarization basis can, in principle, provide estimates of K_{DP} without switching the transmitted polarization, the estimation of this parameter would inevitably cause problems in weaker showers. But with circular polarization, the cross-polar signal does not depend on the orientation of hydrometeors; furthermore, in combination with the copolar signal, it leads to the measurement of the mean apparent canting angle. This advantage of the circular polarization basis is overcome by what linear polarization offers for quantitative measurements of rainfall without the need for extensive corrections. Therefore, our choice rests with the linear H, V basis.

III.2. Methods of implementing the linear polarization basis

Several options exist for implementing the linear polarization basis. The microwave circuits in the KOUN1 can be configured to test the most promising polarimetric schemes. Scientists at NSSL, NCAR, and CSU have experience with alternately transmitting H, V polarizations wherein a high power ferrite switch and a single receiver are used (Fig. III.4). This arrangement has deficiencies (to be discussed shortly) that prompted other approaches.

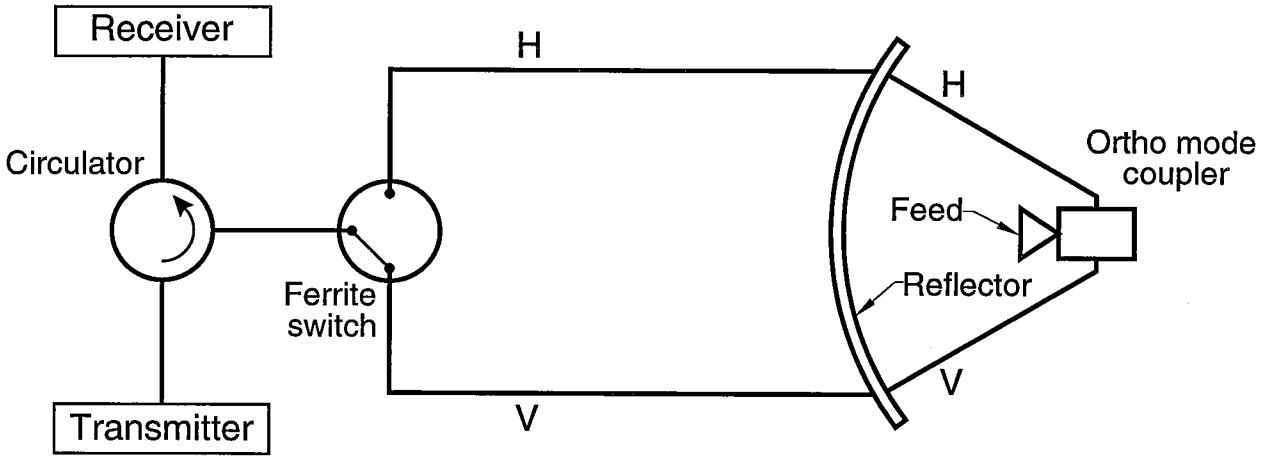

Fig. III.4 A simplified block diagram of the system with a high-power ferrite switch to alternately transmit and receive H and V polarized waves.

NCAR has implemented, in their S-POL polarimetric radar, a high speed rotary switch to alternately transmit H, V polarized waves and a pair of receivers (Fig. III.5). The rotary switch is in the transmission path, and it alternately channels the power to the H and V waveguides that lead to the H and V ports on the antenna feed. The transmitted pulse repetition time (PRT $\equiv T_s$) is controlled by the rotary switch, and the transmitted power is synchronized so that it passes through the switch when it is open to the selected port. A principal advantage of this mechanical switch is its excellent isolation (i.e., $\approx$ 50 dB between ports[9]), which is much superior to the high-speed high-power ferrite switch. Three disadvantages of this arrangement are a relatively short lifetime, excessive acoustic noise that the switch generates, and lack of suitability for the batch mode transmission (Doviak and Zrnic 1993) on the WSR-88D.

[9] Private communication 11/22/96 from Jon Lutz, NCAR/ATD, Boulder, CO.

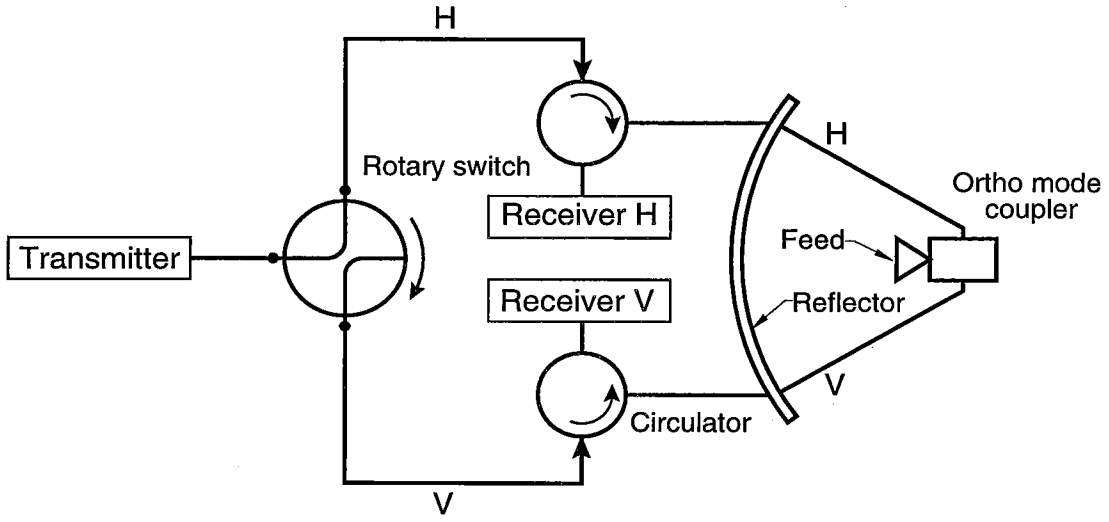

Fig. III.5 A simplified block diagram of the system with a high speed rotary switch (NCAR's S-Pol polarimetric radar) to alternately transmit H and V polarized waves. Two receivers are used for simultaneous reception of copolar and cross-polar echoes.

CSU has two transmitters alternately servicing the H and V ports of the antenna (Fig. III.6). This aproach achieves very good isolation between the H and V signal paths and redundancy of the transmitter chain. But the cost of this system is high. CSU has also tried simultaneous transmission of H and V polarizations with switched reception (Section IV.4). Detailed assesments of simultaneous vs. alternate transmission and reception is presented in Section III.3.

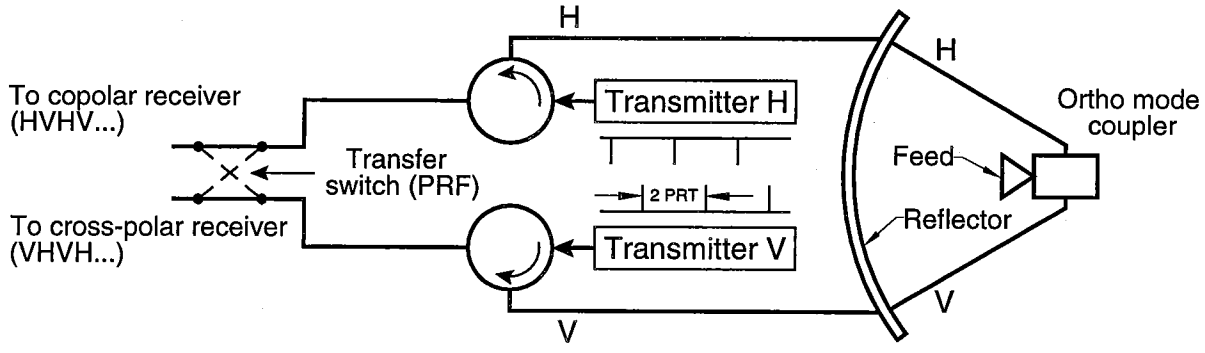

Fig. III.6 A simplified block diagram of a system (CSU's polarimetric radar) with two transmitters and a transfer switch to alternately transmit and receive, in copolar and cross-polar channels, H and V polarized waves. The transfer switch obviates the need to maintain high precision gain balance in the two receiving channels.

NSSL is proposing simultaneous transmission and reception of the H,V polarizations. The schematic in Fig. III.7 illustrates the basics of the system. (A detailed schematic is in Fig. III.8.) Two modes of operation are planned, a dual polarization mode (power splitter/switch connected to the H and V channels) and a single polarization mode (power splitter/switch disconnected from the V channel). A change from mode one to the other will take but a few minutes (mainly because a different software will need to be loaded into the host computer and signal processor memories, and because a diagnostic test of the system needs to be done after any change). The single polarization (H) mode is needed to test other potential improvements for the network of WSR-88Ds. Simultaneous transmission and alternate reception will also be tested; in this configuration, there is one receiver which is alternately switched between the H and V ports (Fig. III.8; phase 1). If needed, our configuration could accommodate a high-power ferrite switch as well.

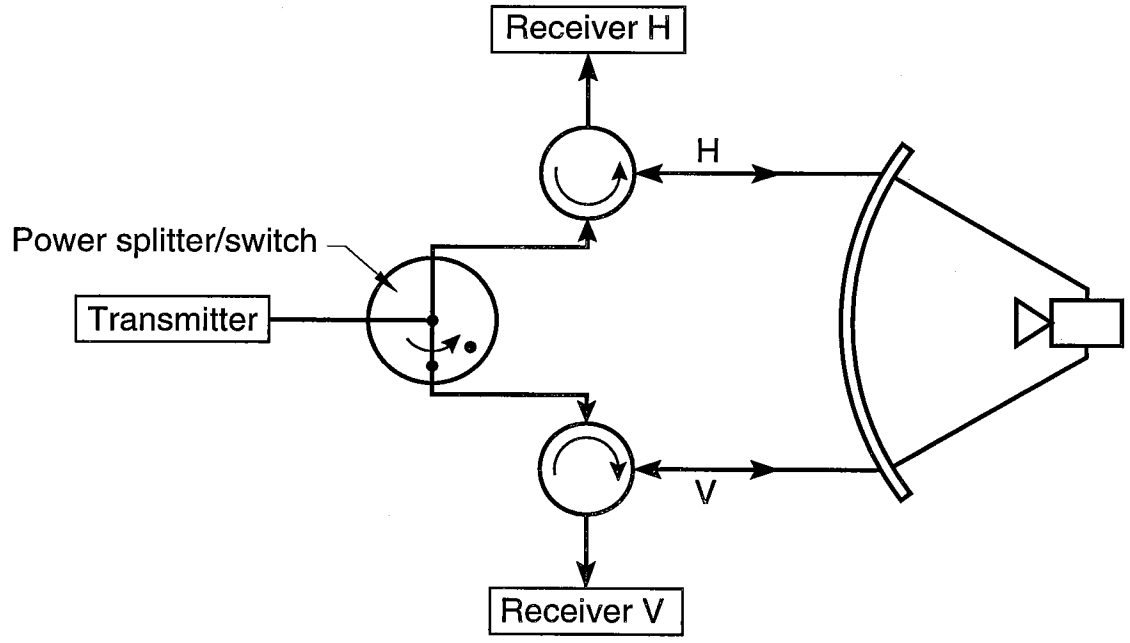

Fig. III.7 A simplified block diagram illustrating the flexibility of NSSL's research and development WSR-88D to switch from simultaneous transmissions and receptions of H, V polarized waves to transmission of horizontally polarized waves (i.e., the WSR-88D operational mode).

Testing of the microwave circuits and analog receiver circuits will be made in two phases which are presented in Fig. III.8. In the first phase, the existing receiver will be connected to either the horizontal or vertical ports. Thus, engineering tests of the two (H, V) channels can be made. Moreover, statistical analysis of co-polar and cross-polar data will be made to test isolation and effects of propagation.

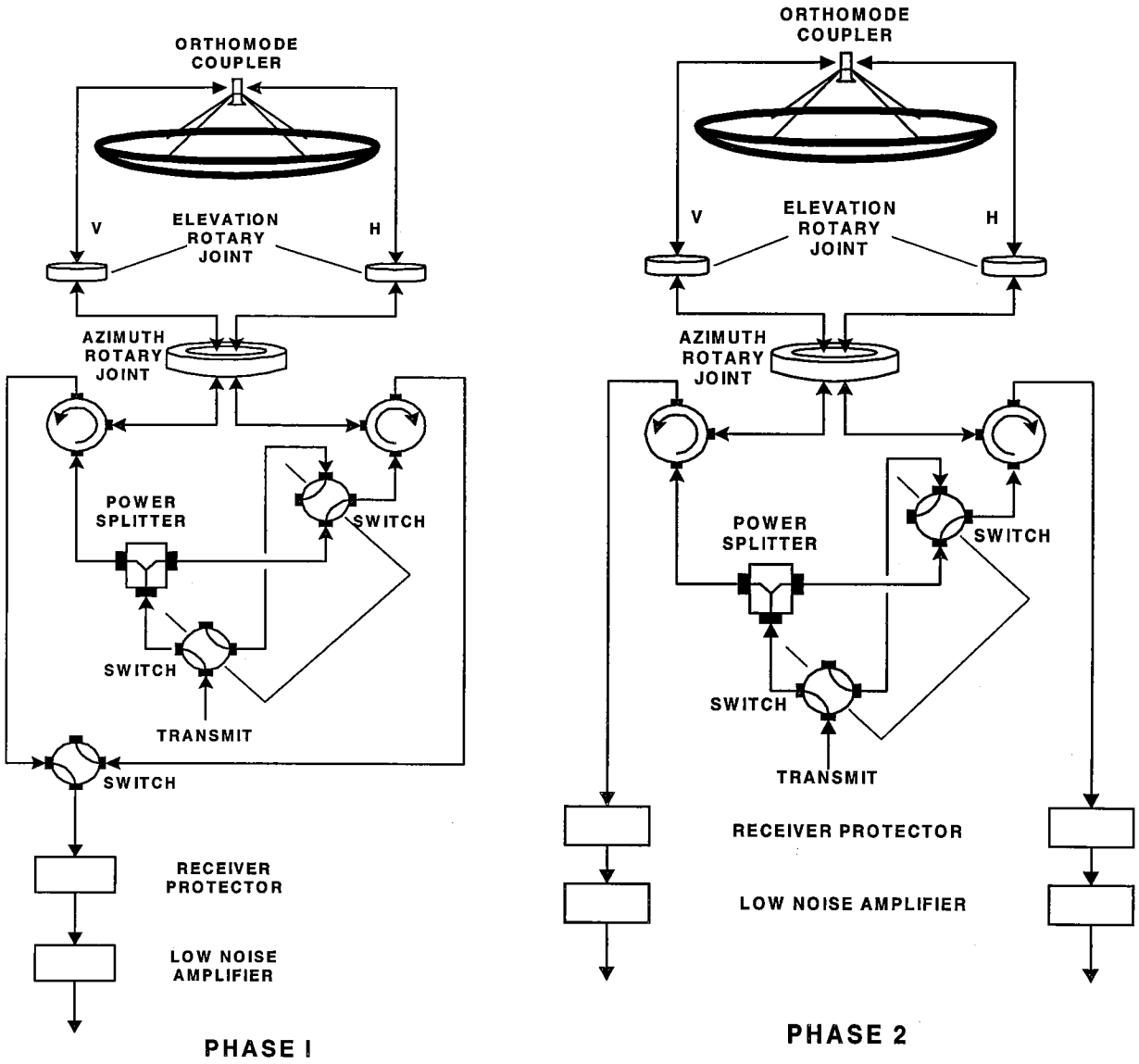

Fig. III.8 A detailed schematic of the microwave components of NSSL's research and development WSR-88D polarimetric radar.

In the second phase, two receivers will be incorporated into the system. In this configuration, we will be able to transmit and receiver H, V polarized signals simultaneously. In addition, with two receivers, it will also be possible to obtain Z_h, *Ldr*, the one-way differential phase (i.e., $\phi_{DP}/2$), and spectral moments in a mode whereby only H is transmitted, and both H and V are received. This will allow us to access the utility of *Ldr* and help decide if such a mode should be considered for the WSR-88D network. Besides engineering tests, a comparison with polarimetric data collected by the Cimarron radar, which has a high-power high-speed switch, will be made. A brief description of the reasons for our decision follows.

III.3. Relative merits of simultaneous vs. alternate transmissions of H, V waves

Assuming no propagation effects, we contrast simultaneous transmission/reception with alternate transmission/reception. The decision to test the mode of simultaneously transmitting and receiving H, V waves is rooted in several benefits compared to the mode of alternating the transmission and reception of H, V waves. The benefits of the simultaneous mode are

i) The correlation $|\rho_{hv}(0)|$ between H and V weather signals at zero lag can be measured directly (i.e., there is no need to assume a correlation model, nor is there any need to perform the time consuming spectral calculations if a model is not assumed; Section III.3.1).

ii) The differential phase shift ϕ_{DP} can be measured directly (i.e., no need to account for Doppler shifts; Section III.3.1).

iii) There are no compromises in the performance of the ground clutter filter (Section III.3.2).

iv) There are less errors in polarimetric variables for the same scan rates (Section III.3.3).

v) There is no need for a costly (>$100 K) high-power ferrite switch.

Alternate transmission of H, V waves has the following benefits:

i) Automatic suppression of overlaid echoes from even trip (2nd, 4th, ...) reflectivities.

ii) The depolarization ratio can be measured (Section III.3.5).

iii) There is no need to have a second receiver. (This also eliminates the need for matching the two receivers.)

Ryzhkov and Zrnic (1998) made a theoretical comparison of the errors in estimating the polarimetric variable ϕ_{DP} for H,V waves alternately transmitted and received (as copolar signals) with a mode in which H, V waves are simultaneously transmitted. They concluded that the

simultaneous transmission of H, V waves provides a better accuracy than alternately transmitted H, V waves for measurement of ϕ_{DP} (Section III.3.3). Furthermore, the advantages of simultaneous transmission are more pronouced if the Doppler spectrum widths, normalized to the typical unambiguous velocity of the WSR-88D radars, are larger than 0.1, values which are typically encountered in severe storms.

The benefits of simultaneous transmission are considered to outweigh the benefits of alternate transmission. Chapter IV analyzes some of the possible biases in polarimetric variables if H, V polarized waves are simultaneously transmitted. Next, we offer a more detailed explanation of the various advantages and disadvantages.

III.3.1 Measurements of the cross correlation $|\rho_{hv}(0)|$ and differential phase ϕ_{DP}

A favorable feature of simultaneous transmission and reception of H, V waves is that the cross correlation coefficient and differential phase are obtained directly without the need to estimate or eliminate the effects of the phase shift due to the Doppler velocity.

To estimate rapidly the $|\rho_{hv}(0)|$ in alternate transmission, the shape of the spectrum is assumed to have a Gaussian form, and correlations are evaluated at lags 0, 1, and 2 (Balakrishnan and Zrnic 1990; Zahrai and Zrnic 1993). If the assumption of a Gaussian shape is dropped, $|\rho_{hv}(0)|$ can still be estimated, but time consuming spectral analysis and interpolation is required (Zrnic et al. 1994).

In the alternate transmission and reception mode, the differential phase ϕ_{DP} and normalized Doppler shift Ψ_d ($=\pi v/v_a$) are coupled (Sachidananda and Zrnic 1989; Zahrai and Zrnic 1993; Doviak and Zrnic 1993). Although the uncoupling of ϕ_{DP} and Ψ_d is straightforward, it introduces an added complexity. Namely, elimination of Ψ_d from the equations reduces the periodicity of the phase $2\phi_{DP}$ to a 360° interval and, therefore, the phase ϕ_{DP} to a 180° interval. In practice, the bottom of this interval would be placed slightly below the differential phase of the radar system to allow for statistical uncertainty and because the phase through most precipitation increases. In cases where the differential phase due to precipitation is more than 180°, aliasing of ϕ_{DP} would occur. Nevertheless, this aliasing can be corrected by examining the continuity of ϕ_{DP}. But wherever ϕ_{DP} aliases, there would be a velocity shift (pseudo alias) by $-v_a$ which also needs to be corrected. With simultaneous transmission, the ϕ_{DP} aliases over a 360° interval, and it is not coupled to the Doppler velocity.

III.3.2 Ground clutter filtering

A clear advantage of the simultaneous transmission is the uncompromised filtering of the ground clutter. That is, the ground clutter filter of the existing WSR-88D can be applied without modifications. This is not so for the mode of alternating transmission and reception. In the alternate sequence HVHV..., the identically polarized echoes need to be separately filtered; otherwise, echoes at orthogonal polarizations would be added by the filter, and the information

specific to polarization would be lost. Because samples of likewise polarization are spaced by $2T_s$, the filter's notch (in the Doppler velocity domain) would repeat at intervals equal to the unambiguous velocity $v_a = \lambda/4T_s$; this is in contrast to the repetition of notches at $2v_a$ that is currently implemented in the WSR-88D (Fig. III.9).

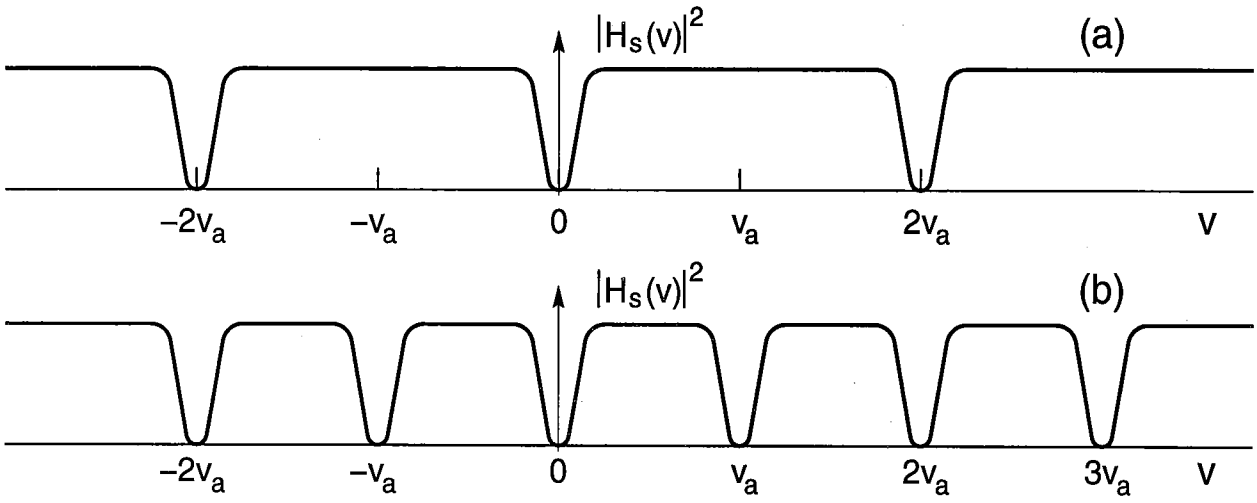

Fig. III.9 Position of the ground clutter filter notches in (a) the current WSR-88D configuration which transmits singly polarized H waves, as well as the mode for simultaneous transmission and reception of H, V waves, and (b) the configuration in which H, V waves are alternately transmitted or received.

III.3.3 Standard error of estimates

The standard errors of estimates with simultaneous and alternate transmissions (receptions) differ. Generally, these are smaller for simultaneous transmission. Because the crucial polarimetric variable is the propagation differential phase, its errors will be compared for the two schemes. The variance of ϕ_{DP} for simultaneous transmission can be shown to be (Ryzhkov and Zrnic 1998)

$$VAR(\phi_{DP}) = \frac{1-|\rho_{hv}(0)|^2}{2M^2|\rho_{hv}(0)|^2} \sum_{m=M-1}^{M-1} (M-|m|)\,|\rho^2(m)| \qquad (radians)^2, \qquad \text{(III.42)}$$

where $|\rho_{hv}(0)|^2$ designates the magnitude squared of the correlation coefficient between horizontally and vertically polarized echoes at zero lag, $|\rho(m)|$ is the magnitude of the correlation coefficient between like polarized echoes (i.e., ρ_{hh} or ρ_{vv}) at lag mT_s, and M is the number of simultaneous pairs which equals the number of transmitted pulses.

For alternate transmission, a similar formula can be derived (Sachidananda and Zrnic 1986):

$$VAR(\phi_{DP}) = \frac{1-|\rho_{hv}(0)|^2|\rho(1)|^2}{4L^2|\rho_{hv}(0)|^2} \sum_{m=L-1}^{L-1} (L-|m|)|\rho(2m)|^2 - \frac{|\rho_{hv}(0)|^2-|\rho(1)|^2}{4L^2|\rho_{hv}(0)|^2} \sum_{m=L-1}^{L-1} (L-|m|)|\rho(2m+1)|^2 \quad (radian)^2, \tag{III.43}$$

where L is the number of H,V pairs (i.e., M/2). Note that for the same dwell time (MT_s), there are twice as many pairs of H,V echoes in simultaneous transmission as there are in alternate transmission. The plot (Fig. III.10) of the standard deviations corresponding to the two formulas illustrates the difference between the two. For narrow spectra (relative to the unambiguous Doppler velocity interval) and the same dwell times, the two schemes are equivalent; samples are highly correlated, and the errors primarily depend on the dwell time. At larger spectrum widths, the alternate scheme is clearly inferior; a sharp increase in the error is observed at a normalized spectral width $\sigma_{vn} \equiv \sigma_v/2v_a$ of about 0.12. This is where the decorrelation of samples degrades the estimates, and such a condition is clearly absent for simultaneous transmission whereby H and V echoes are tightly correlated.

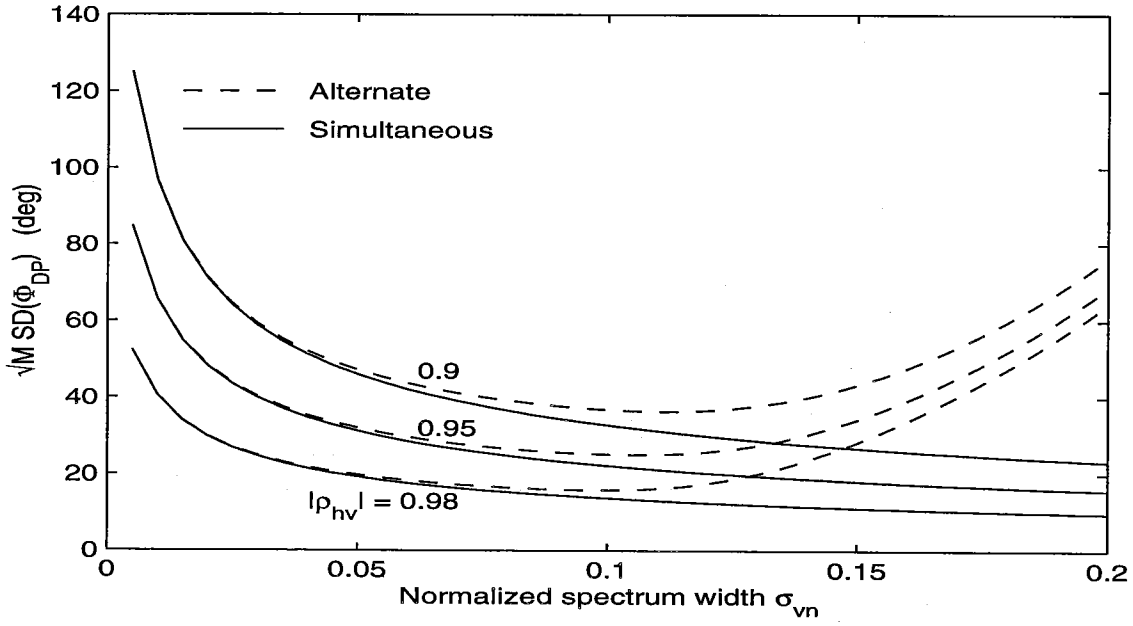

Fig. III.10 Standard deviation of the differential phase estimates for alternate and simultaneous transmission schemes.

III.3.4 Sensitivity

With alternate transmission, all the power is in one polarization, and the loss in sensitivity is mainly confined to twice the loss in the switch. In case of the high-power ferrite switch, the sensitivity could be 3 to 4 dB lower. For a mechanical switch, the loss is negligible. There might be differences between H and V signals due to propagation through and scatter from heavy precipitation or other nonspherical scatterers whereby the sensitivity at vertical polarization could be lower.

With simultaneous transmission, the total transmitted power would be the same as in the current system, but upon reception and partition into two channels, the signal to noise ratios in each receiver would be 3 dB lower. If the signal power from a resolution volume is denoted by S and the receiver noise by N, it follows that the signal to noise ratio for simultaneous transmission would be

$$\mathrm{SNR}_s = S/(2N)\ . \tag{III.44}$$

This assumes that the losses and receiver noises per channel in the dual polarization system are equal to the ones in the current system.

For Doppler velocity measurements, the effective loss in SNR is less; the forthcoming discussion gives the reason. First, a measure of the quality of Doppler velocity estimates is its variance which, at low SNR, can be approximated with

$$\mathrm{VAR}[v] \approx (N/S)^2/M, \tag{III.45}$$

where M is the number of sample pairs (Doviak and Zrnic 1993). For simultaneous transmission, the variance of the velocity estimate in one channel (receiver) is

$$\mathrm{VAR}[v_1] \approx (2N/S)^2/M \tag{III.46}$$

Because there are two receivers, one can combine the velocity estimates. Assuming that the noises of the two receivers are not correlated, the variance of the average velocity (from the two receivers) is

$$\mathrm{VAR}[(v_1 + v_2)/2] \approx \ 2(N/S)^2/M. \tag{III.47}$$

Examination of (III.47) reveals that, for considerations of the Doppler variance increase, the effective reduction in SNR is by $\sqrt{2}$ or 1.5 dB.

The WSR-88D uses SNR thresholds on data prior to display and further manipulations. The default thresholds are 3.5 dB in the storm mode and 0.5 or 1 dB in clear air (long pulse or short pulse). The range of SNR thresholds is from -12 to 20 dB. Thus, depending on the choice of a threshold, the effective reduction of velocity variance will correspond to a decrease in SNR of, at

most, 1.5 dB (i.e., at the -12 dB SNR threshold). At higher SNR thresholds, the effective loss in SNR would be smaller.

III.3.5 Correlation coefficient and Linear Depolarization Ratio

The proposed hardware for simultaneous transmission and reception of H and V polarizations (Fig. III.8, phase 2) cannot provide the linear depolarization ratio, *Ldr*. But, as stated earlier, this parameter is not easy to estimate because it is computed from a typically weak signal which is more easily corrupted by receiver noise. Furthermore, *Ldr* has not proven to be a robust parameter to quantify the properties of precipitation. Moreover, it is affected by differential attenuation, whereas $|\rho_{hv}(0)|$ is not (Section III.1.3). Finally, for some hydrometeor configurations, *Ldr* is highly correlated with $|\rho_{hv}(0)|$ and thus carries very little added information. Here, we comment on the similarity and differences between *Ldr* and $|\rho_{hv}(0)|$.

For completely random orientation of scatterers, the variables *Ldr* and $|\rho_{hv}(0)|$ are related by

$$1 - |\rho_{hv}(0)| = 2Ldr\,. \tag{III.48}$$

This relation can be obtained by inserting (III.13), (III.16), and (III.18) into the definitions of these two variables; i.e.,

$$Ldr \equiv \frac{<|s_{hv}|^2>}{<|s_{hh}|^2>}, \tag{III.49}$$

and

$$|\rho_{hv}(0)| \equiv \frac{|<s_{hh}s_{vv}^*>|}{\left(<|s_{hh}|^2><|s_{vv}|^2>\right)^{1/2}}, \tag{III.50}$$

and noting that, for completely random orientation, the degree of alignment r = 0, and $<|s_{hh}|^2> = <|s_{vv}|^2>$. That is, the reflectivity is not a function of the direction of the incident electric field. An alternate derivation could start with the equations (8.58a to c) of Doviak and Zrnic (1993), followed by an integration over the uniform distribution of canting angles ψ and the angle δ between propagation direction and incident field.

To summarize, for the detection of randomly oriented hail (or any other randomly oriented scatterers), the two variables should perform equally well. But for other configurations, there are differences. For example, if all the hydrometeors have zero canting angle (i.e., $\psi = 0$, and thus, r = 1), then *Ldr* = 0, and $|\rho_{hv}(0)|$ can be computed using (III.13), (III.14), and (III.17); it would depend on the distribution of shapes (i.e., on ν). Sachidananda and Zrnic (1985) have modeled the distribution of shapes for water drops including the effects of shape oscillations. They find

that $|\rho_{hv}(0)|^2$ is larger than about 0.99 for rain rates R up to 200 mm h^{-1}, and if drops do not oscillate, $|\rho_{hv}(0)|^2$ is larger than 0.999, even for R = 200 mm h^{-1}. Thus, *Ldr* and $|\rho_{hv}(0)|$ remain closely related; the main difference is that *Ldr* strongly depends on the mean canting angle (if the degree of common alignment is high; i.e., $r = 1$), whereas $|\rho_{hv}(0)|$ does not. The most significant difference between the two is that *Ldr* is biased by differential attenuation (III.24).

Finally, the significance of not having *Ldr* data diminishes in the presence of other polarimetric variables. Nonetheless, one can conceive of unlikely hydrometeor arrangements that are ambiguous with respect to all other polarimetric variables except *Ldr* . For illustration, take a hypothetical values of $Z_{dr} = 1$ and $|\rho_{hv}(0)| = 1$. Without other information, one would expect that spherical hydrometeors are the likely cause of these values. If *Ldr* were 0, one would be hard pressed to come up with alternate shapes and orientations that could replicate the result. But if *Ldr* was measured to be ≈ 1, then strongly oblate spheroidal hydrometeors of the same size, but with fixed canting angles of 45°, would explain the measurement. On the other hand, measurements of *Ldr* so far have rarely given values larger than about 0.05 (i.e., LDR < -13 dB; Bringi, private communication). Further research, coupled with experiments, is needed to properly evaluate the loss of information due to the absence of *Ldr* measurement.

IV. EFFECTS OF FEED MISALIGNMENT, DROP CANTING, AND BACKSCATTER DEPOLARIZATION ON POLARIMETRIC MEASUREMENTS USING SIMULTANEOUS TRANSMISSION OF H, V WAVES

Radar measurements of hydrometeors' intrinsic polarimetric parameters (e.g., differential reflectivity, specific differential phase, and the coefficient of correlation between horizontally and vertically polarized waves within a resolution volume) usually involve unwanted coupling between the two states of polarization (e.g., horizontally H and vertically V polarized waves). This coupling can be caused by misalignment of the dual port feed and/or canting of the raindrop's axis of symmetry which can create errors in the parameter estimates. Coupling effects could be significant if H, V waves are simultaneously transmitted and received. For example, Sachidananda and Zrnic (1985) show that bias errors in differential reflectivity can be an order of magnitude larger if estimates are made using H, V polarized waves that are simultaneously transmitted and received rather than alternately transmitted and received. The purpose of this section is to extend this study to other polarimetric parameters and to determine the practical bounds on parameter estimation errors caused by effects such as canting angle dispersion, feed misalignment, and backscatter depolarization. Toward this goal, we consider separately the effects of feed misalignment, drop canting along the propagation path, and depolarization upon backscattering.

IV.1. Feed misalignment

Here, we consider a dual-port feed that can radiate and receive waves that are either horizontally or vertically polarized if the feed is properly oriented. One port, called the H′ port, is assumed to generate and receive linearly polarized waves which are nominally horizontal; likewise, the V′ port generates and receives nominally vertically polarized waves. The primes are used to differentiate the directions H′, V′, which are rotated by α degrees, the angular displacement of the feed about its axis, from the exactly horizontal H and vertical V directions (Fig. IV.1). The H′ and V′ polarized waves are assumed to be (1) simultaneously transmitted, (2) orthogonal to each other, (3) of equal magnitudes, and (4) have a phase difference β (i.e. $E_{v'} = E_{h'} e^{j\beta}$). Although the antenna generates equal $E_{h'}$, $E_{v'}$, the wave amplitudes in the H, V directions are not necessarily equal if $\alpha \neq 0$ (Fig. IV.1). Thus, the transmitted wave's polarization is perfectly linear if $\beta = 0$, perfectly circular (right or left handed) if $\beta = \pm\pi/2$, or elliptical for any other β; but the tilt angle τ of the polarization ellipse (Fig. A.1 of Section II) will always be $\pi/4$ (calculated from (A.4)) plus α relative to the H axis. In practice, the radar must be calibrated so that in the absence of propagation effects (e.g. differential attenuation), the voltages $V_{h'}$, $V_{v'}$ in the H′ and V′ channels of the receiver contributed by a spherical scatterer are identical. Such calibration is needed to insure that Z_{dr} estimates are not biased. Observations with a vertically pointed beam are ideally suited for this calibration because drops, whether spherical or not, have their axes of symmetry directed nearly along the vertical (i.e., the canting angles are small; Section IV.2).

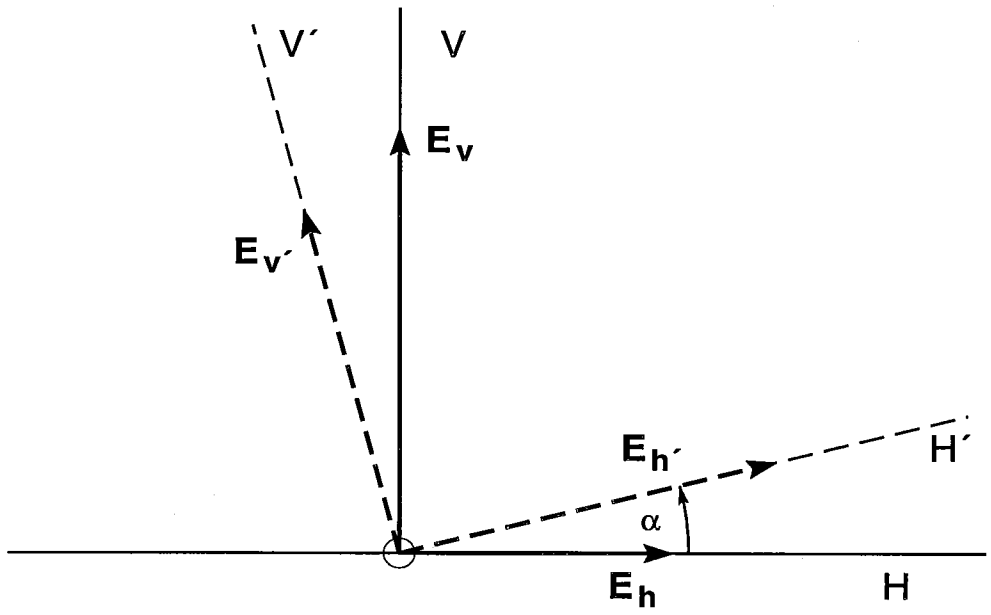

Fig IV.1: The H´, V´ coordinate system in which the transmitted wave amplitudes $E_{h'}$, $E_{v'}$ are equal, but which is rotated by α degrees from the horizontal H and vertical V directions.

In this section, the effects of feed rotation on the estimation of polarimetric parameters are presented. For sake of simplicity, assume that a differential transmission matrix $\boldsymbol{T}$ is given by

$$\boldsymbol{T} = \begin{bmatrix} \exp(-j\phi_{DP}/2) & 0 \\ 0 & 1 \end{bmatrix}, \qquad \text{(IV.1)}$$

where ϕ_{DP} is the two-way intrinsic differential phase shift for the condition of zero canting angle. In (IV.1), differential attenuation is ignored, and it is assumed that there is no coupling between the horizontally and vertically polarized fields as they propagate through precipitation. (This latter effect is discussed in Section IV.2.) The primary reason these assumptions are made is to isolate completely the effects of feed misalignment from all other effects.

For the same reason, we assume there is insignificant phase shift upon backscatter (i.e., $\delta_{hh} = \delta_{vv} = 0$, where δ_{hh} and δ_{vv} are the backscatter phase shifts for H and V waves (Doviak and Zrnic 1993), and that drops are of the same size and are not canted within the sampled resolution

volume. (The effect of depolarization upon backscatter is discussed in Section IV.3.) Thus, the backscatter matrix $\boldsymbol{S}$ for each drop is

$$\boldsymbol{S} = \begin{bmatrix} s_{hh} & 0 \\ 0 & s_{vv} \end{bmatrix}, \tag{IV.2}$$

and the intrinsic differential reflectivity is (Doviak and Zrnic 1993, Eq. 8.46c)

$$Z_{dr} \equiv \frac{<|s_{hh}|^2>}{<|s_{vv}|^2>} = \frac{s_{hh}^2}{s_{vv}^2}, \tag{IV.3}$$

where s_{hh} and s_{vv} are real backscatter coefficients for horizontally and vertically polarized waves. The lower case subscripts of Z_{dr} in (IV.3) and throughout this section indicate the voltage ratio as opposed to uppercase subscripts (DR) that indicate values in dB. The brackets indicate an ensemble average or expectation operation. Because all drops are of the same size and shape, the $V_{h'}$, $V_{v'}$ signal fluctuations, due to random differential motions of the scatterers in the sampled resolution volume, are perfectly correlated. Otherwise, terms such as $<s_{hh}\, s_{vv}>$ would appear in the final expressions requiring introduction of the zero lag correlation parameter $\rho_{hv}(0)$ which, for rain media, is practically 1. If $\boldsymbol{V}'$ and $\boldsymbol{E}'$ are column vector representations of the signals $V_{h'}$, $V_{v'}$ in the receiver and the transmitted fields $E_{h'}$, $E_{v'}$ at the antenna, it can be shown that $\boldsymbol{V}'$ and $\boldsymbol{E}'$ are related via

$$\boldsymbol{V}' = \boldsymbol{A}\cdot\boldsymbol{R}^t\cdot\boldsymbol{T}^t\cdot\boldsymbol{S}\cdot\boldsymbol{T}\cdot\boldsymbol{R}\cdot\boldsymbol{E}', \tag{IV.4}$$

where the dots indicate multiplication, the receiver transfer matrix $\boldsymbol{A}$ is

$$\boldsymbol{A} = \begin{bmatrix} e^{j\gamma} & 0 \\ 0 & 1 \end{bmatrix}, \tag{IV.5}$$

and the rotation matrix $\boldsymbol{R}$ is

$$\boldsymbol{R} = \begin{bmatrix} \cos\alpha & -\sin\alpha \\ \sin\alpha & \cos\alpha \end{bmatrix}. \tag{IV.6}$$

Here, the matrix $\boldsymbol{R}$ is used in place of an otherwise general matrix commonly used to characterize the polarization properties of the dual-port feed. The specific form (IV.6) implies that the coupling between the H and V fields is simply caused by rotation of an otherwise perfect feed (i.e., one without coupling between the H and V ports). The receiver transfer matrix implies no coupling between channels and equal gains, but a phase difference of γ. The superscript t denotes the matrix transpose. We have ignored the changes of signals with range, attenuation, and

proportionality constants which make (IV.4) dimensionally correct. We also assume H, V radiation patterns are matched and that there is negligible coupling between the H and V ports of the antenna. (Typically, the coupling is less than -30 dB.) Effects of pattern mismatch, both in amplitude and phase, and coupling are discussed by Chandrasekar and Keeler (1993).

IV.1.1 Effects of misalignment on differential reflectivity measurements

The measured differential reflectivity can be expressed as the ratio

$$Z_{drm} = \frac{<|V_{h'}|^2>}{<|V_{v'}|^2>}. \tag{IV.7}$$

Solving for $V_{h'}$, $V_{v'}$ from (IV.4) and inserting it into (IV.7) produces the following:

$$Z_{drm} = \frac{|s_{hh}e^{-j\phi_{DP}}\cos^2\alpha + s_{vv}\sin^2\alpha - (s_{hh}e^{-j\phi_{DP}} - s_{vv})e^{j\beta}\sin\alpha\cos\alpha|^2}{|s_{hh}e^{j(\beta-\phi_{DP})}\sin^2\alpha + s_{vv}e^{j\beta}\cos^2\alpha - (s_{hh}e^{-j\phi_{DP}} - s_{vv})\sin\alpha\cos\alpha|^2}. \tag{IV.8}$$

Because drops within the sampled resolution volume are of the same size and shape, the expectation operation does not appear in (IV.8). Only the portion $E_v\sin\alpha$ of the vertically polarized wave is added to the horizontally polarized wave, and hence, only the phase of this portion is differentially shifted by propagation. Thus, the phase difference β between the H′ and V′ waves at the transmitter does not simply add to the differential phase due to propagation.

The intrinsic (true) differential reflectivity Z_{DR} (dB scale) is given by (IV.3), and it is used in place of s_{hh}, s_{vv} in (IV.8) to obtain the Z_{DR} bias, ΔZ_{DR}, from

$$Z_{DRm} = Z_{DR} + \Delta Z_{DR}. \tag{IV.9}$$

This bias is given by

$$\Delta Z_{DR} = 10\log_{10}\left[\frac{|e^{-j\phi_{DP}}(\cos^2\alpha - e^{j\beta}\sin\alpha\cos\alpha) + (\sin^2\alpha + e^{j\beta}\sin\alpha\cos\alpha)(Z_{dr})^{-1/2}|^2}{|e^{-j\phi_{DP}}(e^{j\beta}\sin^2\alpha - \sin\alpha\cos\alpha)(Z_{dr})^{1/2} + e^{j\beta}\cos^2\alpha + \sin\alpha\cos\alpha|^2}\right], \tag{IV.10}$$

and it is plotted in Fig. IV.2 for an intrinsic value of $Z_{DR} = 3$ dB and $\alpha = 0.1°$ for various values of β (measurements reported in Section II.6.4 indicate that $\alpha < 0.1°$). It is noteworthy that the bias is periodic in ϕ_{DP} and has a maximum of 0.062 dB at 180° of differential phase shift if $\beta = 180°$. Furthermore, if ϕ_{DP} is uniformly distributed over 2π, the differential reflectivity bias is zero, on average, if circularly polarized waves (i.e., $\beta = 90°$) are transmitted.

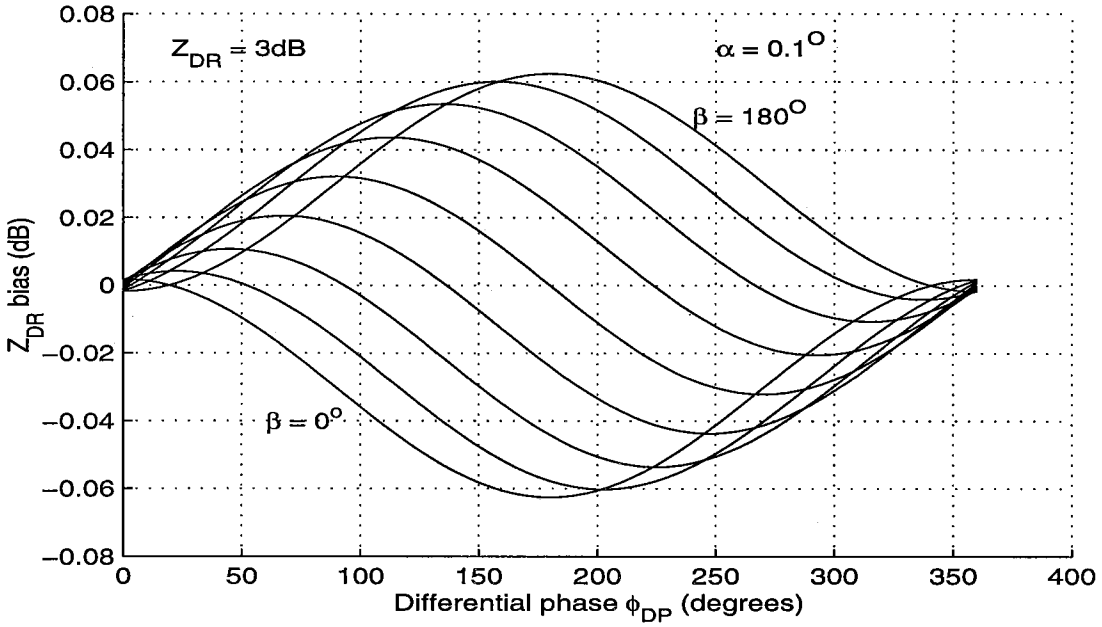

Fig. IV.2 The differential reflectivity bias (in dB) versus round trip differential phase shift, for various values of the differential phase shift β (in steps of 22.5°) upon transmission. The intrinsic differential reflectivity Z_{DR} is assumed to be 3 dB, and the feed misalignment α = 0.1°.

It can be shown that for small α (as expected in the installed dual-port feed), the bias error is proportional to α; a 1 degree misalignment results in 0.62 dB of bias error. But such large errors in feed alignment are not expected. Furthermore, with differential phase shifts as large as 180 degrees, there would be significant differential attenuation which needs to be accounted for. For example, Bringi et al. (1990) compute a differential attenuation of about 0.6 dB for a 180° differential phase shift in rain, and Ryzhkov and Zrnic (1995) observed differential attenuation of about 1.6 dB along a path with 180° of differential phase. Thus, natural effects would usually cause larger biases in differential reflectivity than feed misalignment.

In summary, although there is differential reflectivity bias due to rotation of the feed about its axis, this bias could be made negligible if the angular displacement α of the feed is kept below a few tenths of a degree. Larger tilts of the feed might be tolerated, however, because at large differential phase shifts, the effects of misalignment would be masked by other effects (e.g., differential attenuation). Nevertheless, it would be safer if rotation of the feed from its intended position is less than about 0.1° - 0.2°.

IV.1.2 Effects of misalignment on differential phase measurements

The measured ϕ_{DPm} is defined as (Doviak and Zrnic 1993, Eq. 8.46f)

$$\phi_{DPm} = arg(V_{h'}^{*} V_{v'}), \tag{IV.11}$$

where * indicates a complex conjugation. Because $V_{h'}, V_{v'}$ are perfectly correlated under assumptions given in Section IV.1.1, ϕ_{DPm} for the ensemble of scatters is identical to that for a single scatterer. Therefore, it can be easily shown that if $\alpha = 0$,

$$\phi_{DPm} = \beta - \gamma + \phi_{DP}, \tag{IV.12}$$

where ϕ_{DP} is the intrinsic (true) differential phase, and $\beta - \gamma$ is the contribution to the measured differential phase caused by differential phase shifts in the transmitter and receiver.

The differential phase bias is defined as $\Delta\phi_{DP} \equiv \phi_{DPm} - \phi_{DP}$. Using (IV.4) to calculate $V_{h'}, V_{v'}$, for the case $\alpha \neq 0$, and substituting the results of this calculation into (IV.11), the following equation is obtained:

$$\Delta\phi_{DP} = -\gamma + arg(p), \tag{IV.13}$$

where

$$\begin{aligned} p = {} & \sqrt{Z_{dr}} e^{+j\beta}(\cos^4\alpha + e^{-j2\phi_{DP}}\sin^4\alpha) - \sqrt{Z_{dr}} e^{-j\beta}\sin^2\alpha\cos^2\alpha(1 + e^{-2j\phi_{DP}}) \\ & + e^{-j\phi_{DP}}\sin\alpha\cos\alpha[(1 - Z_{dr}) + 2(1 + Z_{dr})\sin\alpha\cos\alpha\cos\beta]. \end{aligned} \tag{IV.14}$$

In Fig. IV.3 is the plot of (IV.13) as a function of ϕ_{DP} for $\alpha = 1°$, $\gamma = 0°$, $Z_{dr} = 1$, and $\beta = 40°$. From (IV.13) it is obvious that γ simply adds a fixed bias to the measured differential phase, but it can be removed in the calibration of the radar. It can be shown that the oscillatory excursion, around the mean value of about β, is almost the same for all values of β. But for all practical purposes, this mean bias is not significant because the parameter of interest is the range gradient of ϕ_{DP} (i.e., the specific differential phase K_{DP} which relates to rainfall rate). Therefore, the slope of the bias error is more important because this biases the measurements of K_{DP} and, hence, rainrates. It can be shown, however, that the slope bias is also insignificant.

For example, for a heavy rain rate of 37 mm h^{-1} and a 10 cm wavelength radar, the one-way specific differential phase change is about 1° km^{-1} (Doviak and Zrnic 1993, Eq. 8.31a), the reflectivity factor computes to 48 dBZ if the Marshall-Palmer rainrate formula is used, and the

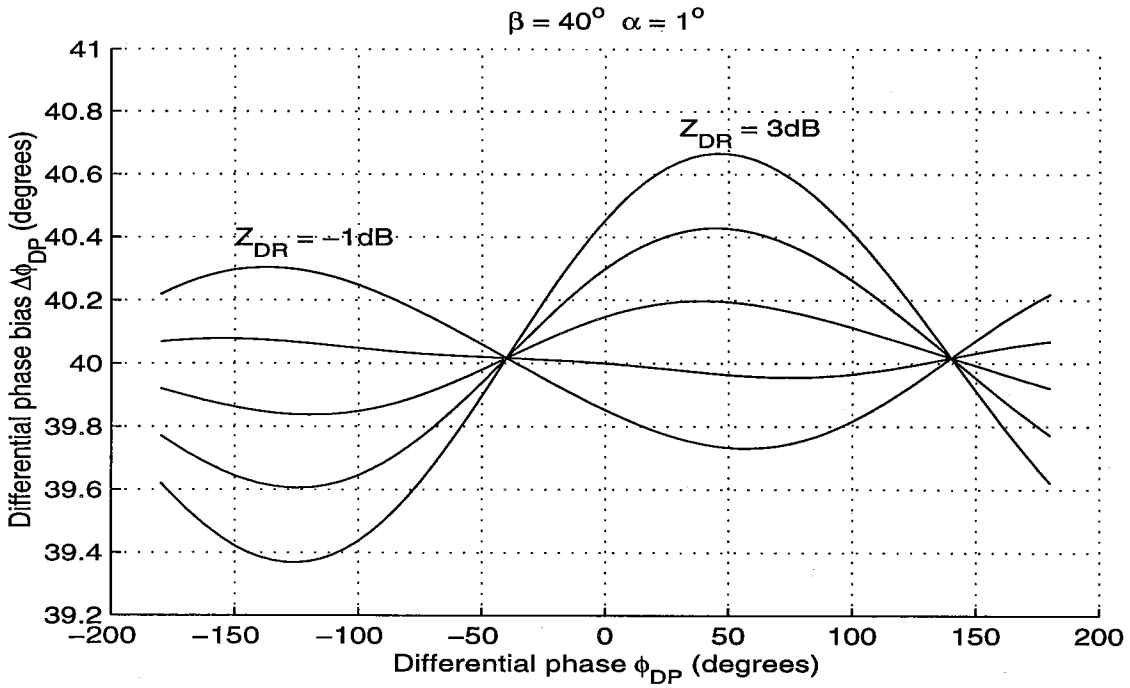

Fig. IV.3 The bias in differential phase measurements for a feed misalignment $\alpha = 1°$ and Z_{DR} ranging from -1 to +3 in steps of 1 dB. The differential phase shift γ within the receiver is assumed to be zero, and the differential phase upon transmission $\beta = 40°$.

differential reflectivity Z_{DR} = 2.2 dB (Doviak and Zrnic 1993, Eq. 8.67). From Fig. IV.3, we see the maximum slope of the differential phase bias occurs over the interval of differential phase from -100° to +25° which, for the cited rain rate, corresponds to a *one*-way path length of 62.5 km. The two-way differential phase bias over this path length is about 0.8°; thus, the specific differential phase bias (one-way) is less than 0.0064° km^{-1}. Hence, the bias in rain rate measurements is less than a few tenths of a mm h^{-1}; it will even be much smaller if the feed tilt is significantly less than 1°.

IV.1.3 Effects of misalignment on the correlation coefficient magnitude

The measured correlation coefficient magnitude can be written as

$$|\rho_{hvm}| = |\rho_{hv}| + \Delta\rho_{hv}, \qquad \text{(IV.15)}$$

where

$$\rho_{hvm} = \frac{<(V_{h'}V_{v'}^{*})>}{\sqrt{<(V_{h'}^{2})><(V_{v'}^{2})>}}. \qquad \text{(IV.16)}$$

Setting $A = R = I$, the identity matrix, in (IV.4), we can derive matrix relations to compute the bias. In this case, however, we assume the scatterers are still nonspherical but are statistically isotropic and may have a distribution of sizes. An example of such scatterers is tumbling hailstones that on average appear to be spherical and, thus, have $Z_{dr} \approx 1$, and yet ρ_{hv} can be significantly less than 1. The bias error $\Delta\rho_{hv}$ is plotted in Fig. IV.4 as a function of the two-way differential phase ϕ_{DP}, with β as a parameter varying from 0 to 180°. It is seen that the bias error is insignificant.

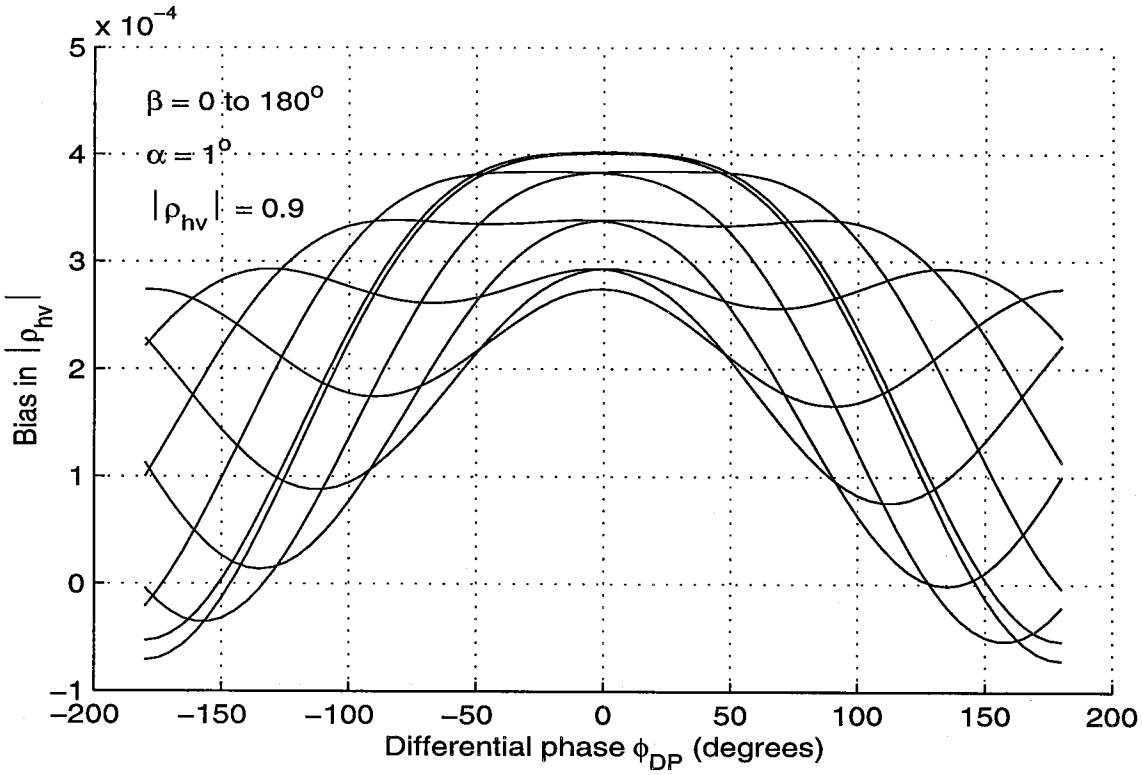

Fig. IV.4 The bias in the magnitude of the measured cross correlation $|\rho_{hvm}(0)|$ between the horizontally and vertically polarized echoes for various values of β in steps of 22.5°. Z_{DR} = 0 dB, $\gamma = 0$, $\alpha = 1°$, and $|\rho_{hv}(0)| = 0.9$.

IV.2. Canting of drops along propagation paths

Canting of raindrops occurs in regions of strong wind shear. Because strong wind shear in thunderstorms is confined to relatively small regions (compared to the propagation path length), and because the shear in these regions has (on the average) no preferential direction with respect to the direction to the radar, we expect the average canting angle (i.e., the average over the propagation path) to be zero.

Strong shear over large regions often can be found, however, near the ground. In such conditions, raindrops can experience persistent canting. Fig. IV.5 (from Brussard 1976) is the geometry of a canted raindrop; the drop is falling downward through a wind field which has a positive vertical shear (i.e., wind increasing with height; if there were a sufficiently strong updraft to move the drops upward through the wind shear region, the canting angle would be reversed). The mean orientation of the drop's axis of rotational symmetry is always parallel to the direction of airflow *relative to the drop* (Brussard 1976).

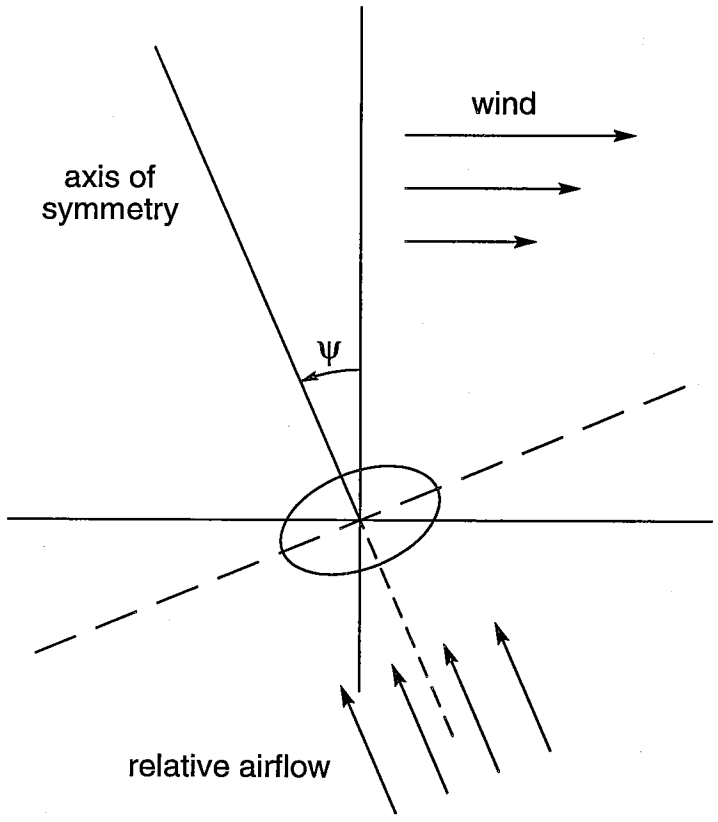

Fig. IV.5 The canting of an oblate spheroidal raindrop. Relative air flow is shown for a drop falling in air with positive vertical shear indicated by the horizontal directed arrows increasing in length with height.

Canting is not only caused by shear. If horizontal wind, spatially uniform over the region tranversed by the drop, is accelerating (due to turbulence, for example), there will be a relative flow in the direction of acceleration due to the inertia of the drop. Thus, the drop will cant and have its axis of symmetry parallel to the relative flow. The magnitude of the canting angle at any instant can be estimated by setting the drop's inertial force equal to the drag force and assuming that the drop accelerates at the same rate as the air, but its velocity lags that of the air by a constant amount. (This latter contention rests on the assumption that steady state is achieved in a negligibly short time.) Under these conditions, it can be shown that the canting angle is given by

$$\psi = \tan^{-1}\left(\sqrt{\frac{2ma}{\rho A C_d w_t^2}}\right), \qquad \text{(IV.17)}$$

where ρ is the density of air, m is the mass of the drop, a is the accerlation of air, A is the drop's cross sectional area in the plane perpendicular to the direction of relative flow, w_t is the drop's terminal velocity, and C_d is its drag coefficient.

Accelerating air is commonly associated with turbulence; hence, accelerations are spatially and temporally random with zero mean. Therefore, drops are momentarily canted one way and then another so that, on average, the canting angle induced by turbulence is zero.

If shear is present, there can be a prolonged average canting angle. Brussard (1976) demonstrates that the canting is strongest close to the ground where shear is usually the strongest; canting has been observed to be as much as 10° at 10 m, but with the much smaller value of 2° at about 80 m, where shear is weaker. For a linear wind profile with the horizontal wind u and vertical shear du/dz, the canting angle ψ, obtained from Brussard (1976), is

$$\tan\psi = \frac{(w_t - w)\,du/dz}{g}, \qquad \text{(IV.18)}$$

where $w_t - w$ is the fall speed of the drop, w_t is its terminal velocity, w is the vertical velocity of air, and g is the force of gravity. Given that 9 m s^{-1} is about the upper limit of the terminal velocity of the largest drops, and if $w = 0$ (as it would be near the ground), the canting angle is less then 0.6° for the extremely large shear of 0.01 s^{-1}. Whereas such large shear can occur in turbulent regions of severe storms, it would not be maintained over long distances, and shear direction is not homogeneous. That is, the canting angle would vary along the beam and would tend to average to zero. Furthermore, the radar beam is typically well above a hundred meters, and shear in rain above this altitude is rarely so persistent and strong. Nevertheless, in what follows, we make a quantitative analysis to establish what the worst effects would be.

To isolate the influence of canting from other effects, we assume (1) differential attenuation is negligible, (2) canting is confined to the plane of polarization (this is a worst case

because waves depolarize less for other canting directions), (3) $\alpha = 0$, (4) canting angle dispersion is negligible (dispersion is considered in Section IV.2.4), and (5) drops are of equal size and shape and are not canted in the sampled resolution volume.

IV.2.1 Effects of mean canting on Z and Z_{DR}

Sachidananda and Zrnic (1985) have computed the effects of canting angle ψ on the reflectivity factor and differential reflectivity under the assumption that all drops have equal ψ. For example, their Fig. 10 shows that if $\beta = 0°$ (i.e., linear polarization at 45°) and $Z_{DR} = 3$ dB, a maximum reflectivity bias occurs at $\phi_{DP} = 180°$, and this maximum is proportional to ψ. If $\psi = 5°$, the bias in reflectivity is -1.5 dB. The same conditions create a bias of -3 dB in their Z_{DR} plot (Fig. 11). Z_{dr} bias vs. ϕ_{DP} is plotted in Fig. IV.6 but with β as a parameter. Sachidananda and Zrnic (1985) define positive ψ as cw displacements of the drop's symmetry axis projected onto the plane of polarization; this is opposite to the definition used herein which follows that of Oguchi (1983). Thus, the sign of the Z_{dr} bias in their Fig. 11 is reversed from that shown in Fig. IV.6. Two other important facets distinquish our Fig. IV.6 from their Fig. 11: (1) Fig. IV.6 shows that the bias has a period of 720°, and (2) Fig. IV.6 shows that the bias is a function of β. The maximum bias shifts with β, but the excursion of bias values remains about the same.

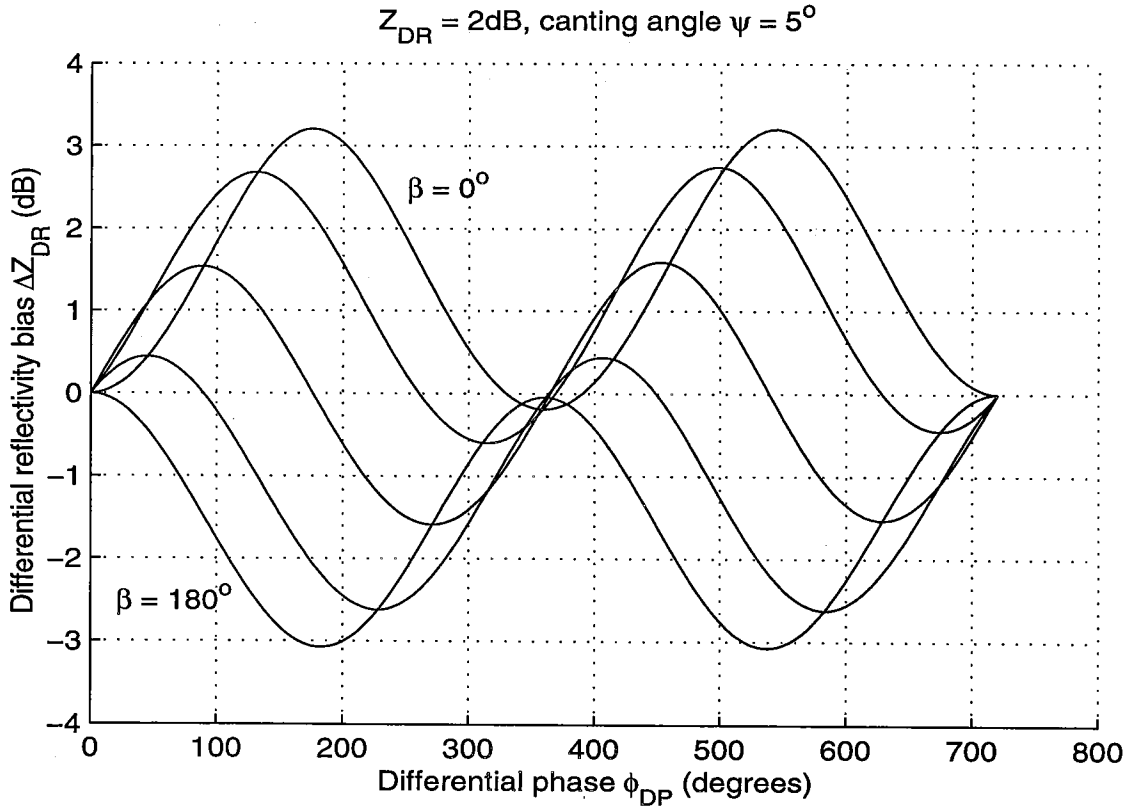

Fig. IV.6 The bias in Z_{DR} due to uniform canting $\psi = 5°$ along a propagation path vs. round trip differential phase ϕ_{DP} . $Z_{DR} = 2$ dB; $\alpha = 0°$.

Although the biases are exceptionally large for the 5° canting angle, canting angles are expected to be an order of magnitude less. It can be shown that the biases are roughly proportional to the canting angle. Thus, for the more realistic canting angle of 1°, the maximum bias in Z is about 0.2 dB, and the maximum bias in Z_{DR} is nearly 0.3 dB if $\phi_{DP} = 180°$. Although 180° of differential phase can be found in squall lines aligned with the radar's beam, it is improbable that uniform canting could be maintained along the entire length of the squall line. Furthermore, differential attenuation is significant for such a large differential phase, and this differential attenuation will strongly bias the differential reflectivity measurements. Furthermore, canting angle dispersion (not considered by Sachidananda and Zrnic 1985) should lessen the bias as shown in Section IV.2.4.

IV.2.2 Effects of mean canting on the differential phase

The normalized (i.e., common phase terms, radar constants, and common polarization and beam spreading losses are factored out) transmission matrix $\boldsymbol{T}$ elements can be obtained from Oguchi (1983), and they are

$$T_{hh} = e^{-j\phi_{DP}/2} + \tan^2\psi\,; \quad T_{hv} = (\tan\psi)\left(e^{-j\phi_{DP}/2} - 1\right); \quad T_{vv} = 1 + (\tan^2\psi)\, e^{-j\phi_{DP}/2}. \qquad \text{(IV.19)}$$

The total differential phase measured at the antenna is given by (IV.11), where now the elements of the voltage vector $\boldsymbol{V}$ are computed from

$$\boldsymbol{V} = \boldsymbol{A}\cdot\boldsymbol{T}^{t}\cdot\boldsymbol{S}\cdot\boldsymbol{T}\cdot\boldsymbol{E}\,. \qquad \text{(IV.20)}$$

As before, $|E_h| = |E_v|$ and the difference $\phi_{DPm} - \phi_{DP}$ is plotted in Fig. IV.7 for various values of Z_{dr}, the canting angle $\psi = 5°$, and $\beta = 0$. Note that again, the bias has a 4π period with respect to the intrinsic differential phase shift and has a maximum of about ±2° at ± 120°. As before, it is the range gradient biases which are of greatest concern. Using the parameters for the case of a 37 mm h^{-1} rain rate presented in Section IV.1.2 and selecting the largest gradient for $Z_{DR} = 2$ dB in Fig. IV.7, it can be deduced that there is as large as a 10% bias in rain rate (i.e., the rain rate would be underestimated by 10% for the region of total differential phase between 150° and 200°). But we have assumed an unusually large canting angle. It can be shown that the bias is roughly proportional to the canting angle for small angles. Thus, for the more realistic canting angle of 1°, the rain rate bias will be less than 2%, and therefore, from a practical view, canting should not significantly affect the specific differential phase measurements from which rain rate estimates are derived.

IV.2.3 Effects of mean canting on the correlation coefficient magnitude

The measured correlation $|\rho_{hvm}(0)|$ between H and V echoes is computed, as in Section IV.1.3, and results, for a canting angle of 5° and various phases β between the transmitted H and V waves, are plotted in Fig. IV.8. The bias depends on the magnitude of $\rho_{hv}(0)$ but is small. For $|\rho_{hv}(0)| = 0.9$, the bias in $|\rho_{hvm}(0)|$ is less than 1%; thus, it can be considered to be insignificant.

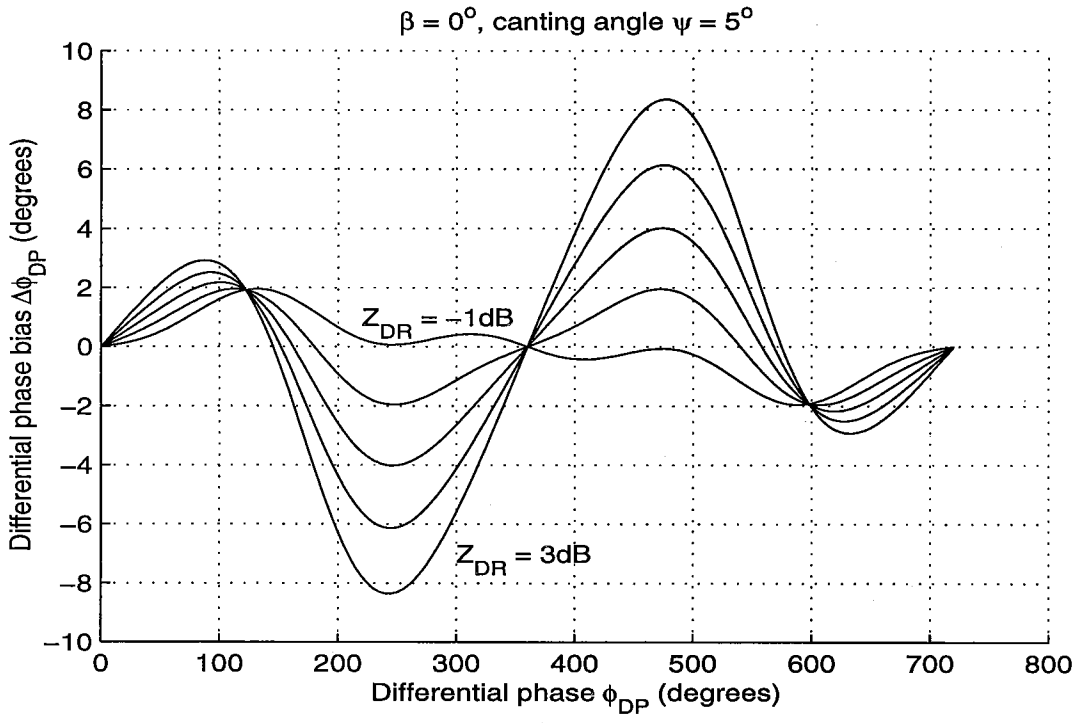

Fig. IV.7 The differential phase bias due to mean canting angle $\psi = 5^\circ$ along the propagation path. $Z_{DR} = 0$ dB in the sampled resolution volume, $\alpha = \beta = \gamma = 0^\circ$.

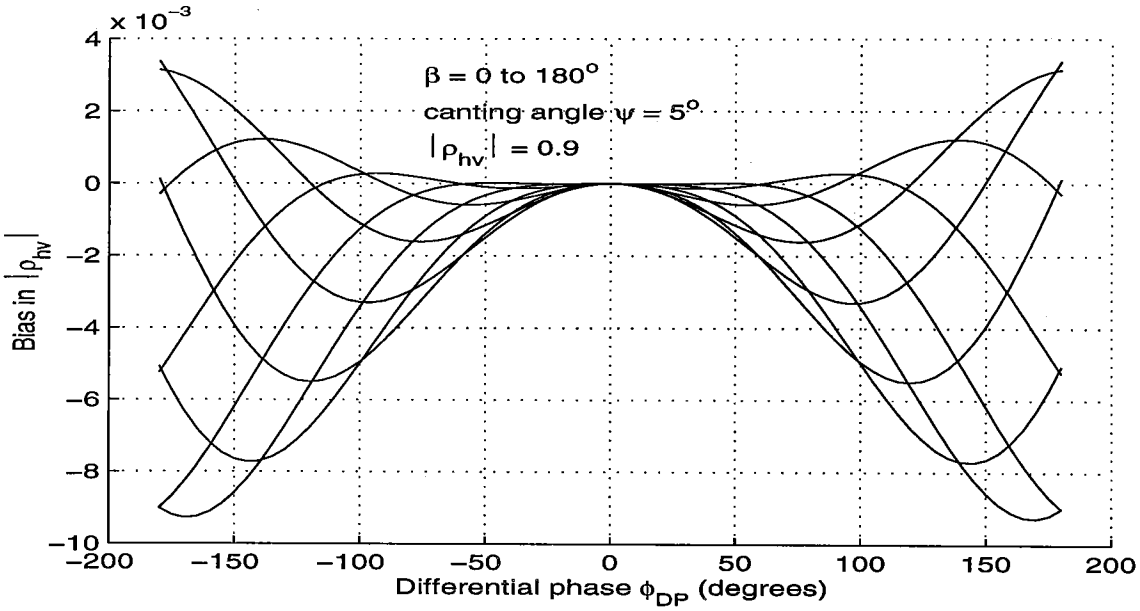

Fig. IV.8 The bias in the measured correlation coefficient $|\rho_{hvm}(0)|$ vs. ϕ_{DP} . β ranges from 0° to 180° in steps of 22.5°, $\alpha = 0^\circ$, and $|\rho_{hv}(0)| = 0.9$.

IV.2.4 Effects of canting dispersion on polarimetric measurements

A random variation of canting angles causes the ensemble of drops to appear less oblate and, thus, will decrease the differential phase due to propagation and indirectly bias the measurements of other intrinsic parameters, even if the mean canting angle is zero. Again referring to Oguchi's (1983) formula for the transmission matrix, it can be shown that the normalized matrix elements are

$$T_{vv} = e^{-j\sigma_\psi^2 \phi_{DP}/2}; \quad T_{hv} = 0; \quad T_{hh} = e^{-j\phi_{DP}/2 + j\sigma_\psi^2 \phi_{DP}/2} \tag{IV.21}$$

under the condition that the mean canting angle is zero, and $\sigma_\psi^2 << 1$. Thus, the dispersion of canting angles decreases the phase shift of the vertically polarized waves, whereas it increases the phase shift of the horizontally polarized wave. The net result is that the propagation differential phase will decrease from the value it would have had if the dispersion were zero.

The decrease of ϕ_{DP} due to canting angle dispersion will cause biases in measurements of Z_{DP} and $|\rho_{hv}|$. Because the bias errors in Z_{DP} and $|\rho_{hv}|$ are functions of ϕ_{DP}, the effect of canting angle dispersion can be determined by moving along any of the curves corresponding to a decrease of ϕ_{DP} by an amount equal to $2\sigma_\psi^2 \phi_{DP}$. It should be pointed out, however, that this reduction in measured differential phase, ϕ_{DPm}, is also present in measurements using alternately transmitted polarizations. Based upon measurements made with alternate transmissions of H, V waves, there is no apparent evidence that canting angle dispersion is a significant contributor to errors in measurement of polarimetric variables.

IV.3. Depolarization upon back scatter

In the next few paragraphs we examine the effects that depolarization upon backscatter has on Z_{dr}, ϕ_{DP}, and ρ_{hv}.

Consider first a single scatterer, illuminated with horizontally and vertically polarized fields and having back scattering matrix coefficients s_{ij}. As before, in order to isolate the effects of depolarization upon backscatter from other effects, we assume no misalignment of the feed (i.e., $\alpha = 0$), canting angles with zero mean (i.e., $\psi = 0$), and equal transmitted magnitudes of vertically and horizontally polarized waves. But there is still a net differential phase between the two polarized components illuminating the scatterer because (1) drops along the propagation path are oblate, and (2) the phase between the two transmitted components is β. Taking these into account and again ignoring radar constants, etc., the corresponding backscatter voltages in the receiver's horizontal and vertical channels are

$$V_h = [s_{hh}e^{-j\Phi_{DP}/2} + s_{hv}e^{j\beta}]\, e^{-j\Phi_{DP}/2 + j\gamma};$$
$$V_v = s_{vv}e^{j\beta} + s_{hv}e^{-j\Phi_{DP}/2}, \tag{IV.22}$$

where ϕ_{DP} is the two-way intrinsic differential phase, and the hydrometeors within the sampled resolution volume are assumed to have a distribution of sizes and differential phases.

IV.3.1 Effects of backscatter depolarization on differential reflectivity measurements

For an ensemble of scatterers, the mean detected power $P_h = \langle V_h V_h^* \rangle$ is

$$P_h = \langle [s_{hh}e^{-j\phi_{DP}/2} + s_{hv}e^{j\beta}][s_{hh}^* e^{j\phi_{DP}/2} + s_{hv}^* e^{-j\beta}] \rangle. \tag{IV.23}$$

An expression similar to (IV.23) can be obtained for the power P_v.

Next we assume that hydrometeors within the resolution volume have a symmetric distribution of canting angles about a zero mean so that (Ryzhkov 1991)

$$\langle s_{hh}s_{hv}^* \rangle = \langle s_{vv}s_{hv}^* \rangle = 0. \tag{IV.24}$$

This is a good assumption for hail, which depolarizes the signal significantly but also causes large cross coupling. Using (IV.24) in (IV.23), the ensemble averages for P_h and P_v reduce to

$$P_h = \langle s_{hh}s_{hh}^* \rangle + \langle s_{hv}s_{hv}^* \rangle;$$
$$P_v = \langle s_{vv}s_{vv}^* \rangle + \langle s_{hv}s_{hv}^* \rangle. \tag{IV.25}$$

Thus, the measured differential reflectivity factor, Z_{drm}, can be expressed as

$$Z_{drm} = Z_{dr}\frac{1 + Ldr}{1 + Z_{dr}Ldr}, \tag{IV.26}$$

where $Ldr \equiv \langle s_{hv}s_{hv}^* \rangle / \langle s_{hh}s_{hh}^* \rangle$.

Ten times the logarithm of the ratio of Z_{drm} / Z_{dr} is plotted in Fig. IV.9 to show the bias in the Z_{DR} measurements as a function of Z_{DR}. In significant hail, Z_{dr} is about, 1 and there is no bias. But in hail mixed with rain, or in the melting layer, there would be significant negative bias. For a case with *Ldr* of 0.01 (i.e., *LDR* = -20 dB) and Z_{dr} of 2 (i.e., Z_{DR} = 3 dB) the bias is less than -0.05 dB but is almost 0.4 dB if *Ldr* increases to the unusually large value of 0.1.

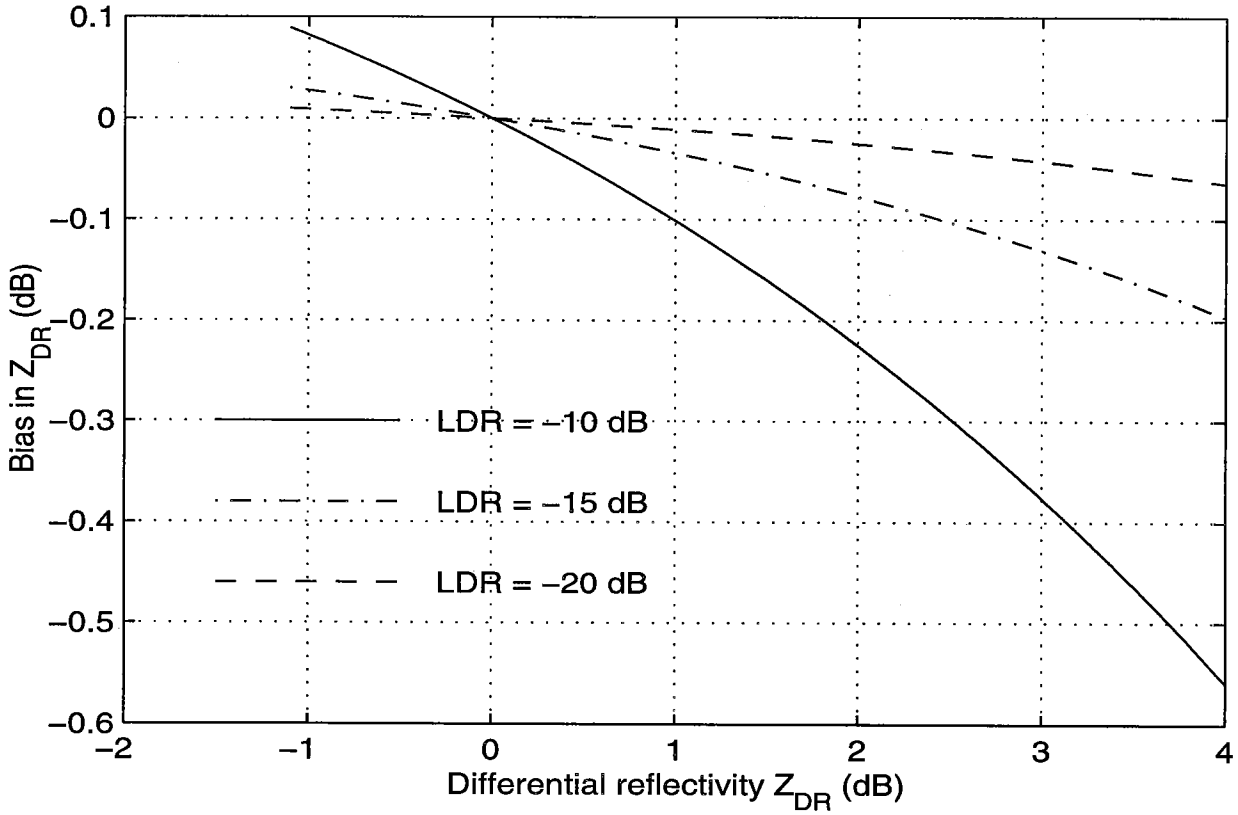

Fig. IV.9 The bias in Z_{DR} measurements, due to depolarization upon backscatter, vs. the intrinsic differential reflectivity for three values of the depolarization ratio, *LDR*. $\beta = 0$, and $\alpha = 0°$.

IV.3.2 Effects of backscatter depolarization on differential phase and correlation magnitude

The correlation coefficient can be obtained from (IV.22) by taking appropriate products and expectations. The result of this computation is

$$\rho_{hvm} = \rho_{hv} \frac{\left[1 + \frac{\langle s_{hv} s_{hv}^* \rangle}{\langle s_{hh} s_{vv}^* \rangle} e^{-j(\phi_{DP}+2\beta)}\right] e^{j(\phi_{DP}+\beta)}}{\left[\left(1 + \frac{\langle s_{hv} s_{hv}^* \rangle}{\langle s_{hh} s_{hh}^* \rangle}\right)^{1/2} \left(1 + \frac{\langle s_{hv} s_{hv}^* \rangle}{\langle s_{vv} s_{vv}^* \rangle}\right)^{1/2}\right]}. \quad \text{(IV.27)}$$

Note that (IV.27) can be written in terms of *Ldr* and Z_{dr}. To get numerical values, we assume that there is no backscatter differential phase δ (i.e., $\delta \equiv \delta_{hh} - \delta_{vv} = 0$), and in the numerator, we express the ratio as

$$\frac{\langle s_{hv} s_{hv}^* \rangle}{\langle s_{hh} s_{vv}^* \rangle} = \frac{Ldr\, Z_{dr}^{1/2}}{\rho_{hv}}. \quad \text{(IV.28)}$$

Because $\delta = 0$, $\langle s_{hh} s_{vv}^* \rangle$ is real, ρ_{hv} is real. With these simplifications, the magnitude of ρ_{hvm} becomes

$$|\rho_{hvm}| = \rho_{hv} \frac{\left[\left|1 + \frac{Ldr\, Z_{dr}^{1/2} e^{-j(\phi_{DP}+2\beta)}}{\rho_{hv}}\right|\right]}{[1 + Ldr]^{1/2}[1 + Ldr\, Z_{dr}]^{1/2}}, \quad \text{(IV.29)}$$

and its phase is

$$\phi_{DPm} - \phi_{DP} = \beta + arg\left[1 + \frac{Ldr\, Z_{dr}^{1/2} e^{-j(2\beta+\phi_{DP})}}{\rho_{hv}}\right]. \quad \text{(IV.30)}$$

Equation (IV.29) indicates that the measured $|\rho_{hvm}|$ is usually biased low compared to the true ρ_{hv}. $|\rho_{hv}(0)|$ bias obtained from (IV.29) is plotted in Fig. IV.10, and the bias in ϕ_{DP} obtained from (IV.30) is plotted in Fig. IV.11 as function of $\phi_{DP} + 2\beta$. The bias in specific differential phase will not be significant, as can be deduced from the following argument. Referring to Fig. IV.11, it is seen that at *LDR* of -15 dB, there is a change of differential phase bias of about 6° per 180° of total differential phase change. Assuming, as in Section IV.1.2, a 1° km^{-1} specific differential phase shift produced by rain, it can be deduced that the added change in the

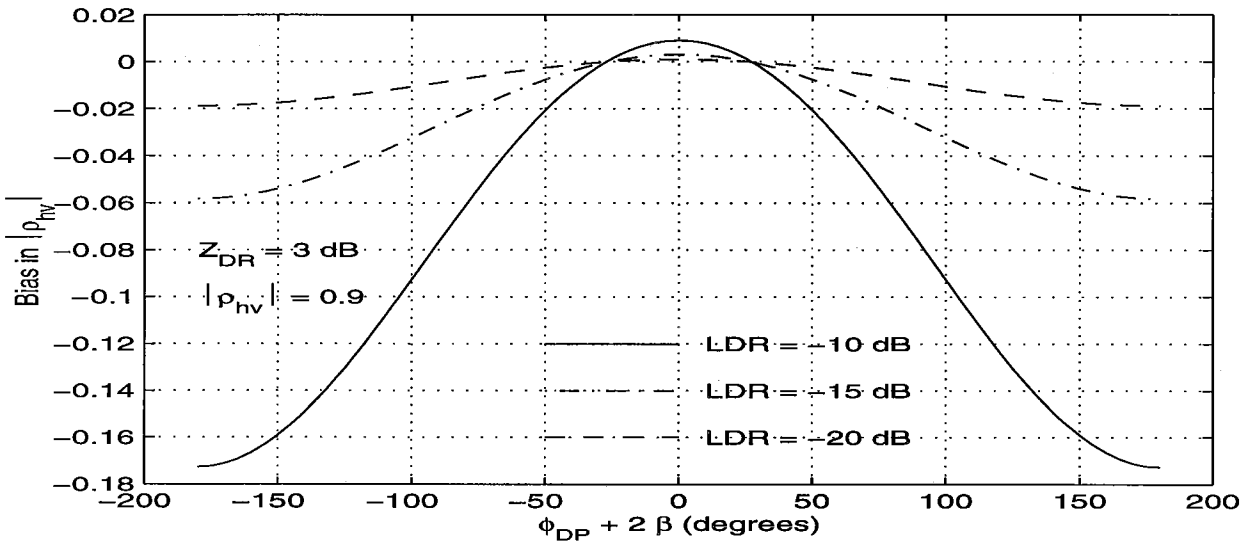

Fig. IV.10 $|\rho_{hv}(0)|$ bias, due to backscatter depolarization, vs. $2\beta + \phi_{DP}$ for three values of the depolarization ratio *LDR*. $\alpha = 0°$, and $\gamma = 0°$.

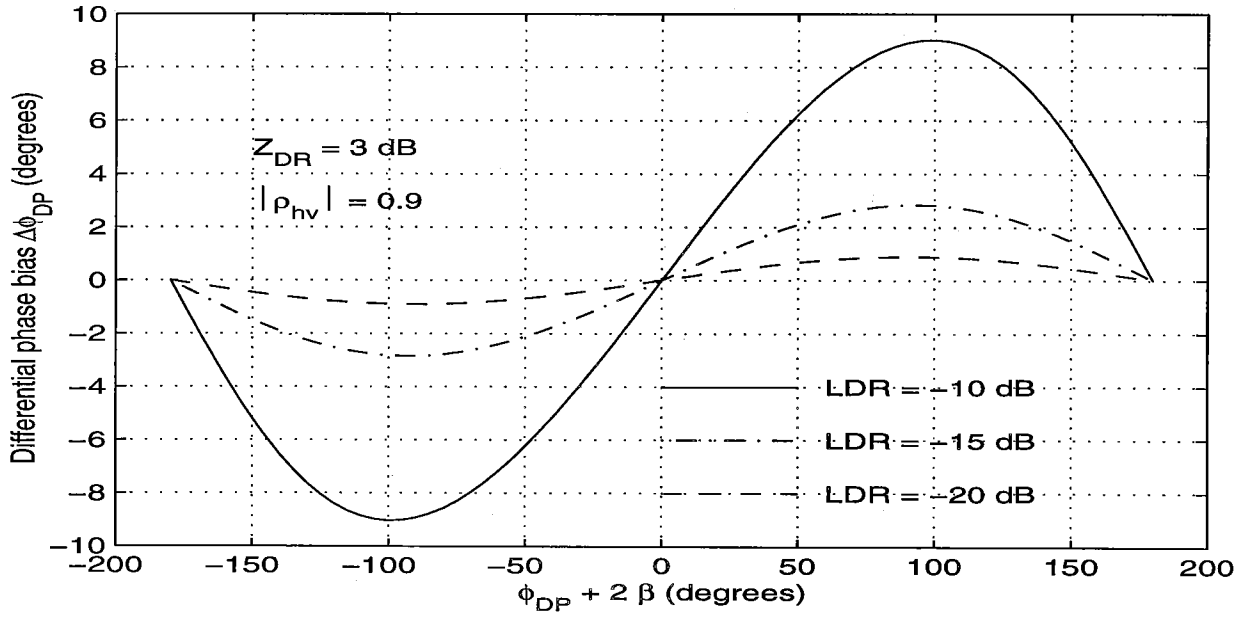

Fig. IV.11 The differential phase bias due to backscatter depolarization vs. the total differential phase $2\beta + \phi_{DP}$, for three values of the depolarization ratio *LDR*. $\alpha = 0°$, and $\gamma = 0°$.

total differential phase shift would be about 0.03° km^{-1}. This corresponds to about a 1 mm h^{-1} change in a rain rate of 37 mm h^{-1}. Similarly, the bias in correlation is not very significant if *LDR* is less than -15 dB. Furthermore, it is mainly negative, and that would accentuate the contrast between hail and rain.

IV.4. Comparison of data obtained with simultaneous and alternate transmissions

There have been no comprehensive comparisons between the proposed mode of simultaneous transmission and reception of H,V signals and the often used alternate H,V transmission and reception mode (i.e., the HV Mode), because hardware modifications to cycle between the two modes are substantial. Also, the initial successes of the alternate scheme negated the need (at least for scientific purposes) to explore less robust but less costly alternatives. Within the last year, scientists at Colorado State University (CSU) have implemented the capability to transmit simultaneous H,V waves and receive these in copolar and cross polar channels through the use of a transfer switch (Fig. III.6); this mode of operation is coined Star (Simultaneous transmission alternate reception). Dr. Bringi and Mr. Brunkow of CSU[10] have provided data that illustrate the potential of the Star mode by comparing nearly simultaneous data collected in each of the two modes. The data were collected in scans separated by one minute; this time separation could account for some of the observed differences seen in the following figures. On the other hand, these data are from a hail storm which presents the most demanding conditions for comparison.

Scattergrams (Fig. IV.12) of the K_{DP} and Z_{DR} for the two modes demonstrate strong correlation between the parameters estimated from data collected with these two modes; the Z_{DR} in the Star mode is higher by about 0.2 dB, but K_{DP} shows no evidence of any bias which is consistent with the theoretical calculations presented in Sections IV.1.2, IV.2.2, and IV.3.2. The cause of the Z_{DR} bias is under investigation. The correlation ρ_{hv} in the Star mode is lower than in the alternate mode; this is consistent with the composite effects of factors discussed in this chapter (i.e., Sections IV.1.3, IV.2.3, and IV.3.2).

In Fig. (IV.13), radial profiles of Z, Z_{DR}, Φ_{DP}, and $|\rho_{hv}(0)|$ are displayed. The correspondence between the reflectivities and differential phases for the two modes is remarkable. As expected (Sections IV.1.3, IV.2.3, and IV.3.2), the correlation in the STAR mode is generally lower.

Overall, these measurements indicate that simultaneous transmission and reception should produce at least as good or better results. This is because reception in HV mode alternates between H and V signals which, due to the Doppler spread, somewhat degrades the estimates.

---

[10] This CSU research is sponsored by the USWRP.

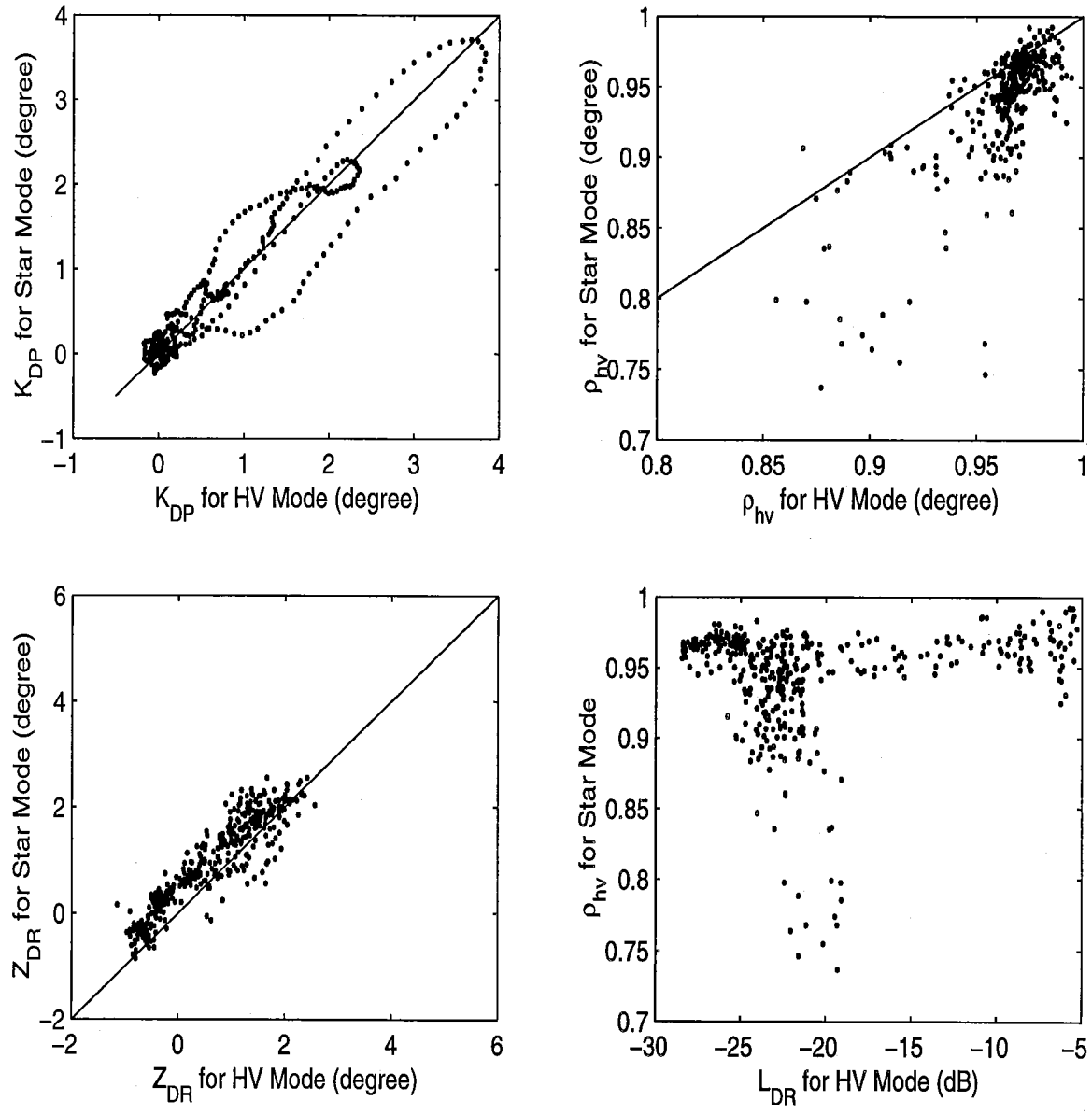

Fig. IV.12 Scattergrams of K_{DP}, ρ_{hv},and Z_{DR} for the H,V and Star modes of polarimetric data collection. Data are from a hailstorm observed with CSU's polarimetric Doppler weather radar.

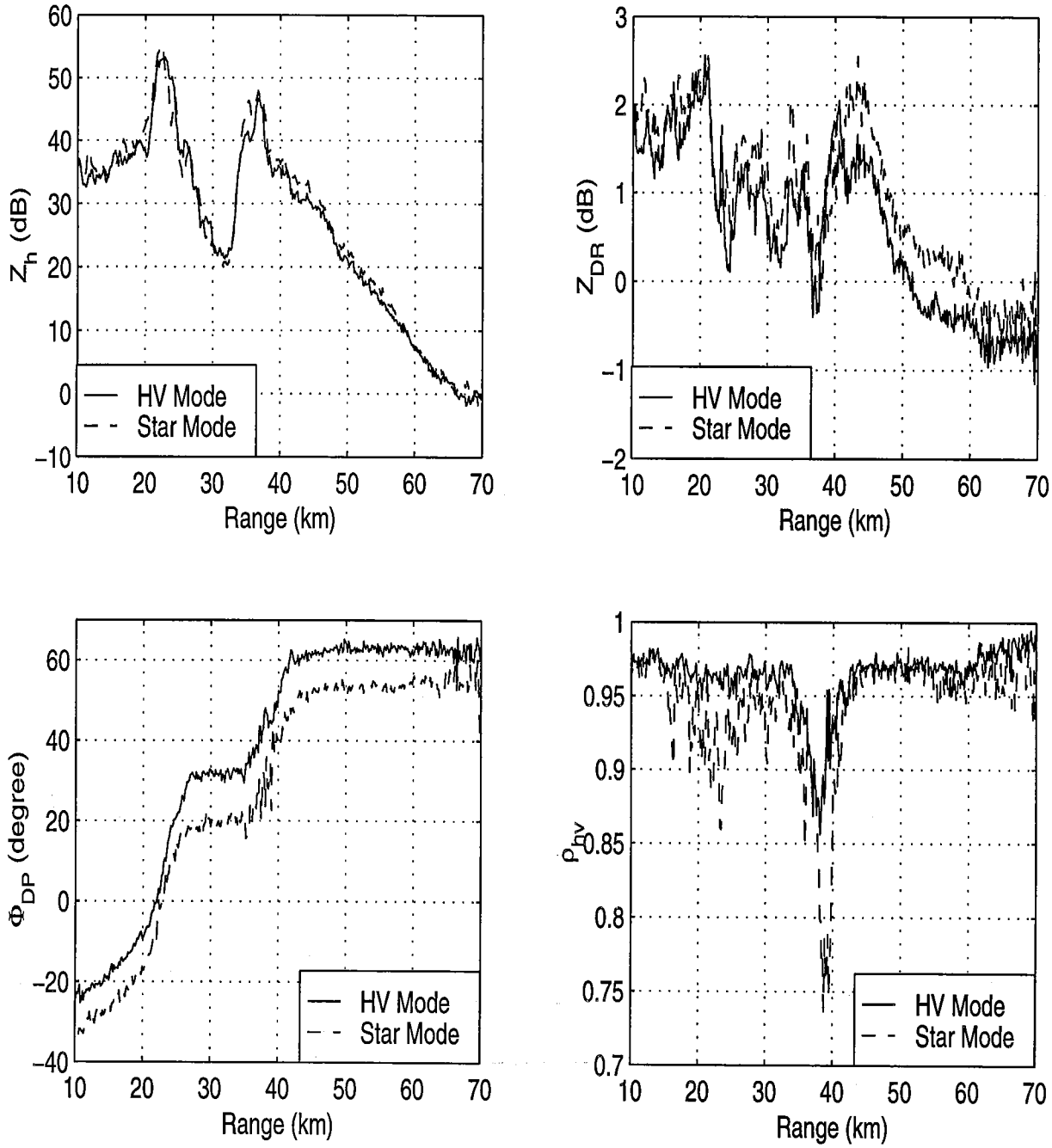

Fig. IV.13 Radial profiles of reflectivity factor at horizontal polarization Z_h, Z_{DR}, Φ_{DP}, and ρ_{hv} for the same data as presented in Fig. IV.12.

IV.5. Summary

Theoretical considerations of feed alignment, canting, and backscatter depolarization suggest that simultaneous transmission of H and V signals would not be detrimental to measurements of specific differential phase K_{DP}, the principal polarimetric parameter which should lead to improved rainfall measurements. Overall, Z_{DR} is much more affected by simultaneous transmission than the other polarimetric parameters. Measurements of the correlation coefficient $\rho_{hv}(0)$ and differential phase ϕ_{DP} can tolerate feed misalignment α of about 1°, whereas Z_{DR} requires α to be less than about 0.1° to 0.2°; this alignment accuracy has been achieved with a dual port feed installed on the research WSR-88D radar (Section II.6.7). Similarily, if differential phase $\phi_{DP} \approx 180°$ (i.e., if propagation is along long paths filled with heavy rain), uniform canting of 1° along the propagation path would significantly bias Z_{dr} (Fig. IV.6) but would not be detrimental to ρ_{hv} (0) and K_{DP}. On the other hand, differential attenaution would be significant at these large values of ϕ_{DP} and is a problem whether H,V waves are transmitted simulataneously or alternately. Differential reflectivity could be affected by depolarization due to backscattering from hail mixed with rain, and the correlation coefficient could also be affected. But backscatter depolarization would accentuate the signatures of low Z_{DR} and low ρ_{hv} in hail regions (i.e., reduce even more the low values of Z_{DR} and ρ_{hv} in these regions; this is observed in Fig. IV.13 for data collected with the CSU polarimetric radar). Thus, the effect might be beneficial.

V. CONCLUSIONS

An engineering evaluation is made in Section II to determine if the existing antenna assembly could be used as is for the dual polarization mode. It was meant to guide us in the selection of hardware for upgrading the WSR-88D (NEXRAD) to polarimetric capability. The current assembly has a feed supported by three struts. This geometry presents a blockage of radiation that differently affects the horizontally and vertically transmitted fields.

Radiation pattern measurements for a number of WSR-88D antennas without a fully assembled radome have been made by Andrew Canada, Inc., manufacturers of the WSR-88D antennas, on their antenna range. Because no pattern measurements were ever made of any WSR-88D antennas on site, it was imperative to make measurements on NOAA/NSSL's research and development WSR-88D (KOUN1) antenna before the feed was changed from one which transmits only horizontally polarized waves to one (a dual port feed) which transmits both horizontally and vertically polarized waves. These pattern measurements are compared to the ones obtained after the dual port feed was installed, and also to those made by Andrew Canada. The patterns, before change of feed, demonstrate that there are no significant changes in the quality of the antenna installed in 1988.

A dual port antenna feed was purchased from Andrew Canada, Inc. and installed on the radar. Pattern measurements were made for the horizontal and vertical polarizations in the horizontal plane and for both polarizations in the lower half of the vertical plane. It is comforting to note that the secondary radiation patterns with the dual port feed are very close to those patterns measured with the single port feed. For polarimetric measurements, it is desirable to have a good match of main lobes at horizontal (H) and vertical (V) polarizations. Both copolar patterns have low sidelobe levels and are well matched in the mainlobe. Beamwidths are 0.93° for the horizontal copolar and 0.90° for the vertical copolar patterns. The match of patterns in the lower half of the vertical plane is excellent, even extending to several of the sidelobes. We have also examined, for points below the boresight, contours of the power ratio (horizontal/vertical in dB) where the antenna gain, relative to the boresight gain, is larger than -20 dB. For the most part, the patterns agree within ±1 dB, and the match is best where the gain is largest (i.e., near the beam axis). For the points far removed from the axis, the difference is larger as expected, but because the antenna gain is much smaller in these regions, the difference is much less significant than for those close to the axis.

Cross polarization patterns were also recorded, and it was observed that the WSR-88D specification of having the cross-polar peak 30 dB below the copolar peak is met. The cross-polar pattern at vertical polarization matches in shape the cross-polar pattern at horizontal polarization, but the amplitudes are about 4 dB higher (still within the measurement uncertainty). Consequently, the addition of the dual port feed, and the retention of the three struts had not degraded the patterns. Therefore, this configuration is recommended for future polarimetric upgrades of the WSR-88D.

Of critical importance to the favorable utility of a polarimetric radar is the selection of an appropriate polarization basis and its practical implementation. Considerations for the choice of polarimetric basis and a few system design options are described in Section III. The circular and linear polarimetric bases are compared. It is demonstrated that the circular basis can, in principle, provide estimates of specific differential phase (K_{DP}) without switching the transmitted polarization. But in weak showers, these estimates are corrupted because the cross-polar signal is almost three orders of magnitude below the copolar signal. But with circular polarization, the cross-polar signal does not depend on the orientation of hydrometeors; furthermore, in combination with the copolar signal, it leads to the measurement of the mean apparent canting angle. Nonetheless, this apparent advantage of the circular polarization basis vanishes in the presence of significant precipitation along the radar beam. A linear polarization basis is well suited for quantitative measurement of rainfall and classification of hydrometeor types without extensive correction of propagation effects. Therefore, our choice rests with the linear H, V basis.

A novel polarimetric scheme employing simultaneous transmission of horizontally and vertically polarized waves is being implemented on the KOUN1 radar. This design includes the installation of two receivers that share several common components, but a single receiver can also measure all the polarimetric variables. With two receivers, the dwell time for computing polarimetric variables is reduced, the ground clutter filter is not affected, and maintenance is simpler. On the down side, the depolarization ratio cannot be measured simultaneously with other polarimetric variables; nonetheless, if desired, it can be measured together with the standard spectral moments in separate volume scans. Having two receivers offers some redundancy that might be advantageous. For comparative testing, NSSL plans to incorporate two receivers in its radar and still retain full WSR-88D compatibility. That is, all current data acquisition modes and scanning strategies can remain as they are, and the impact of polarimetric implementation on the existing algorithms and products should be minimal.

Theoretical evaluation of the effects of feed alignment, canting, and backscatter depolarization on the measurements of polarimetric variables, using simultaneous transmission and reception of the H and V signals, is made in Section IV. The simultaneous transmission and reception mode is not detrimental to measurements of the specific differential phase and coefficient of correlation between H, V weather echoes. The effects of drop canting along propagation paths can be significant on differential reflectivity. However, these effects are detrimental when differential attenuation dominates and is a problem, regardless, if H, V signals are transmitted simultaneously or alternately. Differential reflectivity could be affected by depolarization due to backscattering from hail mixed with rain, and the correlation coefficient could also be affected. But backscatter depolarization would accentuate the signatures of low Z_{DR} and low ρ_{hv} in hail regions (i.e., reduce even more the low values of Z_{DR} and ρ_{hv} in these regions). Thus, the effect might be beneficial.

VI. LIST OF REFERENCES

Balakrishnan, N., and D. S. Zrnic, 1990: Use of polarization to characterize precipitation and discriminate large hail. *J. Atmos. Sci.,* **47,** 1525-1540.

Barge, B. L., 1970: Polarization observations in Alberta. *Preprints, 14th Radar Meteorology Conference,* Tuscon, AZ, AMS, Boston, MA, 221-224.

Barge, B. L., 1974: Polarization measurements of precipitation back scatter in Alberta. *J. Res. Atms.,* **8**, 163-173.

Battan, L. J., 1973: *Radar Observations of the Atmosphere*, Uni. Chicago Press, 323 pp.

Beard, K. V., and A. R. Jameson, 1983: Raindrop canting. *J. Atmos. Sci.,* **40**, 448-454.

Beard, K. V., H. T. Ochs, and R. J. Kubesh, 1989: Natural oscillations of small raindrops. *Nature,* **342**, 408-410.

Beckmann, P. and A. Spizzichino, 1963: *The scattering of Electromagnetic Waves from Rough Surfaces*. Macmillan Co., 503 pp.

Bebbington, D. H. O., R. McGuinness, and A. R. Holt, 1987: Correction of propagation effects in S-band circular polarization-diversity radars. *IEE Proc.,* **134**, 431-437.

Bringi, V. N., V. Chandrasekar, N. Balakrishnan, and D. S. Zrnić, 1990: An examination of radar propagation effects in rainfall at microwave frequencies. *J. Atmos. Oceanic Tech.,* **7,** 829-840.

Brussard G., 1978: A meteorological model for rain-induced cross polarization, *IEEE Tr. on Antennas and Propagation,* **AP-24,** 5-11.

Chandrasekar, V., and R. J. Keeler, 1993: Antenna pattern analysis and measurements for Multiparameter Radars. *J. Atmos. Oceanic Tech.*, **10**, 674-683.

Doviak, R. J., and D. S. Zrnic, 1993: *Doppler Radar and Weather Observations*. Academic Press, 562 pp.

English, M., B. Kochtubajda, F. D. Barlow, A. R. Holt, and R. McGuinness, 1991: Radar measurement of rainfall by differential propagation phase: A pilot experiment. *Atmos.-Ocean,* **29**, 357-380.

Fradin, A. Z., 1961: *Microwave Antennas*. Pergamon Press, 668 pp.

Haddad, Z. S., and D. Rosenfeld, 1997: Optimality of empirical Z-R relations. *Quar. J. Roy. Meteoro. Soc.*, **123**, 1283-1293.

Herzegh, P. H., and R. E. Carbone, 1984: The Influence of Antenna Illumination Function Characteristics on Differential Reflectivity Measurements. *22nd Conference Radar Meteorology*, Amer. Meteor. Soc., Boston, MA., 281-286.

Holt, A. R., 1988: Extraction of differential propagation phase from data from S-band circularly polarized radars. *Elect. Letts.*, **24**, 1241-1242.

Jameson, A. R., 1983: Microphysical interpretation of mult-parameter radar measurements in rain. Part I: Interpretation o fpolarization measurements and estimation of raindrop shapes. *J. Atmos. Sci.*, **40**, 1792-1802.

Long, M. W., 1975: *Radar Reflectivity of Land and Sea.* Lexington Books, 366 pp.

McCormick, G. C., and A. Hendry, 1975: Principles for the radar determination of the polarization properties of precipitation. *Radio Sci.*, **10**, 421-434.

McGuinness, R., D. H. O. Bebbington, and A. R. Holt, 1987: Modeling propagation effects in the use of S-band polarization-diversity radars. *IEE Proc.*, **134**, 423-430.

Oguchi, T., 1983: Electromagnetic wave propagation and scattering in rain and other hydrometeors. *Proc. IEEE,* **71,** 1029-1078.

Paramax Systems Corp., 1992: Test report CDRL 246; Antenna pedestal, Part 1 of 4, Document #TR1218305, 1 July. Prepared by Paramax Systems Corp. for the U. S. Depart. of Comm., Office of Procurement, Washington, D. C. 20230.

Pointin, Y., D. Ramond, and J. Fournet-Fayard, 1988: Radar Differential Reflectivity Z_{DR}: A Real-Case Evaluation of Errors Induced by Antenna Characteristics. *J. Atmos.Oceanic Tech.*, **5**, 416-423.

Radiation Systems, 1993: Electrical Acceptance Test Procedure, CHILL Antenna. Report dated Nov. 12, 1993, prepared by Radiation Systems Inc., Technical Products Division, Sterling, Va., 67 pp.

Ryzhkov, A. V., 1991: Polarimetric information measurements in radar meteorology; theoretical model. *Radio electronics and communication* (In Russian), **2**, 17-23.

Ryzhkov, A. V., 1993: Polarization methods in radar meteorology (in Russian). *Foreign Radio Electronics*, **4,** 18-28.

Ryzhkov, A. V., and D. S. Zrnic, 1995: Precipitation and attenuation measurements at a 10-cm wavelength. *J. Appl. Meteor.*, **34,** 2121-2123.

Ryzhkov, A. V., and D. S. Zrnic, 1996: Assessment of rainfall measurement that uses specific differential phase. *J. Appl. Meteor.*, **35**, 2080-2090.

Ryzhkov, A. V., and D. S. Zrnic, 1998: Polarimetric rainfall estimation in the presence of anomalous propagation. Accepted for publication in *J. Atmos. Oceanic Tech.*

Sachidananda, M., and D. S. Zrnić, 1985: Z_{DR} measurement considerations for a fast scan capability radar. *Radio Sci.*, **20,** 907-922.

Sachidananda, M., and D. S. Zrnic, 1986: Differential propagation phase shift and rainfall rate estimation. *Radio Sc.*, **21,** 235-247.

Sachidananda, M., and D. S. Zrnic, 1989: Efficient processing of alternately polarized radar signals. *J. Atmos. Oceanic Tech.*, **6,** 173-181.

Saffle, R. E., L. D. Johnson, 1997: NEXRAD Product Improvement Overview. *Preprints 13th IIPS*, Longbeach, CA., Amer. Meteor. Soc., 223-227.

Seliga, T., and V. N. Bringi, 1976: Potential use of radar differential reflectivity measurements at orthogonal polarizations for measuring precipitation. *J. Appl. Meteor.*, **15**, 69-76.

Seliga, T., and V. N. Bringi, 1978: Differential reflectivity and differential phase shift: Application in radar meteorology. *Radio Science.*, **13**, 271-275.

Sengupta, D. L., and R. E. Hiatt, 1970: Reflectors and Lenses, Chapter 10 in *Radar Handbook*, M. I. Skolnik, Ed., McGraw Hill.

Sherman, J. W., 1970: Aperture-antenna analysis, Chapter 9 in *Radar Handbook*, M. I. Skolnik, Ed., McGraw Hill.

Spilhaus, A. F., 1948: Raindrop size, shape, and falling speed. *J. Meteorol.*, **5**, 108-110.

Torlaschi, E., and B. Pettigrew, 1990: Propagation effects on reflectivity for circularly polarized S-band radars. *J. Atmos. Oceanic Tech.*, **7**, 114-117.

Torlaschi, E., and A. R. Holt, 1993: Separation of propagation and backscattering effects in rain for circular polarization diversity S-Band radars. *J. Atmos. Oceanic Tech.*, **10**, 465-477.

Zahrai, A., and D. S. Zrnic, 1993: The 10-cm Wavelength Polarimetric Weather Radar at NOAA's National Severe Storms Laboratory. *J. Atmos. Oceanic Tech.*, **10**, 649-662.

Zahrai, A., and D. S. Zrnic, 1997: Implementation of polarimetric capability for the WSR-88D (NEXRAD) radar. *Preprints 13th IIPS*, Longbeach, CA., Amer. Meteor. Soc., 284-287.

Zawadski, I., 1984: Factors affecting the precision of radar measurements of rain. *Preprints: 22nd Conf. Radar Meteor.*, Amer. Meteor. Soc., Boston, MA, 251-256.

Zrnic, D. S., 1996: Simultaneous Differential Polarimetric Measurements and Co-polar Correlation Coefficient Measurements. *U.S. Patent Number 5500646*, March 19, 1996.

Zrnic, D. S., 1996: Weather Radar Polarimetry-Trends Toward Operational Applications. *Bull. Amer. Meteor. Soc.*, **77**, 1529-1534.

Zrnic, D. S., N. Balakrishnan, A. V. Ryzhkov, and S. L. Durden, 1994: Use of correlation coefficient for probing precipitation at nearly vertical incidence. *IEEE Trans. Geosci. Remote Sens.*, **32,** 740-748.

Zrnic, D. S., and A. V. Ryzhkov, 1996: Advantages of rain measurements using specific differential phase. *J. Atmos.Oceanic Tech.*, **13**, 454-464.

VII. LIST OF NSSL REPORTS FOCUSSED ON POSSIBLE UPGRADES TO THE WSR-88D RADARS

Sachidananda, M., 1997: Signal Design and Processing Techniques for WSR-88D Ambiguity Resolution, Part 1, 100 pp.

Sirmans, D., D. S. Zrnic, and M. Sachidananda, 1986: Doppler radar dual polarization considerations for NEXRAD, Part I. 109 pp.

Sirmans, D., D. S. Zrnic, and N. Balakrishnan, 1986: Doppler radar dual polarization considerations for NEXRAD, Part II. 70 pp.